2015

# BIOLOGICAL MATERIALS: PART A. TEMPERATURE-RESPONSIVE POLYMERS AND DRUG DELIVERY AND PART B. POLYMER MODIFICATION OF FISH SCALE AND THEIR NANO-MECHANICAL PROPERTIES

Xu Xiang
*Michigan Technological University*

# BIOLOGICAL MATERIALS: PART A. TEMPERATURE-RESPONSIVE POLYMERS AND DRUG DELIVERY AND PART B. POLYMER MODIFICATION OF FISH SCALE AND THEIR NANO-MECHANICAL PROPERTIES

By

Xu Xiang

A DISSERTATION

Submitted in partial fulfillment of the requirements for the degree of

DOCTOR OF PHILOSOPHY

In CHEMISTRY

MICHIGAN TECHNOLOGICAL UNIVERSITY

2015

This dissertation has been approved in partial fulfillment of the requirements for the Degree of DOCTOR OF PHILOSOPHY in CHEMISTRY.

Department of Chemistry

Dissertation Advisor: *Dr. Patricia A. Heiden*

Committee Member: *Dr. Tarun K. Dam*

Committee Member: *Dr. Loredana Valenzano*

Committee Member: *Dr. Bruce P. Lee*

Department Chair: *Dr. Cary F. Chabalowski*

# Table of Contents

List of Figures ..... ix

List of Tables ..... xv

List of Schemes ..... xvi

Preface ..... xvii

Acknowledgements ..... xix

List of Abbreviations ..... xx

Abstract ..... xxiv

Chapter 1 Introduction ..... 1

Chapter 2 Introduction of RAFT Polymerization ..... 5

2.1 Introduction ..... 5

2.1.1 Controlled radical polymerization and RAFT polymerization ..... 5

2.1.2 Mechanism of RAFT Polymerization and Formation of End groups ..... 6

2.2 CTA Synthesis ..... 9

2.2.1 Single functional CTAs of the $ZCS_2R$ type ..... 9

2.2.1.1 Dithioester CTAs: ..... 10

2.2.1.1.1 Grignard route: ..... 10

2.2.1.1.2 Synthesis of CTAs from benzoic acid and $P_4S_{10}$ or Davy-R reagents: ..... 11

2.2.1.1.3 Other methods ..... 12

2.2.1.2 Trithiocarbonate CTAs: ..... 13

2.2.2 Multi-functional CTAs ..... 15

2.2.2.1 CTAs for Star Polymers: $R(CS_2R')_n$ ..... 15

2.2.2.2 Linear Multifunctional CTAs: $R_1CS_2R_2CS_2R_3$ ..... 16

2.2.3 Macro-CTAs ..... 19

2.3. Polymer end-group removal and modification ..... 20

Chapter 3 End Group Polarity and Block Symmetry Effects on Cloud Point and Hydrodynamic Diameter of Thermoresponsive Block Copolymers ..... 24

3.1 Introduction ..... 24

3.2 Experimental ..... 29

3.2.1 Materials ..... 29

3.2.2 CTA synthesis ..... 29

3.2.3 Synthesis of statistical P(DEGMA-co-OEGA) ($D_xO_y$) copolymer ..... 31

3.2.4 Synthesis of diblock P(DEGMA-*b*-OEGA) copolymers (S-$D_xO_y$-C(1-6) and S-$O_yD_x$-C(1-6)) by two step RAFT polymerization ..... 32

3.3 Characterization ..... 33

3.4 Results and Discussion ..... 35

3.4.1 Measured copolymer composition ..... 37

3.4.2 CP of Statistical copolymers ..... 38

3.4.3 Effect of end group on diblock copolymer properties ..... 39

3.5 Conclusions ..... 49

Chapter 4 GNP-polymer drug delivery system ..... 52

4.1 Introduction ..... 52

4.2 Experimental ..... 57

4.2.1 Materials ..... 57

4.2.2 Syntheses: S-$D_{50}O_{50}$-C and S-$D_{40}O_{60}$-C ..... 57

4.2.3 Reduction of the Dithioester group to a Thiol group ..... 58

4.2.4 Synthesis of GNPs (20 nm) ..... 58

4.2.5 Assembly of GNP-polymer hybrid nanoparticles ..... 59

4.2.6 Characterization of diblock copolymers and their GNP-polymer hybrid nanoparticles ..... 59

4.2.7 Loading and controlled release of ibuprofen of GNP-diblock copolymer hybrids ..... 60

4.3 Results and discussion ..... 62

4.3.1 Characterization of the Diblock Copolymers ..... 63

4.3.1.1 Composition ..... 63

4.3.1.2 Characterization of T-$D_{50}O_{50}$-C and T-$D_{40}O_{60}$-C ..... 66

4.3.2 GNP-polymer nanoparticles ..... 68

4.3.2.1 Characterization of GNP-polymer nanoparticles ..... 68

4.3.2.2 DLS analysis of GNP-polymer hybrids ..... 68

4.3.3 Nanoparticle drug loading and controlled release from the nanoparticles ..... 73

4.4 Conclusions ..... 79

Chapter 5 Peptide-Directed Self-Assembly of Functionalized Polymeric Nanoparticles: Multiple Drug Loading Ability ..... 81

5.1 Introduction ..... 81

5.2 Experimental ..... 85

5.2.1 Materials ..... 85

5.2.2 Synthesis of Amphiphilic Triblock Copolymers ..... 86

5.2.3 Coupling Reaction of Copolymer with Peptide (P1 and P2) ..... 87

5.2.4 Self-Assembly Study of Peptide-Copolymer Conjugates in Aqueous Solution ..... 88

5.2.5 Controlled Release Testing ..... 89

5.3 Results and Discussions ..... 91

5.3.1 Proof of self-assembling by DLS ..... 91

5.3.2 Drug delivery calculation ..... 94

5.3.3 Release data discussions ..... 97

5.4 Conclusion ..... 104

Chapter 6 Polymer Modification of Fish Scale and their Nano-mechanical Properties . 106

6.1 Introduction ..... 106

6.2 Experimental ..... 110

6.2.1 Materials ..... 110

6.2.2 Fish scale modifications ..... 111

6.2.2.1 Cleaning fish scale surfaces (FS and FS-W) ..... 111

6.2.2.2 Fish scales treated by acid or base (FS-H and FS-OH) ..... 111

6.2.2.3 Fish scales treated by Clorox® (FS-C) ..... 111

6.2.2.4 Fish scales modified with $SiO_2$ (FS- $SiO_2$ and FS- $SiO_2$-C) ..... 111

6.2.2.5 Polymer-modified fish scales (FS-PMMA, FS-POEGA, FS-PMA) ..... 112

6.2.3 Preparation of Scale Cross Sections ..... 113

6.2.4 Modulus Using AFM ..... 113

6.3 Results and Discussion ..... 114

6.3.1 Visualization and Analysis of Unmodified Scales: FS and FS-W ..... 114

6.3.2 Selectively degraded scales: FS-H, FS-OH and FS-C ..... 116

5.3.2.1 Changes in composition and structure by FTIR ..... 116

6.3.2.2 Changes in Equilibrium Moisture Content (EMC) ..... 120

6.3.3 Polymer-modified scales ..... 122

6.3.3.1 Changes in composition by FTIR ..... 122

6.3.3.2 Changes in Equilibrium Moisture Content (EMC) of polymer-modified fish scale ..... 124

6.3.4 Nanomechanical properties ..... 125

6.3.4.1 Biomineral surfaces ..... 125

6.3.4.2 Cross section of the samples ..... 129

6.4 Conclusions ..... 131

References ..... 134

Chapter 2 references ..... 134

Chapter 3 references ..... 139

Chapter 4 references ..... 143

Chapter 5 references ..... 148

Chapter 6 references ..... 152

Appendix A: Supporting information for Chapter 3 ..... 157

Appendix B: Derjaguin-Muller-Toropov (DMT) modulus background (Chapter 6) . 162

Appendix C: Permission License Number for Chapter 5 ..... 167

Appendix D: Permission License Number for Figures in Chapter 2 ..... 168

Permission License Number for Figure 2.8 ..... 168

Permission License Number for Figure 2.21 ..... 169

Permission License Number for Figure 2.23 ..... 170

Permission License Number for Figure 2.24 and Figure 2.26 ..... 171

Permission License Number for Figure 2.27 ..... 172

# List of Figures

Figure 2.1 Generic structures for a Dithioester and a Trithiocarbonate RAFT CTA. ..... 5

Figure 2.2: Generic families of monomers suitable for RAFT polymerization..... 6

Figure 2.3: Schematic of RAFT polymerizations ..... 8

Figure 2.4: End groups of RAFT polymerizations ..... 8

Figure 2.5: Canonical forms of xanthates and dithiocarbamates ..... 9

Figure 2.6: General procedure to dithioester CTAs by Grignard route ..... 10

Figure 2.7: CTAs synthesized by a Grignard route ..... 11

Figure 2.8: Synthesis of CTAs from $P_4S_{10}$ (Adapted from Angew. Chem. Int. Ed. 2003, 42, 2869-2872) ..... 12

Figure 2.9: Synthesis of CTAs using a Davy-R reagent. ..... 12

Figure 2.10: Radical exchange process ..... 13

Figure 2.11: Examples of radical exchange ..... 13

Figure 2.12: Procedure to synthesize trithiocarbonate CTAs ..... 13

Figure 2.13: Xanthates and dithiocarbamates ..... 14

Figure 2.14: Trithiocarbonate CTAs ..... 14

Figure 2.15: Synthesize the symmetry CTA with two acid group as ends ..... 15

Figure 2.16: Trifunctional star CTAs..... 16

Figure 2.17: Linear multi-functional CTA synthesis ..... 16

Figure 2.18: Illustration of the potentially active sites and the preferred reactive site. .... 17

Figure 2.19: Linear multi-functional CTAs ..... 18

Figure 2.20: Illustration of the side reactions of CTA 21 and CTA 23 that lead to different polymer products from multi-functional CTAs ..... 18

Figure 2.21: Use of a macro-CTA (Copied from ACS Appl. Mater. Interfaces, 2011, 3(3), 898-909. See Appendix D for a copy of the copyright transfer agreement.) ..... 19
Figure 2.22: A "grafting-from" approach ..... 20
Figure 2.23: End group modifications (Adapted from Polym. Chem., 2010, 1, 149-157) 20
Figure 2.24: Thermolysis of RAFT-synthesized polymersm (Copied from Polym. Chem., 2010, 1, 149-157. See Appendix D for a copy of the copyright transfer agreement.) ..... 21
Figure 2.25: Mechanism of radical induced end group removal ..... 22
Figure 2.26: Metal nanoparticles attached to RAFT-synthesized polymer via thiol groups (Adapted from Polym. Chem., 2010, 1, 149-157) ..... 22
Figure 2.27: Three main approaches for polymer/gold nanocomposites (Copied from Advances in Colloid and Interface Science, 2009, 149, 28-38. See Appendix D for a copy of the copyright transfer agreement.) ..... 23
Figure 3.1: CTAs to be studied ..... 28
Figure 3.2. This graphical illustration (blue hexagons represent the "C" end) is used to give a simplified image of polymer structure, and show their abbreviated designations. "S" as a chain end refers to a dithioester or trithiocarbonate group from the CTA, while "C" refers to the other chain end resulting from an asymmetric CTA. ..... 28
Figure 3.3 The label for each hydrogen on NMR spectra ..... 34
Figure 3.4: CP curves of diblock copolymers from DT1-3. A: S-DxOy-C(1-3) B: S-OyDx-C(1-3) ..... 40
Figure 3.5 (a) bar chart comparing CPs based on end group and block sequence, (b) $D_h$ and CP, and (c) $D_h$ and $\Delta T$ ..... 41

Figure 3.6 Affect of temperature on conformations of (a) S-DxOy-C, where chain end and block polarity are matched; (b) possible interactions between dithioester chain ends in the micellar core; and (c) S-OyDx-C, where chain end and block polarity are mismatched. ..... 42

Figure 3.7. Graphs of transmittance v. temperature for symmetrical triblock copolymers that have both (a) hydrophilic and (b) hydrophobic, symmetric chain ends. ..... 45

Figure 3.8: Proposed structures for symmetrical triblock copolymers from TC1 and TC2 in aqueous solution. ..... 46

Figure 3.9: CP for Star copolymer ..... 48

Figure 3.10: Star polymer structure in aqueous solution ..... 48

Figure 4.1: GNP-polymer synthesis and drug delivery property test ..... 56

Figure 4.2: Diblock copolymer synthesis procedure ..... 58

Figure 4.3 Standard curve of ibuprofen in PBS buffer. ..... 62

Figure 4.4 The $^{1}H$ NMR spectrum of S-$D_{50}O_{50}$-C. ..... 63

Figure 4.5a Photos showing the change in color after a solution of S-$D_{50}O_{50}$-C (dithioester end group) dissolved in $CH_2Cl_2$ (left) is subjected to aminolysis to give a thiol-terminated copolymer T- $D_{50}O_{50}$-C in $CH_2Cl_2$ (right, after the product is isolated and re-dissolved in $CH_2Cl_2$). ..... 64

Figure 4.5b FTIR of S-$D_{50}O_{50}$-C and T-$D_{50}O_{50}$-C ..... 65

Figure 4.6 $^{1}H$ NMR of S-$D_{50}O_{50}$-C (left) and T-$D_{50}O_{50}$-C (right). ..... 65

Figure 4.7 CP curves of a) S-$D_{50}O_{50}$-C and T-$D_{50}O_{50}$-C; and ..... 67

b) S-$D_{40}O_{60}$-C and T-$D_{40}O_{60}$-C ..... 67

Figure 4.8 Color of GNPs (left) and GNP-polymer nanoparticles (right). ..... 68

Figure 4.9 The mechanism of aminolysis. ..... 69

Figure 4.10a Temperature dependent spectra of GNP-$D_{50}O_{50}$-C ..... 70

Figure 4.10b Proposed structure differences of S-$D_{50}O_{50}$-C and GNP-$D_{50}O_{50}$-C in aqueous solution..... 70

Figure 4.11 Temperature-dependent $D_h$ of S-$D_{50}O_{50}$–C and its GNP-hybrid nanoparticle ..... 71

Figure 4.12 The Temperature-dependent $D_h$ of the GNP-hybrid nanoparticles ..... 72

Figure 4.13 Uv-*vis* spectrum of ibuprofen..... 74

Figure 4.14a: The release curve mass vs time: a) GNP-$D_{50}O_{50}$-C b) GNP-$D_{40}O_{60}$-C..... 75

Figure 4.14b: The percent release (%) curve from drug loaded vs time:a) GNP-$D_{50}O_{50}$-C b) GNP-$D_{40}O_{60}$-C..... 75

Figure 4.15 Ibuprofen release shown as release mass vs. time^1/2..... 78

Figure 5.1 Illustration of the assembly of a 3-nanoparticle system ..... 85

Figure 5.2 DLS test showing the hydrodynamic diameter resulting from different stages of self-assembly. (a) and (b) Hydrodynamic diameter of the individual nanoparticles P1-NP-P1 and P2-NP-P2; (c) Hydrodynamic diameter of an assembled nanoparticle trimer form by mixing P1-NP-P1 with P2-NP-P2 at 2:1 ratio after 20 h of assembly time; (d) Hydrodynamic diameter of an assembled nanoparticle fiber by mixing P1-NP-P1 with P2-NP-P2 at 1:1 ratio after 20 h of assembly time. ..... 92

Figure 5.3 Chemical structure of the model drugs. (a) Nitrofurazone (NF), (b) 4′,5′-Dibromofluorescein (DBF) and (c) Fluorescein (FL)..... 94

Figure 5.4 Standard curves of NF, DBF and FL used for the quantitative determination of the multiple released drugs (Test done in PBS)..... 95

Figure 5.5 Cumulative release of model drugs from multiple drug-loaded self-assembled nanoparticle scaffolds over 24 h. (a) NF and DBF release from a two drug-loaded scaffold, mg per 100 mL PBS buffer; (b) wt.% cumulative release from two drug-loaded scaffold. (c) NF, DBF and FL release from a triple drug-loaded scaffold, mg per 100 mL PBS buffer; (d) wt.% cumulative release from triple drug-loaded scaffold. ..... 100

Figure 6.1 The diagram illustrates the different scale structures and modified scales. From left: an assembly of scales showing their overlap (top left); a representation of an individual scale before and after washing, and the alternating collagen layers. The second row represents the expected changes in structure resulting from chemical modifications. ..... 113

Figure 6.2 Surface of FS control scales imaged by optical microscope and AFM. The probe tip in the optical images has a 40 μm diameter. AFM images show a 6μmx6μm area. At bottom a topographical AFM image maps the roughness of the biomineral layer. ..... 114

Figure 6.3 Cross-section of FS-W showing the different layers of collagen ..... 116

Figure 6.4 FTIR of FS (a) and FS-W (b) ..... 117

Figure 6.5 IR for soaked samples: FS-H (a), FS-OH (b) and FS-C (c) ..... 118

Figure 6.6 EMC of modified fish scale (Soaked with different solution) ..... 121

Figure 6.7 IR for polymer-modified fish scale: FS-$SiO_2$ (a) and FS-POEGA (b) ..... 122

Figure 6.8 EMC of Polymer-modified fish scales ..... 124

Figure 6.9 Optical and AFM images showing changes in surface features of (a) FS, (b) FS-$SIO_2$-C and (c) FS-$SiO_2$. ..... 128

Figure 6.10 Cross section AFM test (6μm X 6μm) ..... 129

Figure A1 TC1 (a) $^{1}H$ NMR spectrum and (b) $^{13}C$ NMR spectrum ..... 158

Figure A2 TC2 $^{1}H$ NMR spectrum ..... 158

Figure A3 TDT $^{1}H$ NMR spectrum ..... 159

Figure A4 GPC spectra of PEG standard polymers. (RI Intensity vs PEG Retention Time (min)..... 160

Figure A5 GPC of Specimen TC1/C-$D_{25}O_{50}D_{25}$-C ..... 161

Figure B1 The basic DMT model ..... 163

Figure B2 DMT modulus of fish scale tested by AFM (Adapted from *Beilstein J. Nanotechnol.* 2013, 4, 611–624.)..... 164

# List of Tables

Table 3.1 Copolymer composition, $D_h$, CP and $\Delta T$ ..... 37

Table 3.2 Effect of end groups on thermoresponse of symmetrical triblock copolymers 45

Table 4.1 Characteristics of the Diblock Copolymers ..... 66

Table 4.2 $D_h$ of GNP-hybrid polymers and block copolymer ..... 71

Table 4.3 Loading efficiency and release data..... 76

Table 5.1 Reactant ratios and theoretical data of triblock copolymer ..... 87

Table 5.2 Hydrodynamic diameter of a scaffold "Trimer" and the full scaffold after restoration of peptide-functionalized nanoparticle stoichiometry. ..... 94

Table 5.3 Released quantity of model drugs from the two-drug scaffold (in 100ml PBS buffer). ..... 97

Table 5.4 Quantity of each model drug released from the three-drug scaffold (in 100 mL PBS buffer). ..... 98

Table 5.5 Loading efficiency of model drugs in two-drug and three-drug nanoparticle scaffolds. ..... 99

Table 6.1 Summary of designations..... 112

Table 6.2 EMC of modified samples at 48 hours (80% relative humidity)..... 121

Table 6.3 EMC of polymer-modified samples at 48 hours (80% relative humidity) ..... 124

Table 6.4 Modulus (GPa) of the biomineral surface of fish scales..... 127

Table 6.5 Modulus of cross-sectional layers of scales (GPa) ..... 130

Table A1 Molecular weights and PDI of PEG standard polymers. ..... 159

Table A2 Molecular weight and Polydispersity by GPC..... 160

# List of Schemes

Scheme 3.1: TC1 synthesis ..... 30

Scheme 3.2: TC2 synthesis ..... 30

Scheme 3.3: TDT synthesis ..... 31

Scheme 3.4: Statistical copolymer synthesis ..... 32

Scheme 3.5: Diblock copolymer synthesis ..... 33

# Preface

The initial ideas for the projects described in this dissertation were by Professor P. A. Heiden, but all the decisions regarding synthetic methods and the approaches to achieve the objectives were made by the author. Furthermore, all the research contained within this dissertation was performed by the author with the exceptions as noted below.

Chapter 3 contains a manuscript accepted for publication "End Group Polarity and Block Symmetry Effects on Cloud Point and Hydrodynamic Diameter of Thermoresponsive Block Copolymers" in *Journal of Polymer Science Part A: Polymer Chemistry*. The authors are: Xu Xiang[1,*], Xiaochu Ding[1, 2], Ning Chen[1], Beilu Zhang[1], and Patricia A. Heiden[1,*]. I certify that I performed all the research in this manuscript except the following: Dr. Xiaochu Ding (Department of Bioengineering, University of Pittsburgh) ran the Gel Permeation Chromatography (GPC) results given in the manuscript; Dr. Ning Chen (National Institute of Standards and Technology, NIST) ran the Matrix-assisted laser desorption/ionization – time of flight (MALDI-TOF) for molecular weight (2 samples) given in the manuscript; Beilu Zhang (Ph.D. candidate in the Department of Chemistry), helped resynthesize several of the polymers sent to Dr. Ding for GPC analysis.

Chapter 5 contains some of the data given in the published manuscript "Peptide-Directed Self-Assembly of Functionalized Polymeric Nanoparticles Part II: Effects of Nanoparticle Composition on Assembly Behavior and Multiple Drug Loading Ability" in *Macromolecular Bioscience*. The authors are: Xu Xiang[a], Xiaochu Ding[a]*, Trevor Moser[b], Qi Gao[b], Tolou Shokuhfar[b] and Patricia A. Heiden[a]*. I certify that I replicated

the synthesis of the peptide-directed self-assembly of functionalized polymeric nanoparticles that were first synthesized by Xiaochu Ding in his Ph.D. project, and performed hydrodynamic tests (DLS) and prepared and measured the drug release profiles of a two-drug and three-drug scaffold, including the mathematical analyses needed to measure the drug release. Xiaochu Ding (now a post-doctoral researcher in the Department of Bioengineering, University of Pittsburgh) performed the original synthesis, and the other authors performed other characterizations and cell work.

Chapter 6 contains the manuscript "Polymer Modification of Fish Scale and their Nano-mechanical Properties" currently under-review for publication in *Journal of Applied Polymer Science*. The authors of the draft under consideration are: Xu Xiang[a]*, Fei Long[b], Ronald E. Kinnunen[c], Reza Shahbazian-Yassar[b] and Patricia A. Heiden[a]*. I certify that I designed the synthesis and performed all the research described in this manuscript except some of the AFM characterization of the modified fish scales were by Dr. Fei Long (Prof. Reza Shahbazian-Yassar's group, Department of Mechanical Engineering and Engineering Mechanics) but much of the AFM work was done by me with the assistance of Dr. Long.

# Acknowledgements

First of all, I would like to thank my advisor, Dr. Patricia A. Heiden. She is a very kind professor and teach me a lot. She educates and encourages me to develop the ability of solving the problems by myself. At the same time, she also help me improving my English skills, not only the writing, but also the speaking. Even most of the time, I did them worse than her expect. In these years of studying at Michigan Tech, she give me a lot of help in the research and also teach me how to become to a good teacher and a good researcher. All of these are benefited to me.

I also would like to thank my committee members Dr. Tarun K. Dam, Dr. Loredana Valenzano and Dr. Bruce P. Lee for their time, efforts and suggestions on my Ph.D. dissertation and defense.

I also want to thank my lab mates for their help: Ning Chen, Xiaochu Ding, Martha Barajas Meneses, Soha Albukhari and Beilu Zhang. I also want to thank Fei Long (for AFM, Department of Mechanical Engineering-Engineering Mechanics) and Prem L. Kashyap (for cooperation in chitosan project, ICAR-National Bureau of Agriculturally Important Microorganisms, India).

The help from all the staff in Chemistry Department who include Celine Grace, Denise Laux, Margaret Dunsten, Kelly Smith, Lorri Reilly, Andrew Galerneau, Aparna Pandey Jerry Lutz and Dean Seppala, is acknowledged.

At last, I would like to thank my parents for their love, encouragement and support during my Ph.D. study at Michigan Technological University.

# List of Abbreviations

| | |
|---|---|
| AFM | Atomic Force Microscopy |
| AIBN | 2, 2'-Azoisobutyronitrile |
| ATRP | Atom transfer radical polymerization |
| BDAT/TC1 | S, S'-Bis(α,α′-dimethylacetic acid) trithiocarbonate |
| BuMA | *n*-Butyl methacrylate |
| $^{13}$C NMR | Carbon-13 nuclear magnetic resonance |
| CP | Cloud point |
| CRP | Controlled radical polymerization |
| CTA | Chain transfer agent |
| DBF | 4',5'-Dibromofluorescein |
| DCM | Dichloromethane |
| DEGMA | Di (ethylene glycol) methyl ether methacrylate |
| $D_h$ | Hydrodynamic diameter |
| DIPEA | *N,N*-Diisopropylethylamine |
| DLS | Dynamic light scattering |
| DMAEMA | N, N-Dimethylaminoethyl Methacrylate |
| DMF | Dimethyl formamide |

| | |
|---|---|
| DMSO | Dimethyl sulfoxide |
| DMT Moduli | Derjaguin-Muller-Toropov moduli |
| DT1 | S-(Thiobenzoyl)thioglycolic acid |
| DT2 | 2-Cyano-2-propyl benzodithioate |
| DT3 | 4-Cyano-4-(phenylcarbonothioylthio) pentanoic acid |
| EAK16-II | AEAEAKAKAEAEAKAK a peptide sequence |
| ECM | Extracellular matrix |
| EMC | Equilibrium Moisture Content |
| EG | Ethylene glycol |
| EGMA | (Ethylene glycol) methyl methacrylate |
| EtOAc | Ethyl acetate |
| FL | Fluorescein |
| FS | Fish scale |
| FTIR | Fourier transform infrared spectroscopy |
| GNP | Gold nanoparticle |
| GPC | Gel permeation chromatography |
| HATU | 2-(7-Aza-1-H-benzotriazol-1-yl)-1,1,3,3-tetramethylaminium |
| HAP | Hydroxyapatite |

| | |
|---|---|
| HCl | Hydrochloric acid |
| HDA | Hetero-Diels-Alder reaction |
| $^{1}$H NMR | Proton nuclear magnetic resonance |
| LCST | Lower critical solution temperature |
| MA | *tert*-Butyl methacrylate |
| MALDI-TOF | Matrix-assisted laser desorption/ionization - time of flight |
| MMA | Methyl methacrylate |
| MW | Molecular weight |
| NaOH | Sodium hydroxide |
| NF | Nitrofurazone |
| NP | Nanoparticle |
| OEGA | Oligo (ethylene glycol) methyl ether acrylate |
| P1 | H2N-TTTT-AEAEAEAE-amide a peptide sequence |
| P2 | H2N-TTTT-AKAKAKAK-amide a peptide sequence |
| PBS | Phosphate-buffered saline |
| PDI | Polydispersity index |
| PMA | Poly (*tert*-Butyl methacrylate) |
| PMMA | Poly (methyl methacrylate) |

| | |
|---|---|
| PNIPAM | Poly (*N*-isopropylacrylamide) |
| POEGA | Poly (Oligo (ethylene glycol) methyl ether acrylate) |
| POSS | Polyhedral oligomericsilsesquioxane |
| PVP | Poly (1-Vinyl-2-pyrrolidinone) |
| RAFT | Reversible addition fragmentation chain transfer |
| SFRP | Stable free radical mediated polymerization |
| TC1/BDAT | S, S'-bis(α,α′-dimethylacetic acid) trithiocarbonate |
| TC2 | Dibenzyl Trithiocarbonate |
| TDT | 1,3,5-Benzenetricarbodithioic acid / 1,3,5-tris(phenylmethyl) ester |
| TEOS | Tetraethyl orthosilicate |
| TGA | Thermogravimetric analysis |
| UCST | Upper critical solution temperature |
| VP | 1-Vinyl-2-pyrrolidinone |

# Abstract

This research has three parts. Two parts deal with novel nanoparticle assemblies for drug delivery, and are described in Part A, while the third part looks at properties of fish scales, an abundant and little-used waste resource, that can be modified to have value in medical and other areas.

Part A describes fundamental research into the affects of block sequence of amphiphilic block copolymers prepared from on a new and versatile class of monomers, oligo(ethylene glycol) methyl ether acrylate (OEGA) and the more hydrophobic di(ethylene glycol) methyl ether methacrylate (DEGMA). Polymers from these monomers are biologically safe and give polymers with thermoresponsive properties that can be manipulated over a broader temperature range than the more researched N-isopropylacrylamide polymers. Using RAFT polymerization and different Chain Transfer Agents (CTAs) amphiphilic block copolymers were prepared to study the effect of block sequence (hydrophilic OEGA and more hydrophobic DEGMA) on their thermo-responsive properties. Pairing hydrophilic chain ends to a hydrophobic DEGMA block and hydrophobic chain ends to hydrophilic blocks ("mis-matched polarity") significantly affected thermoresponsive properties for linear and star diblock copolymers, but little affected symmetric triblock copolymers. Specifically matching polarity in diblock copolymers yielded nanoparticles with higher cloud points (CP), narrow temperature ranges for coil collapse above CP, and smaller hydrodynamic diameter than mis-matched polarity. Using this knowledge two linear OEGA/DEGMA diblock copolymers were prepared with thiol end groups and assembled into hybrid nanoparticles with a gold nanoparticle core (GNP-polymer hybrids). This design was made using the hypothesis

that a hybrid polymer drug carrier with a high CP (50-60 ˚C) and a diblock structure could be designed with low levels of drug release below 37 ˚C (body temperature) allowing the drug carrier to reach a target (tumor) site with minimal drug loss and accompanying side effects, to healthy tissue. Once at a tumor site safe wavelengths of light could heat the gold core and polymer domain to above the CP releasing the bulk of the drug where it is needed. The results were promising but suggested additional modification of the copolymer is required to further reduce release low temperature drug release. The second half of Part A addressed multi-drug controlled release from tissue scaffolds prepared from "nanoparticle fibers". Tissue scaffolding for cell regeneration requires the ability to both physically support cells and promote their growth. This may require a drug "cocktail" of low or high molecular weight drugs to be released at different rates depending on the therapeutic levels needed for each drug. This work succeeded in producing a novel, flexible, and robust system of assembled fibers of nanoparticles that could independently control the release of multiple drugs.

Fish scale is an abundant and growing waste resource, with supplies far exceeding current uses, which have focused on harvesting the components of scales (hydroxyapatite and collagen) and ignored the scale itself. No studies have looked at the chemical modification of the intact scales, but such modifications may make scales suitable and even desirable additives into polymers for new composites with useful applications. Part B of this research investigated chemical modification of fish scales, characterized the changes to the upper biomineral layer and inner collagen layer, and the effects of these modifications on nanomechanical properties and moisture uptake. We described some possible uses for modified scales.

# Chapter 1 Introduction

This dissertation has two major divisions. The first major division addresses two novel drug delivery systems design, and is described in Chapters 3, 4 and 5. The second major division is a fundamental study of the chemical modification and nano-mechanical analysis of fish scale, an abundant waste resource, and is described in Chapter 6.

Chapter 3 describes a fundamental study of the affect of end group polarity and block sequence on the thermoresponse properties of novel amphiphilic block copolymers from a new class of ethylene glycol-containing (meth)acrylates. Polymers from these monomers have recently become of interest because of their broad temperature range over which their cloud points (CPs) can be manipulated. Their block copolymers were investigated here as possible vehicles to address a a major challenge in the the area of drug delivery, which is to reduce the quantity of drug, particularly toxic drugs like chemo-therapy, that escape from nanoparticles when they are not at their target site. Diblock star copolymers and linear di- and triblock copolymers of hydrophilic oligo(ethylene glycol) methyl ether acrylate (OEGA) and more hydrophobic di(ethylene glycol) methyl ether methacrylate (DEGMA) monomers were prepared by RAFT polymerization with Chain Transfer Agents (CTAs) providing the end groups. The affect of matching or mis-matching chain end polarity and block sequence was studied on the hydrodynamic diameter, cloud point, and temperature range of the chain collapse on linear di- and triblock copolymers and star diblock polymers. The affects of matching or mis-matching chain end polarity were significant with linear diblock copolymers but more complex with triblock and star copolymers. This study allowed us to determine that

amphiphilic diblock copolymers of hydrophilic OEGA and more hydrophobic DEGMA with "matched" chain end polarity gave copolymers with higher CP, smaller hydrodynamic diameter, and narrower transition window than "mis-matching" polarity.

The results from this study were used to design and test a gold nanoparticle(GNP)-polymer hybrid as a novel "high-efficiency" thermoresponsive drug delivery carrier, as described in Chapter 4. Typically thermo-responsive drug-delivery polymers are selected with CPs near the temperature of the human body (37 ˚C), which means drug begins being released immediately when introduced into the body, whether or not it is at the target site. The rationale behind this design was that GNPs can absorb a bio-safe wavelegth of light and convert it to heat, thereby heating the GNPs local environment. When the temperature exceeds the polymer's cloud point, the drug is released. We prepared and studied two amphiphilic "matched" diblock copolymers with CPs between 50-60 ˚C whose end groups were selected so that the chain end bonded to the hydrophobic (drug carrier) block was thiol (T) to bond to the gold core, while the polar chain end was a $–CO_2H$ (C) which could ultimately be bonded to a targeting ligand. The two polymers were: T-$D_{50}O_{50}$-C (CP = 51.5 ºC) and T-$D_{40}O_{60}$-C (CP =59.8 ºC) and their GNP hybrids. The thero-responsive properties, composition, and end groups were verified by UV-vis hydrodynamic diameter, IR spectra, NMR spectra, drug loading (ibuprofen), and drug release were determined. The drug release profiles were measured at 4 different temperatures to understand how the thermoresponsive properties affect the releasing rate and efficiency. At 0.5 h time point, the release percent was from 16.7% to 39.7% correspondence 20 ºC to 60 ºC, and it increased to 57.0% ~ 94.8% at 24 h. Although the low temperature drug release was still considered too high, the results were

promising, and showed that a larger hydrophobic core reduces early drug loss. Further studies are needed to improve polymer design for further reductions in early drug release.

A novel multi-drug release tissue scaffold was studied in Chapter 5 to address another remaining challenge in drug delivery, i.e. the ability for a single scaffold device to simultaneously contain and independently control the release of multiple drugs, so each drug can be released and maintained at a therapeutic but non-toxic level. This work builds on the prior research from our group (Dr. Xiaochu Ding), who first synthesized and functionalized drug-containing nanoparticles with peptides and self-assembled these into continuous nanoparticle fibers and three-dimensional (3D) scaffolds. Ideally each drug is loaded into a "custom" nanoparticle composition the releases that drug at a suitable rate. The number and placement of these nanoparticles can be controlled by controlling the number of each nanoparticle and its assembly sequence. The novelty of this work was preparing and proving control over assembly sequence with three different model drug-containing nanoparticles, and quantifying the independent release of each drug from the scaffold. This type of nanoparticle scaffold combines the advantages of peptide self-assembly and the versatility of polymeric nanoparticle controlled release systems for tissue engineering.

The second part of the dissertation was focus on a new biomaterial: fish scale. Fish scales are an abundant yet underutilized waste resource, with supplies far exceeding current uses. Current use for scales separate the main components for individual use, which sacrifices the properties inherently built into the scale through its hierarchical structure. Most research studies also focus on scale components, though recent research has studied

hierarchical scale designs. No prior studies have looked at the chemical modification of the scales themselves. Here, we used some basic chemical modifications of intact scales, and sought to preferentially degrade or enhance one of the two scale domains. The chemical, nanomechanical, and moisture uptake changes in the scale domains were tested to highlight pathways to potential property enhancements to suggest new applications for fish scale waste, and may benefit from the existing hierarchical scale design. The results from this research show that different domains can be preferentially (but not exclusively) modified and the modulus can be tuned over a broad range, however, all modifications resulted in increasing the moisture uptake of the scales compared to unmodified scales, indicating some structural damage to the scales despite modifications that increased modulus.

# Chapter 2 Introduction of RAFT Polymerization

## 2.1 Introduction

### 2.1.1 Controlled radical polymerization and RAFT polymerization

Since the first report by Otsu and co-workers[1] opened the door to Controlled Radical Polymerizations (CRP) it has become one of the most important polymer synthetic methods. This is because CRP allows previously difficult to prepare or even unobtainable polymers to prepare that have a desired microstructure such as diblock or triblock copolymers, controlled molecular weight, and narrow molecular weight distribution[1]. The most researched CRP methods are stable free radical mediated polymerization (SFRP), atom transfer radical polymerization (ATRP) and reversible addition fragmentation chain transfer (RAFT) polymerization. Each of these methods has certain advantages and disadvantages, but they all permit a greater degree of control over molecular weight (MW), monomer sequence, and polydispersity index (PDI) compared to non-controlled radical polymerization. The RAFT process appeared in the literature in the early 1970s[1] but in 1998 the use of dithioester chain transfer agents (CTA) was reported and spurred research into the RAFT polymerization method[2]. RAFT polymerization requires the use of both a traditional radical initiator as well as a CTA. Figure 2.1 shows two common types of CTA used to produce linear polymers (Z and R are function groups).

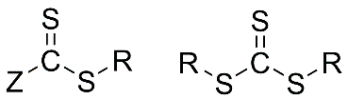


Figure 2.1 Generic structures for a Dithioester and a Trithiocarbonate RAFT CTA.

RAFT affords the typical advantages often associated with CRP, i.e. control over end group[3] [4], MW[5] and monomer sequence[6]. However, unlike other CRP methods, RAFT tolerates a very wide range of monomers, including functional monomers, such as acids and their salts, alcohols, and tertiary amines[2] (Figure 2.2). However monomers bearing nucleophilic functional groups, such as primary or secondary amines, may cause unwanted decomposition of the RAFT moiety during polymerization[4].

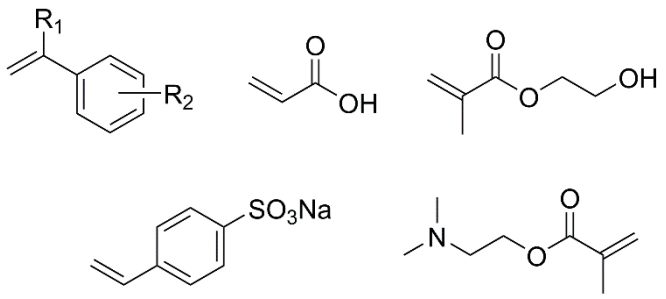


Figure 2.2: Generic families of monomers suitable for RAFT polymerization

RAFT polymerization also occurs under simple and environmentally friendly conditions, proceeding in water at room temperature without the need for protecting groups. Aqueous RAFT polymerization is well-suited for the synthesis of nano- and micro- scale self-assembled polymers, which can be useful in electronics and biotechnology[7] [8].

### 2.1.2 Mechanism of RAFT Polymerization and Formation of End groups

The commonly accepted mechanism of RAFT polymerization is shown in Figure 2.3. Based on the equilibrium, end group control can be achieved through the choice of different kinds of CTAs[3]. Selecting a dithioester, such as that shown in Figure 2.1, gives a

$CS_2Z$ and R as the polymer chain end groups. Both of these groups also affect the final polymer properties, as well as aspects of the polymerization kinetics as shown in Figure 2.3. Specifically, step two illustrates the initial equilibrium and re-initiation step, and in this step the Z group influences the addition rate. For example, Z groups with a conjugating structure will stabilize the radical on the carbon, slowing the fragmentation step. At the same time, the R group also plays a role in the fragmentation process by determining the strength of the S-R bond and the stability of the R• radical after fragmentation. That in turn affects the breaking and reforming of the S-R bond. If R• is unstable, the fragmentation process is slow because the high energy of activation favors maintaining the S–R bond. However, at the same time, because the R• is unstable, when it is formed it possesses a higher reaction rate between R• and the monomer. There is a balance between these two effects. In step three, the main equilibrium step, the R group has bonded to a monomer and functions as the unreactive end group of a growing polymer chain. Therefore, it is the Z group that plays an important role in the propagation (monomer addition) rate. By appropriate selection of the R and Z groups, the overall polymerization rate can be controlled. However, like most free radical reactions, the overall rate of a RAFT polymerization is controlled by multiple factors in the system, including steric and polar factors, solvent, reactant concentration and reaction temperature.

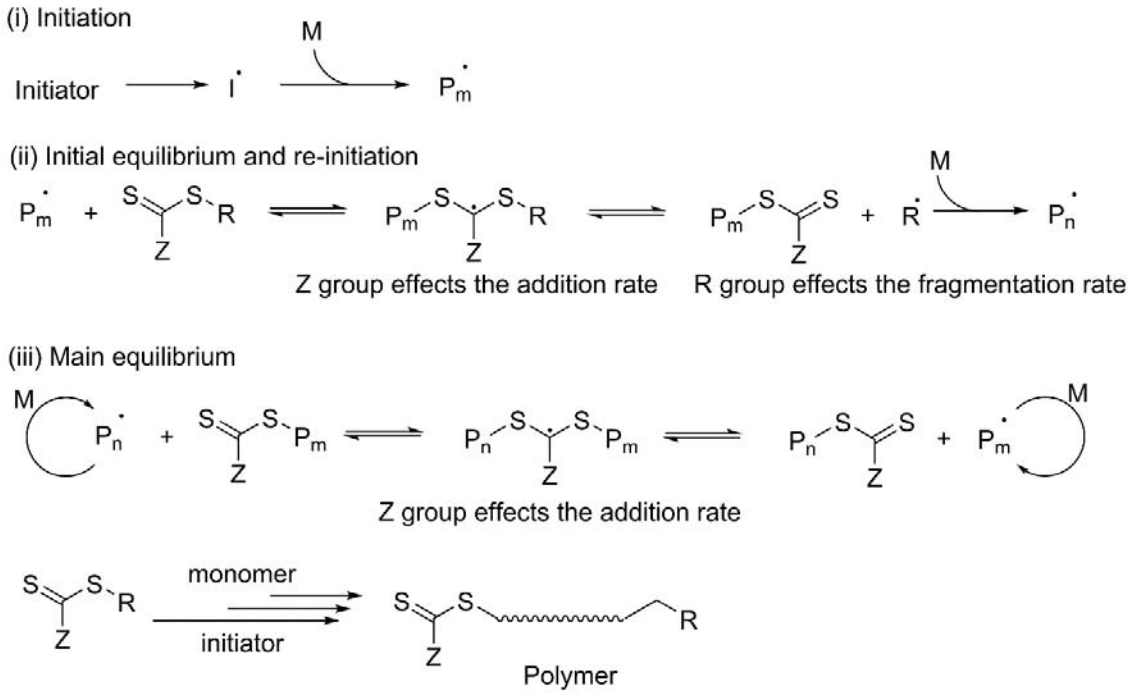


Figure 2.3: Schematic of RAFT polymerizations

In RAFT polymerization, the two chain ends are designated as α- and ω- (Figure 2.4). Most chain ends arise from the Z (the ω- end) and R (the α- end) groups of the CTA. Consequently, the simplest way to achieve the desired chain ends is to employ a CTA with these end groups, but if that is not possible many CTA end groups are easily modified after polymer synthesis to give the desired chain ends. Both approaches are well represented in the literature.

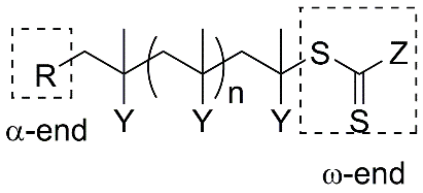


Figure 2.4: End groups of RAFT polymerizations

In the RAFT mechanism, the radical initiator (I• in Step 1 of Figure 2.4) and R group on the CTA give α- chain ends, while the ω- chain ends are from the CTA only. Various post polymerization modifications have been performed on both the α- and ω-end, but because all chains are likely to have an ω-end from the CTA, it is more common to remove or modify this end than the α-end.[4, 9]

## 2.2 CTA Synthesis

### 2.2.1 Single functional CTAs of the $ZCS_2R$ type

Four families of CTAs of the $ZCS_2R$ type have been reported, with the family being determined by the identity of the Z activating group. In the dithioesters Z = an aromatic or aliphatic group. In xanthates Z = $–NR_2$, while in trithiocarbonates Z= –SR, and in dithiocarbamates Z = –OR. Every CTA includes a free-radical leaving group (R) and an activating group (Z). The structural effects of the Z group on reactivity were studied in 2003.[10] It was found that the N and O atoms in xanthates and dithiocarbamates can participate in resonance stabilization with the C=S double bond (Canonical forms: Figure 2.5). These resonance structures affect the radical reactivity and therefore these CTAs give somewhat poor control of molecular weight[10-11]. Consequently, this introduction emphasizes recent studies with dithioesters and trithiocarbonates.

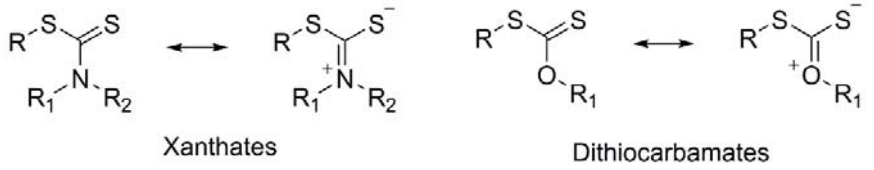


Figure 2.5: Canonical forms of xanthates and dithiocarbamates

### 2.2.1.1 Dithioester CTAs:

Dithioesters were reported in 1998 as RAFT CTAs[2] and now are the most commonly used CTAs in RAFT. Dithioesters possess a simpler structure than trithiocarbonates, xanthates, and dithiocarbamates, and they are easy to synthesize. Dithioesters are commonly synthesized via Grignard reagents, phosphorous pentasulfide ($P_4S_{10}$), and Davy-R reagents, as illustrated below.

#### *2.2.1.1.1 Grignard route:*

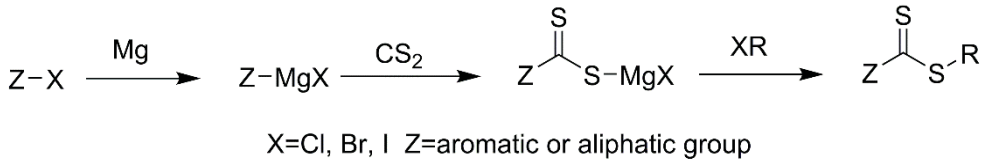


Figure 2.6: General procedure to dithioester CTAs by Grignard route

The Grignard route is simple and versatile and used to synthesize many thiocarbonyl compounds (Figure 2.6). Dithioesters are readily obtained by reaction of Grignard agents with halogenated compounds, so this method is often used for RAFT CTA synthesis (Figure 2.7, CTA1-CTA4). A dithiobenzoic acid intermediate can also be obtained by treating the $PhCS_2MgX$ intermediate with aqueous HCl [12]. Dithiobenzoic acid is not stable at room temperature so it should be stored at or below –20 $^{o}$C. Many reagents can be reacted with dithiobenzoic acid to access a great variety of different CTAs. In summary, the Grignard reaction is a valuable and versatile route to RAFT CTAs, but because Grignard reagents are sensitive to oxygen and water, the reaction conditions must be scrupulously controlled.

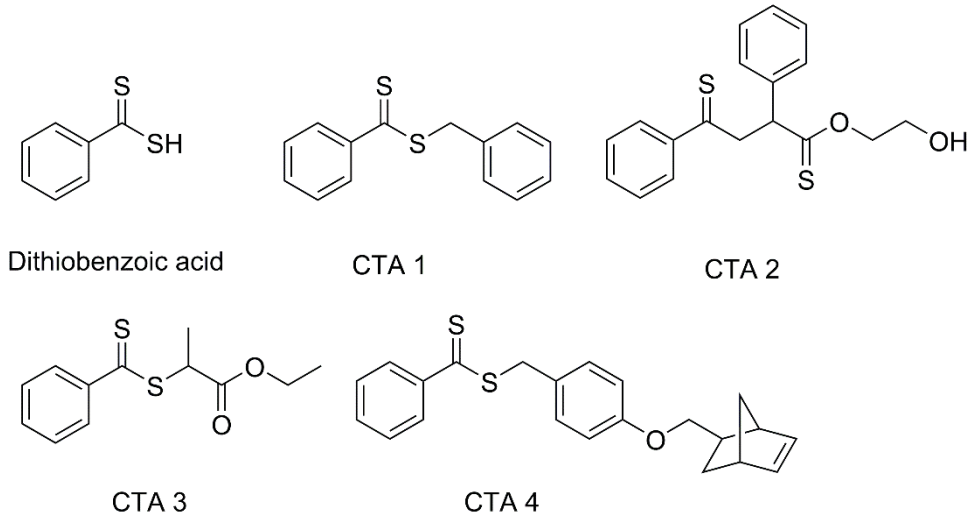


Figure 2.7: CTAs synthesized by a Grignard route

*2.2.1.1.2 Synthesis of CTAs from benzoic acid and $P_4S_{10}$ or Davy-R reagents:*

While the Grignard route is simple and versatile it does require careful control over the reaction conditions. CTA syntheses using $P_4S_{10}$ or Davy-R reagents require less stringent synthetic conditions. Figure 2.8 outlines four different routes to multifunctional dithioester CTAs, starting with reaction of benzoic acid and $P_4S_{10,}$ giving a transient dithiobenzoic acid. This is converted to the desired CTAs in a single step[13]. A great many thiols and alcohols have been reacted with carboxylic acids using $P_4S_{10}$ to give many different CTAs[12 14]. Three of the paths outlined in Figure 2.8 (paths A, B and C) proceed by a radical exchange process, while path D is a nucleophilic reaction. As stated, these routes occur in a single step and give high yields.

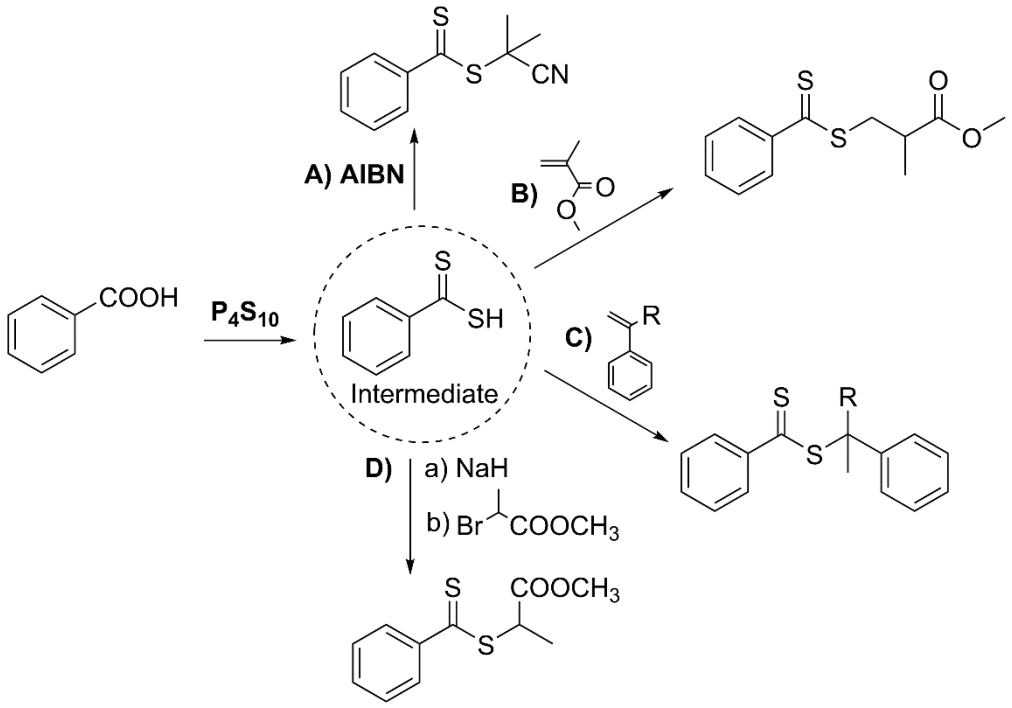


Figure 2.8: Synthesis of CTAs from $P_4S_{10}$ (Adapted from Angew. Chem. Int. Ed. 2003, 42, 2869-2872)

The Davy-R process, shown in Figure 2.9, is similar to the process using $P_4S_{10}$, and offers another route to synthesize dithioester CTAs.[12]

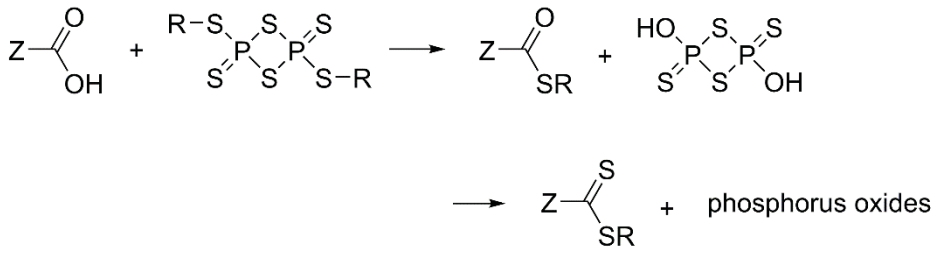


Figure 2.9: Synthesis of CTAs using a Davy-R reagent.

*2.2.1.1.3 Other methods*

Radical exchange processes are a powerful, but often less efficient method to synthesize new CTAs. In this approach excess radicals (R'•) are used to replace the R group of an

existing dithioester moiety (-SR)[10, 15]. This process is illustrated in Figure 2.10 and two examples of its use are given in Figure 2.11. Radical exchange processes can also be used in the synthesis of xanthates, as described elsewhere in 2006[16].

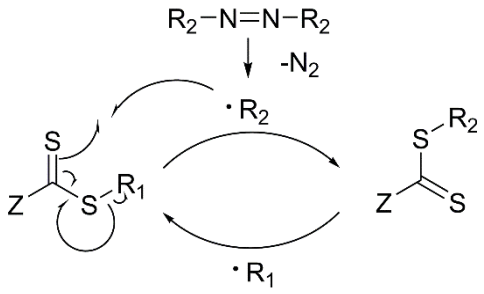


Figure 2.10: Radical exchange process

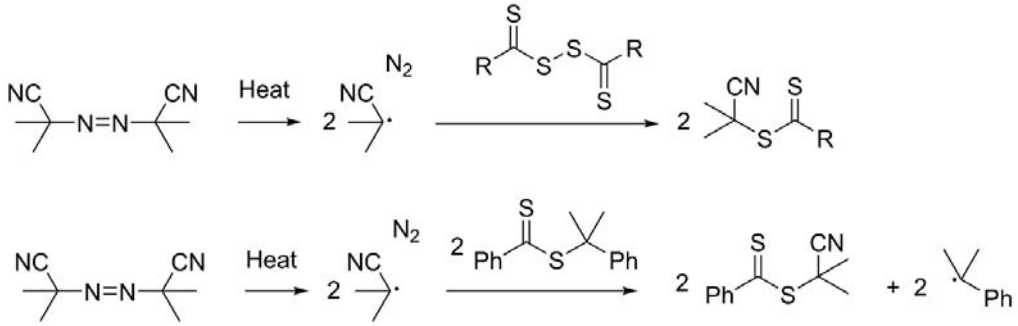


Figure 2.11: Examples of radical exchange

### 2.2.1.2 Trithiocarbonate CTAs:

Trithiocarbonates are also commonly used CTAs in RAFT polymerization. A typical synthetic procedure is shown in Figure 2.12.

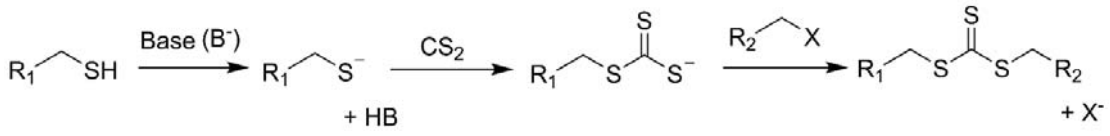


Figure 2.12: Procedure to synthesize trithiocarbonate CTAs

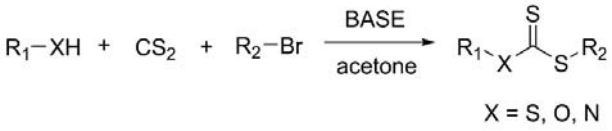


Figure 2.13: Xanthates and dithiocarbamates

This method can also be used to give xanthate and dithiocarbamate CTAs (Figure 2.13). Skey and O'Reilly studied this method for the synthesis of trithiocarbonate CTAs (Figure 2.14, CTA5-CTA13), dithiocarbamates (Figure 2.14, CTA14-CTA16), and xanthates (Figure 2.14, CTA17-CTA19). They reported this as a high yield method for synthesizing functional CTAs[17].

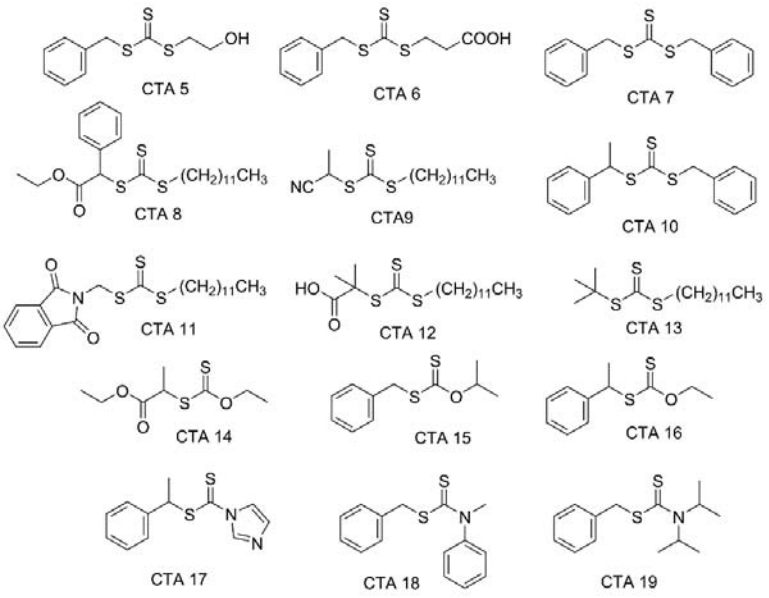


Figure 2.14: Trithiocarbonate CTAs

In dithioester CTAs, only one reactive site is present to react with monomer, however, trithiocarbonate CTAs possess two active sites. If $R_1$ and $R_2$ are the same, both sites are equally reactive and a symmetrical polymer is formed. Figure 2.15 outlines a convenient one-step method that is, however limited to the synthesis of a symmetrical CTA with two

carboxylic acids[18]. If the R groups are not equally reactive, the reaction rates will of course differ, and indeed it is even possible that only one of the sites will be activated. The above methods can be used to synthesize asymmetric CTAs if desired. The physical properties of a symmetrical polymer will of course differ from those of an asymmetrical structure.

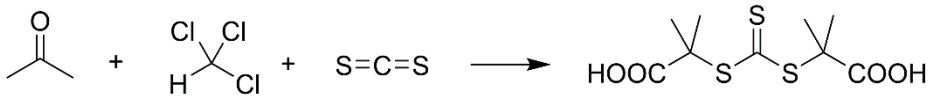


Figure 2.15: Synthesize the symmetry CTA with two acid group as ends

## 2.2.2 Multi-functional CTAs

Several types of multi-functional CTAs have been designed to permit the RAFT-synthesis of more complex polymer architectures, such as star or graft polymers. The two major types of multi-functional CTAs are $R(CS_2R')_n$, which give star polymers, and $R_1CS_2R_2CS_2R_3$, which give linear or graft polymers.

### 2.2.2.1 CTAs for Star Polymers: $R(CS_2R')_n$

Figure 2.16 outlines the synthesis of a trifunctional RAFT CTA that will function as a core molecule to give a three arm star polymer. The trifunctional CTA is synthesized by reacting a trifunctional carboxylic acid with a benzylic mercaptan and $P_4S_{10}$. However, this route is susceptible to side reactions and so gives low yields.[13]

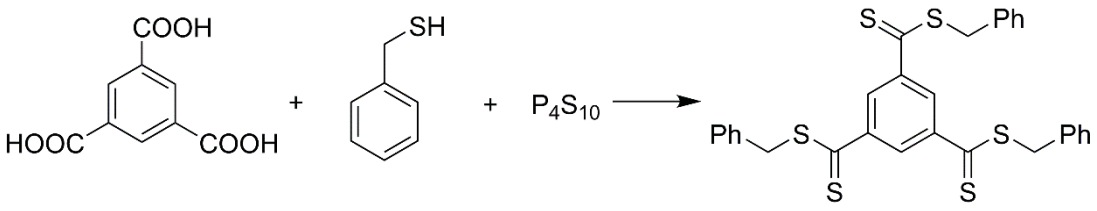


Figure 2.16: Trifunctional star CTAs

### 2.2.2.2 Linear Multifunctional CTAs: $R_1CS_2R_2CS_2R_3$

Linear multi-functional CTAs have been synthesized using a method that is similar to the trithiocarbonate CTA synthesis. These CTAs allow the synthesis of more complex linear polymeric structures[19] (Figure 2.17).

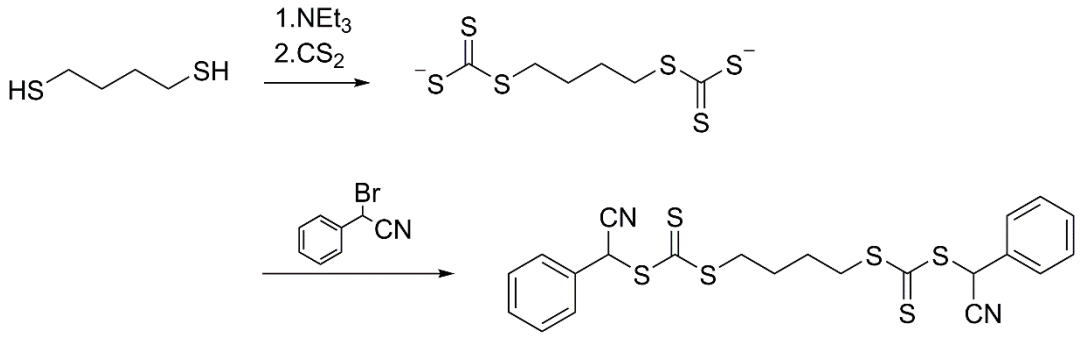


Figure 2.17: Linear multi-functional CTA synthesis

There are two trithiocarbonate groups in one CTA. So, there are four reaction sites (shown in Figure 2.18) that can be utilized that arise from these two trithiocarbonate functional groups. The monomers will add to the site that forms the more stable radical. For example, in Figure 2.18, the polymerization will happen only at the site that gives the PhCH• (CN) radical.

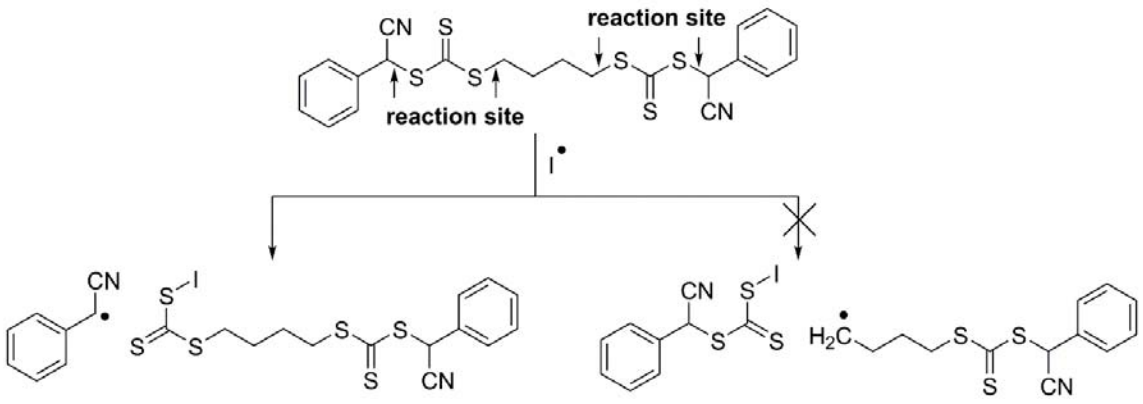


Figure 2.18: Illustration of the potentially active sites and the preferred reactive site.

Bivigou-Koumba, et *al.* researched this type of CTA[20] in detail. They synthesized seven CTAs (CTA 20 – CTA 26, shown in Figure 2.19) and tested their reaction activity. They found that these CTAs yielded polymers with different end groups and different molecular weights when they were used despite following the same polymerization procedure. For example, a comparison of the polymer resulting from CTA 23, which has electron-donating methyl ether end groups, with the polymer resulting from CTA 25, which has electron-withdrawing perfluoro end groups, shows that the polymer from CTA 23 has only half the molecular weight of the polymer resulting from use of CTA 25. The mechanism that explains why the molecular weight of the polymers from these two CTAs is different is shown in Figure 2.20. When initiator is added, CTA 23 breaks down into two other CTAs: CTAy and CTAz (Figure 2.20). This means the CTA 23 is effectively present at twice the concentration of CTA 25, which accounts for the molecular weight difference. The X group on the benzene ring of this kind of CTA decides the reaction orientation. H (CTA 21) and $CH_3O$ (CTA 23) as electron-donating groups, induce this side reaction while electron-withdrawing groups like $CF_3$ (CTA 25) block it.

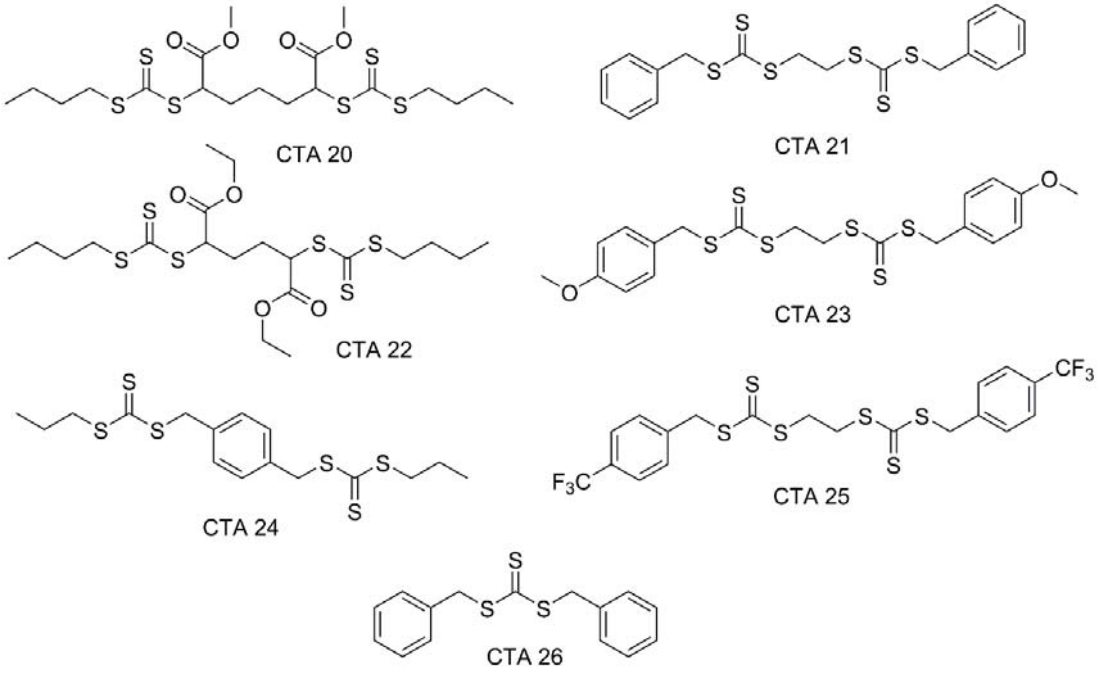


Figure 2.19: Linear multi-functional CTAs

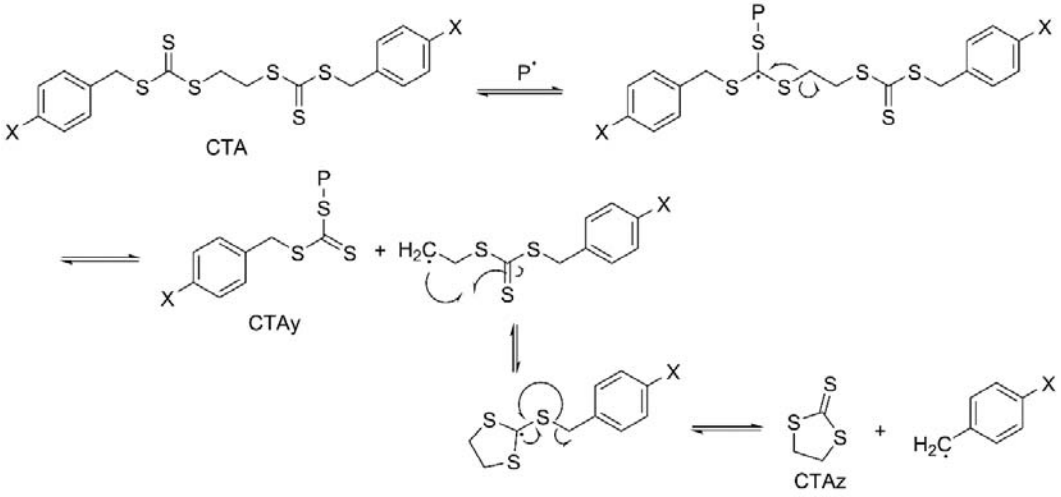


Figure 2.20: Illustration of the side reactions of CTA 21 and CTA 23 that lead to different polymer products from multi-functional CTAs

### 2.2.3 Macro-CTAs

In RAFT polymerization, dithioester or trithiocarbonate functional groups are typically the preferred CTAs. Researchers have also been interested in macro-CTAs, and opted to prepare these by assembling smaller CTAs. For example, Wang et *al.* coupled hepta (3, 3, 3-trifluoropropyl) polyhedral oligomericsilsesquioxane (POSS) with a trithiocarbonate CTA via reaction with its end group[18a] (Figure 2.21). Using this macro-CTA, they then prepared a new physical hydrogel.

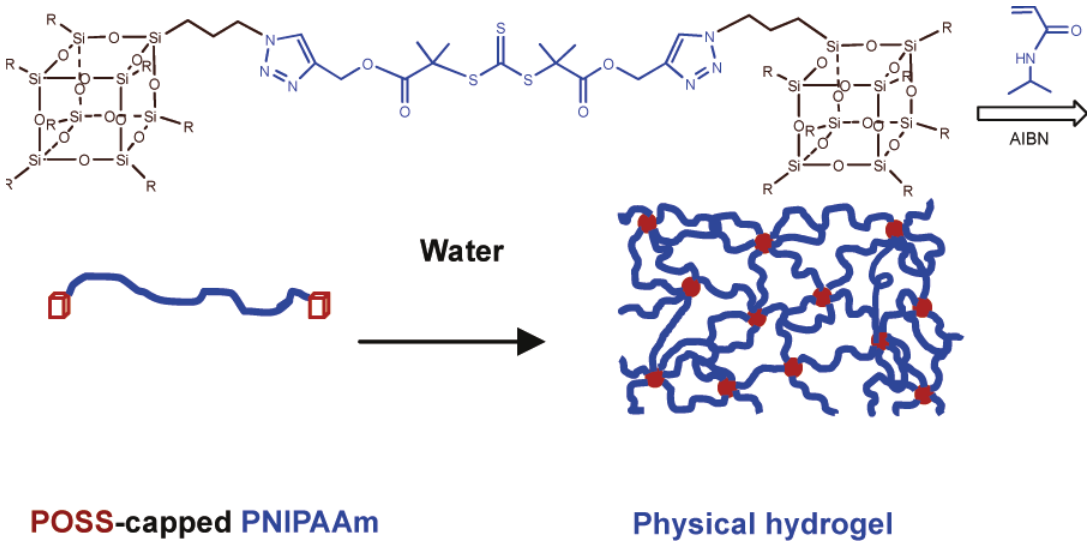


Figure 2.21: Use of a macro-CTA (Copied from ACS Appl. Mater. Interfaces, 2011, 3(3), 898-909. See Appendix D for a copy of the copyright transfer agreement.)

To gain improved polymer properties, researchers also studied coupling CTAs to solid supports. Polymerization of this kind, where the supported CTA is the site of a polymer chain's growth, is called a "grafting-from" approach (Figure 2.22). This approach may require modification of the surface of the support particle, so that it can function as a

CTA. GNPs[21], carbon nanotubes or graphene[22] and resin[23] have all been reported as solid supports for RAFT polymerization.[24]

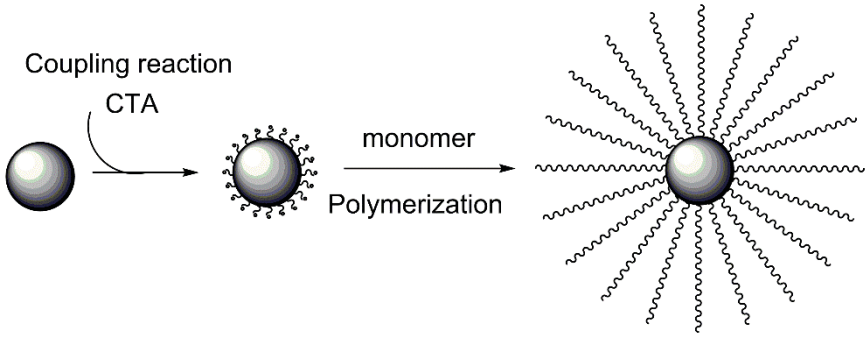


Figure 2.22: A "grafting-from" approach

## 2.3. Polymer end-group removal and modification

The most common process to control chain end group identity, other than selecting a CTA with the desired end group, is removal and/or modification of an existing chain end. There are four main approaches to remove or modify the $CS_2Z$ group, as illustrated in Figure 2.23[4].

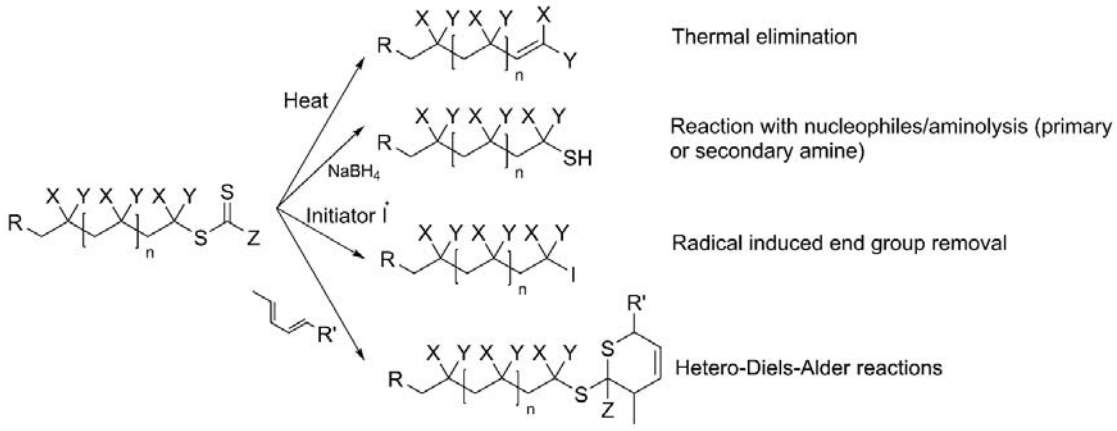


Figure 2.23: End group modifications (Adapted from Polym. Chem., 2010, 1, 149-157)

Thermal elimination and radical induced end group removal can yield sulfur free end groups. Thermal elimination has the advantage of needing no additional chemicals, but does require that the polymer and any functional groups on that polymer be stable at the reaction temperature. Thermal elimination is typically accomplished at 120-200$^{o}$C. Postma et *al.* described thermolysis of RAFT-synthesized polymers in 2005[25] (Figure 2.24). The weight loss profile observed by Thermogravimetric Analysis (TGA), as well as the mechanism of loss, were shown to depend strongly on both the RAFT agent being eliminated and the structure of the polymer backbone. A more detailed study was published in 2006[26]. The course of thermolysis of poly(methyl methacrylate) (PMMA), prepared with dithiobenzoate and trithiocarbonate RAFT agents, was followed by TGA, 1H NMR spectroscopy, and gel permeation chromatography (GPC).

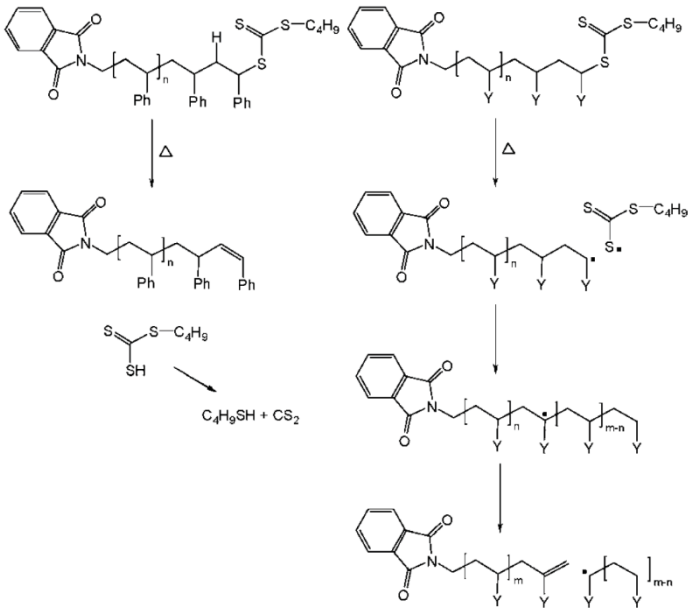


Figure 2.24: Thermolysis of RAFT-synthesized polymersm (Copied from Polym. Chem., 2010, 1, 149-157. See Appendix D for a copy of the copyright transfer agreement.)

Radical induced end group removal involves the exchange between the initiator and RAFT end group. This mechanism is shown in Figure 2.25.

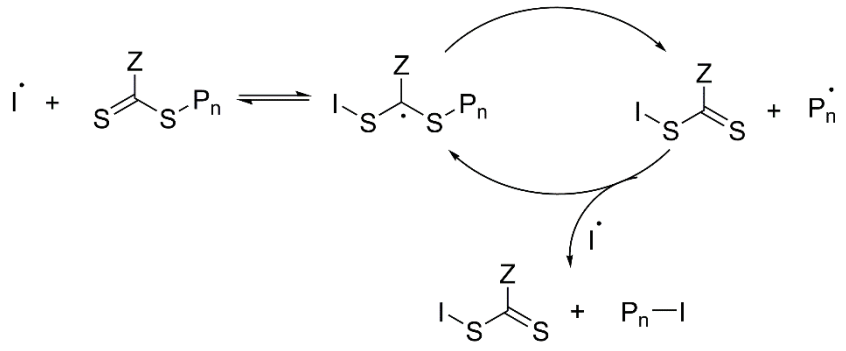

Figure 2.25: Mechanism of radical induced end group removal

Another end group modification involves reaction of dithioester groups with excess amine or reducing agents, such as $NaBH_4$. This is one of the most widely used and versatile methods of RAFT end group conversion. By this method, it is easy to convert a dithioester group to a thiol (-SH). This modification affords a good route to attach RAFT polymers to nanoparticles, such as gold nanoparticles (GNP), as shown in Figure 2.26 [27].

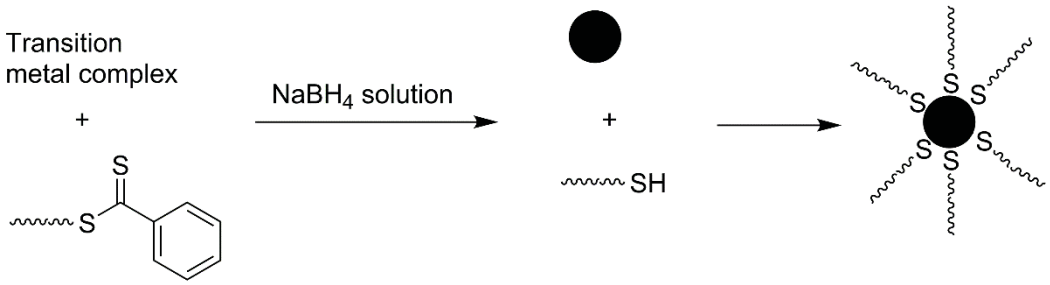


Figure 2.26: Metal nanoparticles attached to RAFT-synthesized polymer via thiol groups (Adapted from Polym. Chem., 2010, 1, 149-157)

Polymer modified gold nanoparticles have great potential for use in advanced materials. Compared with other polymerization methods, RAFT polymerization has several

advantages for making a covalent bond to metal nanoparticles like GNPs[21]. There are three main preparative approaches for polymer/gold nanocomposites based on covalent linkages, as illustrated in Figure 2.27. A "grafting-from" approach was mentioned in the last section (Macro-CTA).

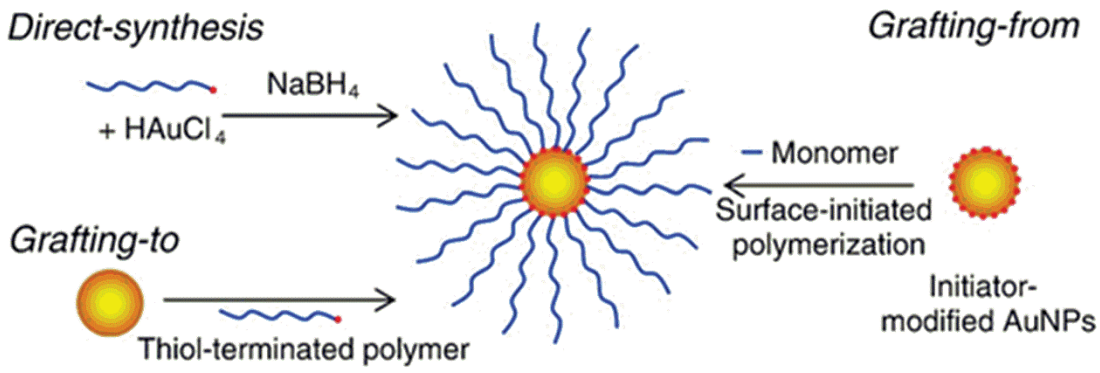


Figure 2.27: Three main approaches for polymer/gold nanocomposites (Copied from Advances in Colloid and Interface Science, 2009, 149, 28-38. See Appendix D for a copy of the copyright transfer agreement.)

Finally, Hetero-Diels-Alder (HDA) reactions can be used to modify the thiocarbonylthio group of the RAFT polymer, illustrating a RAFT-HDA click conjugation method as reported by Inglis, et *al.* at 2009[28].

# Chapter 3 End Group Polarity and Block Symmetry Effects on Cloud Point and Hydrodynamic Diameter of Thermoresponsive Block Copolymers[a]

## 3.1 Introduction

Stimuli-responsive (co)polymers are "smart" materials that undergo significant conformational changes when environmental conditions are changed appropriately.[1] Typical stimuli include change in temperature[2], pH[3], intensity of light[4] and humidity[5]. These materials have been extensively investigated for biomedical uses, especially for drug (or other active ingredient) delivery.[6] Thermoresponsive materials that possess a "lower critical solution temperature" (LCST) are of interest as drug delivery vehicles.[2a] The LCST is usually approximated as the cloud point (CP) of a solution, and is measured by a change in light transmission resulting from phase separation of the polymer from the solvent.

The CP of a polymer depends on the balance between changes in enthalpy arising from hydrogen bonding between water and polymer and entropy when this bonding is broken and the water molecules are no longer ordered around the polymer[7]. Specifically this means that the CP is not only controlled by polymer composition but to a greater or lesser degree on the degree of polymerization, polydispersity, end groups, and architecture.[8] For a given composition it can also vary with the concentration of the solution being tested. However, the magnitude of each of these effects depends on the specific polymer being studied.[8f, 9] For example poly(*N*-isopropylacrylamide) (PNIPAM)[9], which is probably the

[a] The material contained in this chapter was previously has been accepted for publication in *Journal of Polymer Science Part A: Polymer Chemistry*.

most studied stimuli-response polymer, has a CP that is relatively independent of molecular weight and end group. For example, the CP of PNIPAM with *tert*-butyl and methyl end groups and a 30-fold difference in molecular weight, $1.78 \times 10^4$ g/mol versus $4.75 \times 10^5$ g/mol, had less than 1 ˚C difference, i.e. 30.83 ˚C to 30.18 ˚C. In fact, the influence of various chain end groups (*tert*-butyl, methyl, trityl and amide) on the CP of PNIPAM was similarly negligible, ranging from only 29.74 ˚C to 30.83 ˚C. PNIPAM backbones may be relatively unaffected by these changes because the repeat unit contains amide groups, so the effects of two end groups that both interact with the same homopolymer domain, are relatively insignificant. This may also explain why more flexible thermoresponsive polymers show more significant effects from changes in end group identity.[10]

Studies of linear and branched PNIPAM copolymers with an imidazole co-monomer showed significant effects of architecture on CP.[11] Depending on the monomer composition, the CP of the linear PNIPAM copolymers ranged from 32 ˚C to 20 ˚C, while the CP of the different branched PNIPAM copolymers ranged from 29 ˚C to 11 ˚C. The CP declined as the imidazole co-monomer content rose in both linear and branched copolymers. These copolymers were made using reversible addition−fragmentation chain-transfer (RAFT) polymerization, giving polymers asymmetric end groups, but the reduction in CP is primarily attributed to the imidazole groups forming stronger hydrogen bonds with each other. However, the branched PNIPAM copolymers also had a lower CP than linear PNIPAM copolymers at the same monomer ratio. This suggests that the linear copolymers yielded more stable micelles than did the branched ones.

The LCST of triblock copolymers[8f] (ABC type) and their aggregation behavior have been studied[2b]. One of the thermoresponsive blocks was hydrophilic and non-ionic ((Ethylene glycol) methyl methacrylate, EGMA), the second block (*N,N*-Dimethylaminoethyl Methacrylate, DMAEMA) was both hydrophilic and ionizable, and the third block (*n*-butyl methacrylate, BuMA) was hydrophobic and non-thermoresponsive. The researchers found that by altering the position of the hydrophobic block, but maintaining the overall composition, the CP ranged from 54 ˚C to 72 ˚C. They attributed the effect to the position of the hydrophobic block altering the micelle structure. Another study of triblock copolymers with one hydrophilic block and two thermoresponsive blocks[2b] reported that changes in micellar shape and size were controlled by temperature.

Polymers from di(ethylene glycol) methyl ether methacrylate (DEGMA *Mn* = 188 g/mol) and oligo(ethylene glycol) methyl ether acrylate (OEGA *Mn* = 480 g/mol) are a newer class of thermoresponsive materials, with excellent potential as smart biocompatible materials[2b, 7a, 7b]. These EG-based monomers can be polymerized to give polymers with well-defined structure, composition, and tunable LCST using controlled radical polymerization methods. They can also produce thermoresponsive nanoparticles (NPs) with EG moieties already at the aqueous interface. That allows them to be used as drug delivery vehicles and administered into the bloodstream without additional surface modification to resist non-specific protein absorption, extending survival time in the blood. A diblock copolymer using these monomers was thought to have value for "surfactant on demand" applications[2b] since the CP of these blocks can be tuned over a broad temperature range compared with PNIPAM[12].

Overall the evidence of end group effects on CP is still somewhat conflicting, largely because the studies involve different polymers and copolymers, molecular weights, architectures, etc. However, the overall weight of the evidence suggests that micelles form below the CP and that hydrophobic chain ends promote this formation, while hydrophilic chain ends effect the hydration and organization of the (co)polymer below the CP.[2b] Nevertheless, additional research is needed, especially in the area of amphiphilic diblock copolymers, where there is little prior research.

We previously[12] studied the effect of diblock sequence on the CPs of linear diblock copolymers of DEGMA and OEGA with amphiphilic chain ends (dithioester and carboxylic acid). The CP of a series of copolymers, with the same block sequence, rose linearly as the hydrophilic block length rose, as expected. Less expected though was that the difference in CP of diblock copolymers with similar composition but different block sequence could be as little as 1.0 ˚C or as much as 28.0 ˚C. While molecular weight was previously shown to not significantly affect the CP[13] designing amphiphilic block copolymers with amphiphilic end groups has a significant impact on the CP. This likely arises from the effects on chain conformation and how the different chain end groups interact with the different polymer domains.

Here we continue our study of asymmetric end group effects on the CP of DEGMA and OEGA block copolymers to include additional end groups, and architecture. Our overall objective is to better understand these effects on amphiphilic block copolymers from EG-containing monomers, because their CPs can be tuned over a broad range and their

biocompatibility and resistance to protein absorption make them increasingly important copolymers for drug delivery vehicles.

Figure 3.1 shows the structure of and abbreviations used for the six CTAs that are studied in this paper. Illustrations of the block structures and abbreviations for the diblock copolymers in this work are given in Figure 3.2.

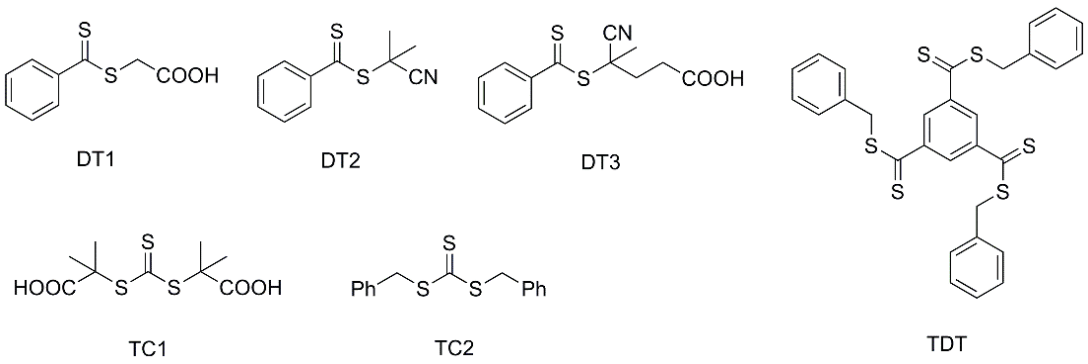


Figure 3.1: CTAs to be studied

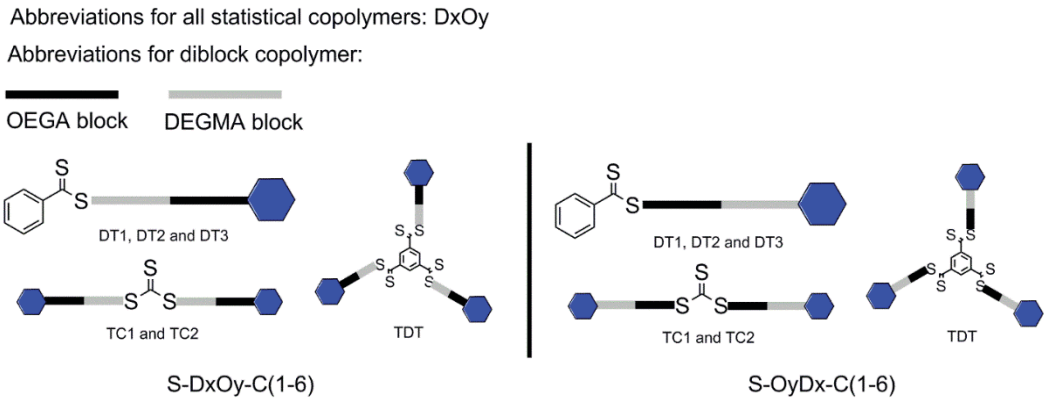


Figure 3.2. This graphical illustration (blue hexagons represent the "C" end) is used to give a simplified image of polymer structure, and show their abbreviated designations. "S" as a chain end refers to a dithioester or trithiocarbonate group from the CTA, while "C" refers to the other chain end resulting from an asymmetric CTA.

## 3.2 Experimental

### 3.2.1 Materials

Di (ethylene glycol) methyl ether methacrylate (DEGMA *Mn*=188.2 g/mol) and oligo (ethylene glycol) methyl ether acrylate (OEGA *Mn*=480g/mol) were purified by passing over a neutral aluminum oxide column to remove residual inhibitor. 2, 2'-Azoisobutyronitrile (AIBN) was recrystallized from ethanol. The following reagents were used as received: carbon disulfide, chloroform, acetone, sodium hydroxide, ligroin, hydrochloric acid, benzene tricarboxylic acid, benzyl mercaptan, phosphorus pentasulfide, 1,4-dioxane, tetrabutylammonium hydrogen sulfate, hexane, S-(Thiobenzoyl)thioglycolic acid (DT1) 2-cyano-2-propyl benzodithioate (DT2), and 4-cyano-4-(phenylcarbonothioylthio) pentanoic acid (DT3). The remaining CTAs were synthesized using procedures given below.

### 3.2.2 CTA synthesis

**Synthesis of S, S'-bis(α,α′-dimethylacetic acid) trithiocarbonate (BDAT / TC1)**

TC1 was synthesized according to a published method (Scheme 3.1).[14] Carbon disulfide (2.74 g, 0.036 mol), chloroform (10.75 g, 0.09 mol), acetone (5.23 g, 0.09 mol) and tetrabutylammonium hydrogen sulfate (0.241 g, 0.071 mol) were mixed with 12 mL of ligroin in a 250 mL round bottom. Then NaOH solution (50%, 20.16 g) was added dropwise into the mixture over 1.5 h while maintaining the temperature below 25 $^{o}$C. After the addition was complete the reaction was maintained at 22-25$^{o}$C for 12 h while being stirred with a magnetic stirrer. Once the reaction was completed, 90 mL $H_2O$ was added to dissolve the yellow solids, followed by adding 12 mL of $HCl_{conc}$ to acidify the

aqueous solution and yield crystalline solids. After filtration and washing several times by $H_2O$, the crude compound (3.26 g, 32.11%) was purified by recrystallization in toluene and acetone (3:1 v/v). $^1$H NMR ($CDCl_3$): 1.68 (s, -C**H**$_3$, 12H), Figure A1.

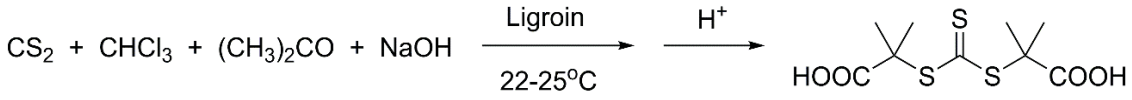


Scheme 3.1: TC1 synthesis

**Synthesis of dibenzyl trithiocarbonate (TC2)**

TC2 was synthesized following the method given in a published paper[15] (Scheme 3.2): Carbon disulfide (800 mg, 10.5 mmol) and benzyl chloride (1.27 g, 10.0 mmol) were added into 10 mL DMF. The reactor was placed in an ice bath and then potassium carbonate (1.38 g, 10.0 mmol) was added into the DMF solution. The reaction mixture was stirred and maintained at 40°C for 24h before being quenched by pouring into ice-water. The mixture was extracted by ethyl acetate and dried with anhydrous sodium sulfate. After filtering and removing the solvent, a yellow oil product was obtained (2.60 g, 89.66%). $^1$H NMR ($CDCl_3$): 4.60 (s, Ar-C$\underline{H}_2$- 4H), 7.21-7.35 (m, Ar-$\underline{H}$, 10H), Figure A2.

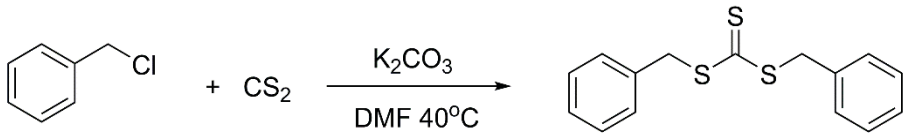


Scheme 3.2: TC2 synthesis

**Synthesis of 1,3,5-Benzenetricarbodithioic acid (TDT)**

TDT was prepared using a known procedure[16] (Scheme 3.3): Benzene tricarboxylic acid (2.00 g, 0.0095 mol), benzyl mercaptan (3.50 g, 0.029 mol), $P_4S_{10}$ (3.18 g, 0.0072 mol), and dioxane (150 mL) were introduced into a three-neck flask. The mixture was heated and maintained at reflux (100 $^oC$) for 24 h. The solution was concentrated down to about 20% of the original volume, and the solid waste product was removed by filtration. Then $CH_2Cl_2$ was added to the filtrate, and the mixture was filtered a second time. The solution was then passed through a short silica gel column using hexane : $CH_2Cl_2$ (5 : 1) as eluent. The crude compound was then purified through a second column of silica gel using hexane : EtOAc ( 9 : 0.5) as eluent (yield = 12.1%). $^1H$ NMR ($CDCl_3$): 4.58 (s, -S-C$\underline{H}_2$-, 6H), 7.23-7.58 (m, $CH_2$-Ar$\underline{H}$, 15H), 8.68 (s, Ar$\underline{H}$, 3H), Figure A3.

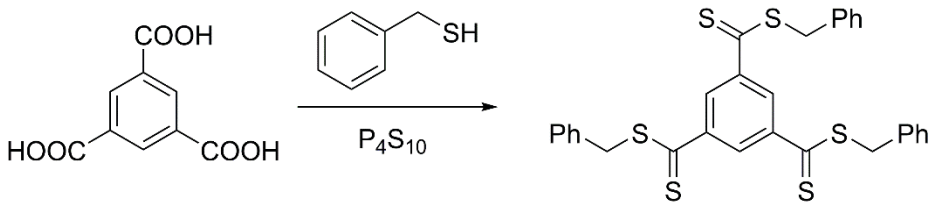


Scheme 3.3: TDT synthesis

## 3.2.3 Synthesis of statistical P(DEGMA-co-OEGA) ($D_xO_y$) copolymer

A typical RAFT synthesis procedure is illustrated in Scheme 3.4. An example procedure, using DT3 as CTA, is as follows: DEGMA (1.88 g, 0.01 mol), OEGA (4.80 g, 0.01 mol), DT3 (0.056 g, $2\times10^{-4}$ mol) and AIBN (0.0033 g, $2\times10^{-5}$ mol) were dissolved in 1,4-dioxane (30 mL) and the mixture was degassed with $N_2$ for 30 min. The RAFT polymerization was performed at 85 $^oC$ with continuous stirring while under the protection of $N_2$ gas. After 48 h, the mixture was concentrated using a rotary evaporator

and precipitated 3 times in cold hexane (0 $^{o}$C, ice bath). The product was dried in vacuo at 80 $^{o}$C for 3 h to obtain a viscous copolymer (5.84 g) with a yield of 86.6 %.

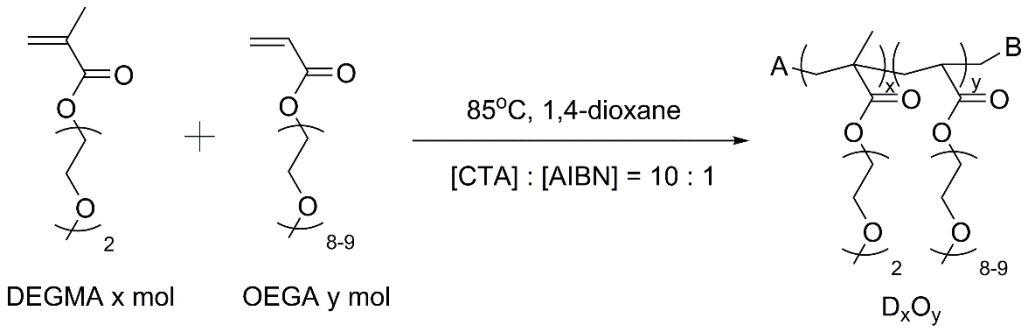


Scheme 3.4: Statistical copolymer synthesis

### 3.2.4 Synthesis of diblock P(DEGMA-*b*-OEGA) copolymers (S-$D_xO_y$-C(1-6) and S-$O_yD_x$-C(1-6)) by two step RAFT polymerization

All the diblock copolymers were synthesized in a similar way, exemplified here by the synthesis of S-$D_{50}O_{50}$-C with DT3 (Scheme 3.5). OEGA (4.8 g, 0.01 mol), DT3 (0.056 g, $2\times10^{-4}$ mol), AIBN (0.0016 g, $1\times10^{-5}$ mol) and 1, 4-dioxane (30 mL) were mixed and degassed for 30 min. The mixture was heated at 85 $^{o}$C under the protection of $N_2$ (g) for 48 h. The resulting macro-CTA (S-$O_{50}$-C) was isolated by concentration using a rotary evaporator. The crude product was precipitated 3 times in cold hexane (0$^{o}$C, ice bath). After drying at 80 $^{o}$C for 3 h in vacuo, the purified macro-CTA was obtained (4.40 g, 90.6%).

In the second step, the macro-CTA (S-$O_{50}$-C), DEGMA (1.88 g, 0.01 mol), AIBN (0.0016 g, $1\times10^{-5}$ mol) and 1,4-dioxane (30 mL) were mixed and degassed for 30 min, and then heated and stirred for 48 h at 85 $^{o}$C under $N_2$ gas protection. The reaction mixture was concentrated and precipitated in cold hexane (0$^{o}$C, ice bath) and dried in

vacuo at 80 $^{o}$C for 3 h. The overall yield of S-$D_{50}O_{50}$-C is 82.1% (5.53 g). They were then dialyzed for 3 days using dialysis tubes with a 3500 cut off.

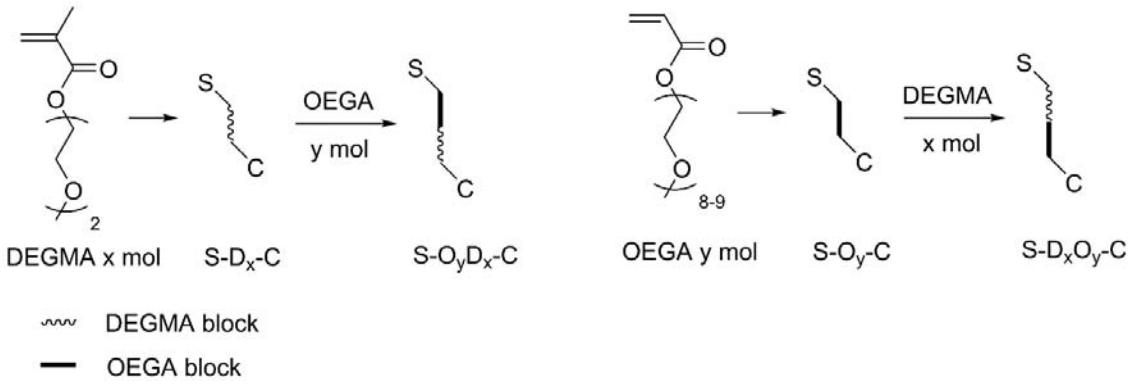


Scheme 3.5: Diblock copolymer synthesis

## 3.3 Characterization

$^{1}$H NMR spectra were recorded in $CDCl_3$ on a Varian Unity Inova400 at 400 MHz. Fo is the ratio of OEGA in the diblock copolymer which was calculated using the integration values from $^{1}$H NMR spectra. The full details of the calculation and methods are given elsewhere[12]. The NMR spectrum in Figure 3.3 identifies key hydrogen bands, whose populations were calculated by Equation 3.1 for Fo:

$$\frac{3 \times (1 - Fo) + 3 \times Fo}{6 \times (1 - Fo) + 32 \times Fo} = \frac{integration\ of\ Hd}{integrations\ of\ (Hf + Hg + Hh + Hi)}$$

Equation 3.1 Fo calculation

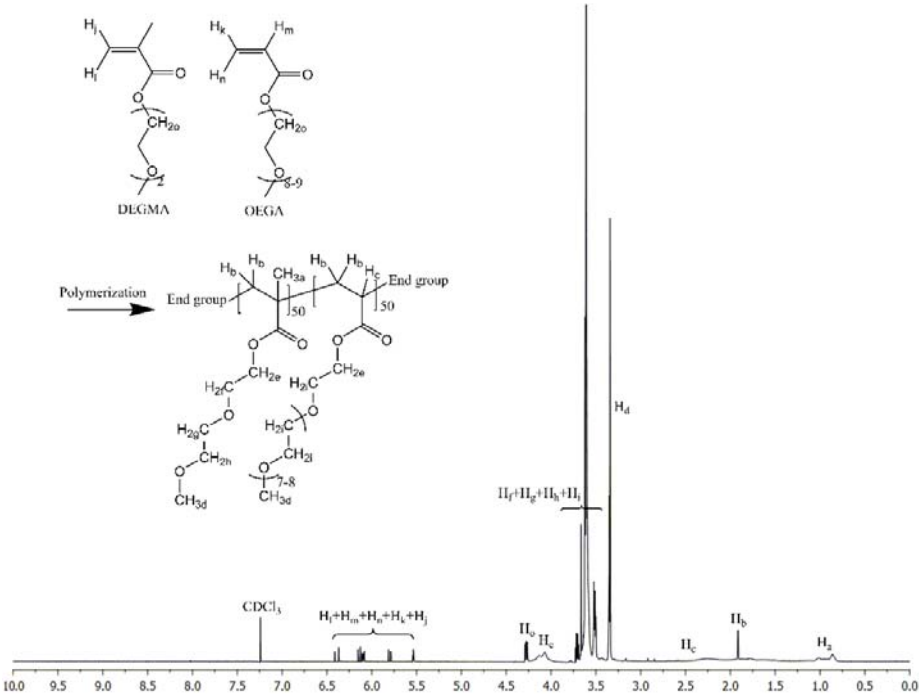


Figure 3.3 The label for each hydrogen on NMR spectra

UV-vis spectra were recorded using a Perkin Elmer UV/vis spectrometer (Lambda 35) equipped with a Peltier based temperature controller. All the CPs of the aqueous copolymer solutions were determined at a wavelength of λ=500nm. The aqueous solutions were loaded into quartz cuvettes at a concentration around 5-10 mg/ml. The transmittance (T %) was recorded at each 1 ˚C interval, using a heating/cooling rate of 1 $^{o}$C/min. When the temperature approached the CP (ΔT% > 2%), the heating/cooling rate was lowered to 0.1 $^{o}$C/min. At each temperature where T% was to be measured the solution was maintained for 2 min at that temperature before the T% was recorded to ensure the transmittance was stable. The test was concluded when the T% decreased to a minimum of 2% of the maximum T%. Then, all the transmittance values were normalized onto a 0-100% scale. The CP curves were then plotted with normalized transmittance values versus temperature. The temperature value of the normalized

T%=50% was defined as the CP. The transition range (ΔT) of the copolymer was defined as the change of the temperature values from T%=90% to T%=10%.

A dynamic light scattering (DLS) instrument (Coulter NP4 plus, Beckman Coulter, Fullerton, CA) was used to test the hydrodynamic diameter ($D_h$) of the copolymer in aqueous solutions.

Molecular weights were determined by gel permeation chromatography (GPC, Viscoteck GPCmax VE2001, Malvern Instruments Ltd, UK), equipped with Viscotek 270 dual detector and VE 3580 RI detector. One SDV GPC Analytical column of 1000 Angstrom, 5 Micron and dimension of 8 x 300 mm (Polymer Standard Service-USA Inc.) and THF were used as stationary and mobile phases respectively. 1.0 mg/mL of each polymer sample in THF solution was prepared and filtered through 0.2 μm syringe filter before injection with 100 μL for test. Poly(ethylene glycol) (Polymer Standard Service-USA Inc.) was used as standards for molecular weight calibration with a concentration of 1.0 mg/mL. The calibration data are in Table A1 and Figure A4, and a representative spectrum is given in Figure A5.

## 3.4 Results and Discussion

The statistical (control) and block copolymers of OEGA and DEGMA were prepared using three different categories of CTAs, with the theoretical ratio of OEGA to DEGMA at 50:50. After the composition was confirmed to be similar to the theoretical composition the effects of end group and architecture were studied on nanoparticle size, CP, and the temperature range of the coil-globule transition. The copolymer composition,

$D_h$, CP and ΔT are all given in Table 3.1. The theoretical number-average molecular weight is defined as Equation 3.2:

$$Mn(th) = \frac{[DEGMA]o \times M(DEGMA) + [OEGA]o \times M(OEGA)}{[CTA]o} + M(CTA)$$

Equation 3.2 The theoretical number-average molecular weight calculation

In Equation 3.2, [DEGMA]o, [OEGA]o and [CTA]o are the initial concentrations of the monomers and CTA, while M(DEGMA), M(OEGA) and M(CTA) are their molecular weight. The molecular weight of S-$D_{50}O_{50}$-C1 and S-$O_{50}D_{50}$-C1 were measured by Matrix-assisted laser desorption/ionization – time of flight (MALDI-TOF). All the specimens were tested by GPC and showed a molecular weight similar to theoretical but often a broad PDI attributed to a high molecular weight fraction not separated by the dialysis tube. Most of the PDIs were between 2.46-3.72 but two were above 4 and two were above 5 (Table S2). However, several other researchers have indicated the CPs of these polymers are not significantly altered by molecular weight differences[9, 13, 17]. That seems to be the case here also, as the specimens with the broadest PDI (the star polymers at 5.69 and 5.86, and S-$D_{50}O_{50}$-C3 at 4.71) had CPs that occurred over a narrow temperature range (Table 3.1). For example the star polymers collapsed over a 2.0 and 1.2 ˚C range. Also, S-$D_{50}O_{50}$-C3 with its 4.71 PDI collapsed over a 3.5 ˚C range while S-$O_{50}D_{50}$-C3 had a PDI of 2.47 and collapsed over a 7.5 ˚C range.

### 3.4.1 Measured copolymer composition

The copolymer composition was measured using $^1$H NMR, and is reported as Fo. The Fo of the statistical copolymer is close to the theoretical 50% (47%-55%) for all the

Table 3.1 Copolymer composition, $D_h$, CP and ΔT

| CTA | Sample | $Y_D$ (%)[a] | $Y_O$ (%)[b] | $Y_{over}$ (%) | $F_o$ (%)[c] | $D_h$ (nm) | Mn (th)[d] | Mw (GPC)[e] | CP (°C) | ΔT (°C) |
|---|---|---|---|---|---|---|---|---|---|---|
| Dithioester CTAs | | | | | | | | | | |
| 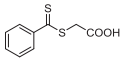 DT1 | $D_{50}O_{50}$ | - | - | 70 | 55 | - | - | - | 66.3 | 5.0 |
| | S-$D_{50}O_{50}$-C1 | 38 | 89 | 75 | 49 | 152 | 33,612[f] | 44,000 | 48.9 | 1.6 |
| | S-$O_{50}D_{50}$-C1 | 69 | 85 | 80 | 68 | 254 | 33,612[g] | 27,900 | 27.6 | 4.0 |
| 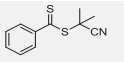 DT2 | $D_{50}O_{50}$ | - | - | 91 | 55 | - | - | - | 71.0 | 2.5 |
| | S-$D_{50}O_{50}$-C2 | 43 | 92 | 78 | 46 | 134 | 33,621 | 38,800 | 54.7 | 1.5 |
| | S-$O_{50}D_{50}$-C2 | 39 | 85 | 72 | 75 | 252 | 33,621 | 29,200 | 35.3 | 10 |
| 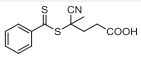 DT3 | $D_{50}O_{50}$ | - | - | 87 | 54 | - | - | - | 69.4 | 2.5 |
| | S-$D_{50}O_{50}$-C3 | 60 | 91 | 82 | 50 | 143 | 33,679 | 30,900 | 54.2 | 3.5 |
| | S-$O_{50}D_{50}$-C3 | 40 | 96 | 80 | 72 | 305 | 33,679 | 21,300 | 30.2 | 7.5 |
| Trithiocarbonate CTAs | | | | | | | | | | |
| 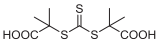 TC1 | $D_{50}O_{50}$ | - | - | 94 | 54 | - | - | - | 74.7 | 2.5 |
| | C-$O_{25}D_{50}O_{25}$-C | 61 | 90 | 82 | 53 | 103 | 33,682 | 37,800 | 29.2 | 2.5 |
| | C-$D_{25}O_{50}D_{25}$-C | 73 | 83 | 80 | 60 | 266 | 33,682 | 22,700 | 31.8 | 5.7 |
| 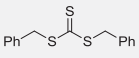 TC2 | $D_{50}O_{50}$ | - | - | 90 | 47 | - | - | - | 67.5 | 3.0 |
| | Ph-$O_{25}D_{50}O_{25}$-Ph | 59 | 92 | 83 | 42 | 184 | 33,690 | 30,800 | 40.5 | 4.5 |
| | Ph-$D_{25}O_{50}D_{25}$-Ph | 84 | 89 | 88 | 60 | 115 | 33,690 | 33,800 | 25.2 | 2.0 |
| Star CTA | | | | | | | | | | |
|  TDT | $(D_{50}O_{50})_3$ | - | - | 79 | 50 | - | - | - | 66.1 | 1.2 |
| | S-$(D_{50}O_{50})_3$-C6 | 55 | 89 | 80 | 57 | 95 | 100,734 | 77,100 | 57.5 | 2.0 |
| | S-$(O_{50}D_{50})_3$-C6 | 43 | 88 | 75 | 63 | 130 | 100,734 | 81,400 | 24.6 | 1.2 |

[a] Percent yield for the polymerization of the monomer DEGMA. [b] Percent yield for the polymerization of the monomer OEGA. [c] The ratio of OEGA in the diblock copolymer, calculated from Equation 3.1. [d] Theoretical number-average molecular weight, calculated from Equation 3.2. [e] Molecular weight tested by GPC. PDI are given in Table S2. For linear polymers these ranged from 2.46-4.71, but for stars were 5.69-5.86. [f] Molecular weight tested by MALDI-TOF: Mw = 38,555 PDI = 1.12. [g] Molecular

copolymers regardless of the CTA used. Therefore, these CTAs did not significantly affect the reaction of the two monomers. However, the order of monomer addition used to synthesize the diblocks does effect the composition of the diblock copolymers.

Specifically, the Fo in S-Dx**Oy**-C (O block formed first), ranged from 46% to 57% which is similar to the range found for the statistical copolymers, but when we reversed the order of monomer addition, to produce S-Oy**Dx**-C and the D block first, Fo was even higher, ranging from 60% to 72%. The effect on overall copolymer composition arises because of the effect of the pendent EG chain (oligoethylene oxide with 8-9 pendent EG groups versus diethylene glycol with only 2 pendant EG groups) on the solvation and mobility of the growing chain end. That is, by reacting the OEGA first, the longer EG side chain of the OEGA allows the polymer to retain greater solvation and mobility, which increases the yield of OEGA. The compositional differences shown in Table 3.1 show that OEGA consistently yields higher reaction efficiency than DEGMA. Conversely, when the DEGMA is reacted first, the resulting polymer is less soluble and this slows the reaction with respect to DEGMA. We propose this as the major reason for the differences in composition, although it cannot be ignored that some reactivity difference in the monomers can be attributed to the methyl group on the radical-bearing carbon of DEGMA lowering the reactivity compared to OEGA. This is because the methyl groups add electron density to the propagating radical chain end and perhaps some additional steric hindrance, but those effects are inherent to the monomer and independent of block sequence.

### 3.4.2 CP of Statistical copolymers

Earlier studies have reported the effects of composition and end groups on the CP of OEGA/DEGA acrylates and OEGMA/DEGMA methacrylate copolymers.[2b, 7b, 7c, 18] In our prior work we looked at OEGA/DEGMA diblock copolymers, where we used OEGA instead of OEGMA to enhance the hydrophobicity difference of the two monomers.[12]

The relationship between the copolymer composition and CP of the statistical from these two monomers followed a similar relationship of Fo/CP described by our prior work, CP = 0.907Fo + 20.4 (using only DT1), and first shown by Lutz et *al*.[7a]. From the linear relationship generated from the statistical copolymers in that work[12], the CP for a theoretical Fo=50) should around 65.7 $^{o}$C. The CTAs used here gave slightly different polar end groups, and different architectures, and yet the measured CPs of the statistical copolymers generated here ($D_{50}O_{50}$) were similar, regardless of end group or architecture, ranging from 66.3-74.7 ˚C. And, the measured CP is very close to the value predicted by the linear relationship, using the actual composition again regardless of the end group or the architecture: DT1/66.3$^{o}$C, DT2/71.0$^{o}$C, DT3/69.7$^{o}$C, TC1/74.7$^{o}$C, TC2/67.5$^{o}$C and TDT/66.1$^{o}$C.

Therefore, although end group identity and placement significantly affect the CP of diblock copolymers, as shown in the following section, end group effects on statistical copolymers are generally small. However, if the reactivity ratios of the monomers are significantly different so they tend towards a blocky copolymer structure an end group effect should still be anticipated.

### 3.4.3 Effect of end group on diblock copolymer properties

The six DEGMA/OEGA (1:1) diblock copolymers prepared from DT1-3 gave an actual Fo ranging from 0.47 to 0.55. The copolymers possessed the same hydrophobic end group ($PhCS_2$) but slightly different hydrophilic chain ends. The effect of the changes in end group structure on the CPs was measurable but small, regardless of the hydrophilic chain end. The largest difference was 7.7 ˚C (S-$O_{50}D_{50}$-C2 compared to S-$O_{50}D_{50}$-C1).

The difference polarity was insignificant in comparison to the effects from chain end placement.

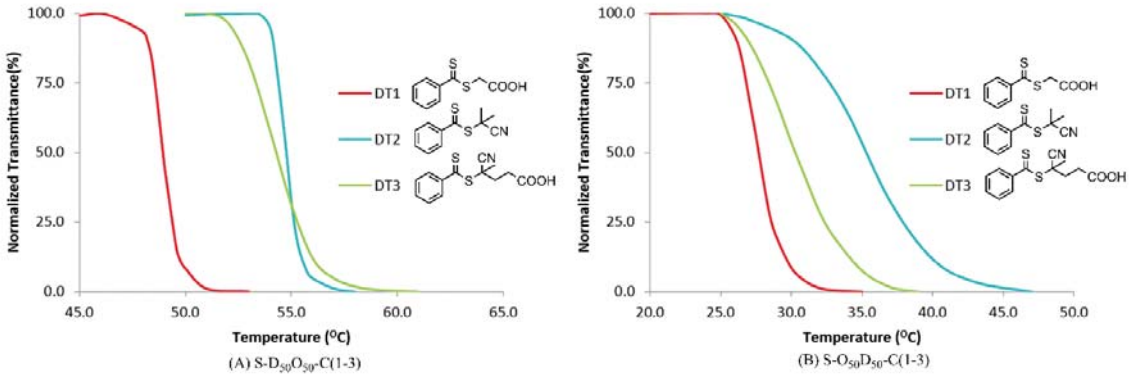


Figure 3.4: CP curves of diblock copolymers from DT1-3. A: S-DxOy-C(1-3) B: S-OyDx-C(1-3)

Pairing the hydrophobic $PhCS_2$– chain end with the hydrophobic (compared to OEGA) DEGMA block drops the CP by 15-17 ˚C relative to the CP of the statistical copolymers (Table 3.1) prepared using the same CTAs. However, pairing the hydrophobic $PhCS_2$– chain end with the hydrophilic OEGA block drops the CP by 36-39 ˚C. Furthermore, the CP curves show a relatively narrow transition (ΔT) for the coil collapse when the hydrophobic chain end is paired to the hydrophobic DEGMA block (Figure 3.4A), but pairing the hydrophobic chain end to the hydrophilic OEGA block results in the coil collapse occurring over a much broader temperature range (Figure 3.4B). The relative effect of chain end placement on CP is more clearly seen in a bar chart format (Figure 3.5a).

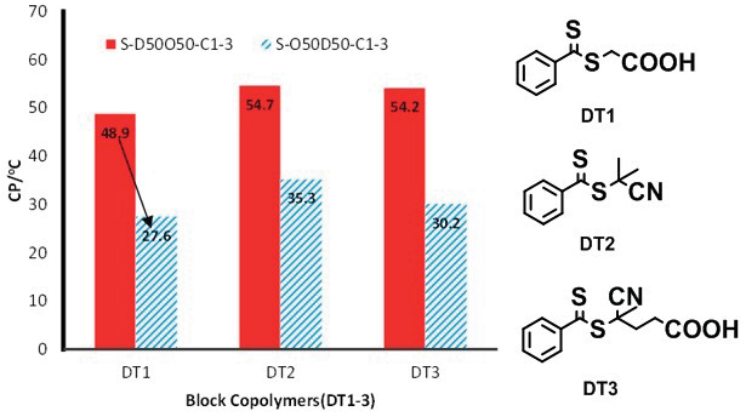


(a) CP of block copolymer (DT1-3)

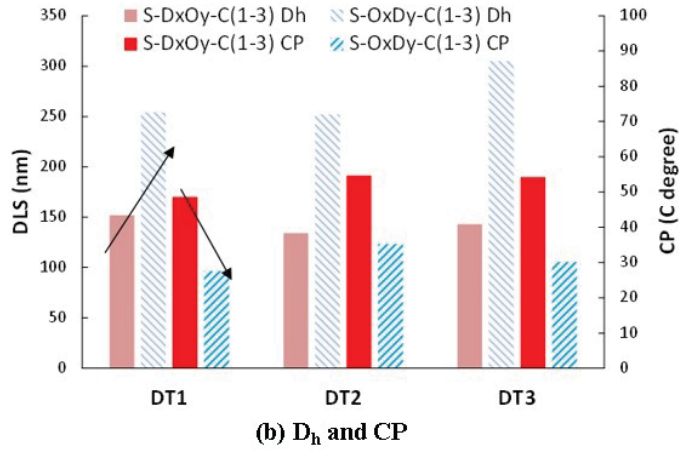


(b) $D_h$ and CP

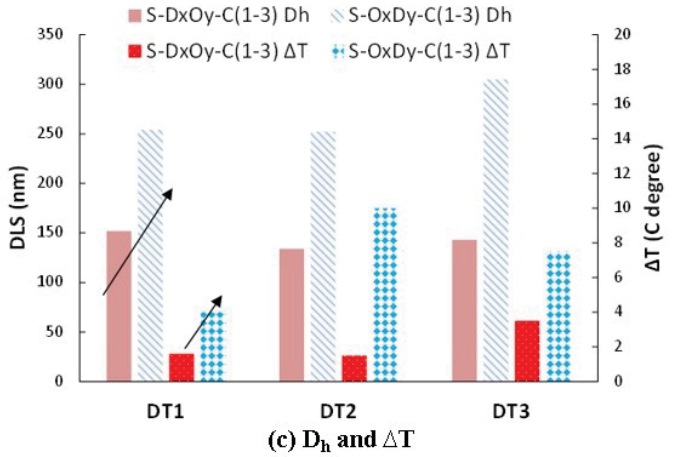


(c) $D_h$ and ΔT

Figure 3.5 (a) bar chart comparing CPs based on end group and block sequence, (b) $D_h$ and CP, and (c) $D_h$ and ΔT.

The relationship between the CP of linear OEGA/DEGMA diblock copolymers and amphiphilic end groups is clear: matching the polarity of block with end groups (i.e. pairing the hydrophilic OEGA block with the hydrophilic end group and the more hydrophobic DEGMA block with the hydrophobic end group) gives a higher CP and a more narrow transition than blocks paired to end groups of a different polarity.

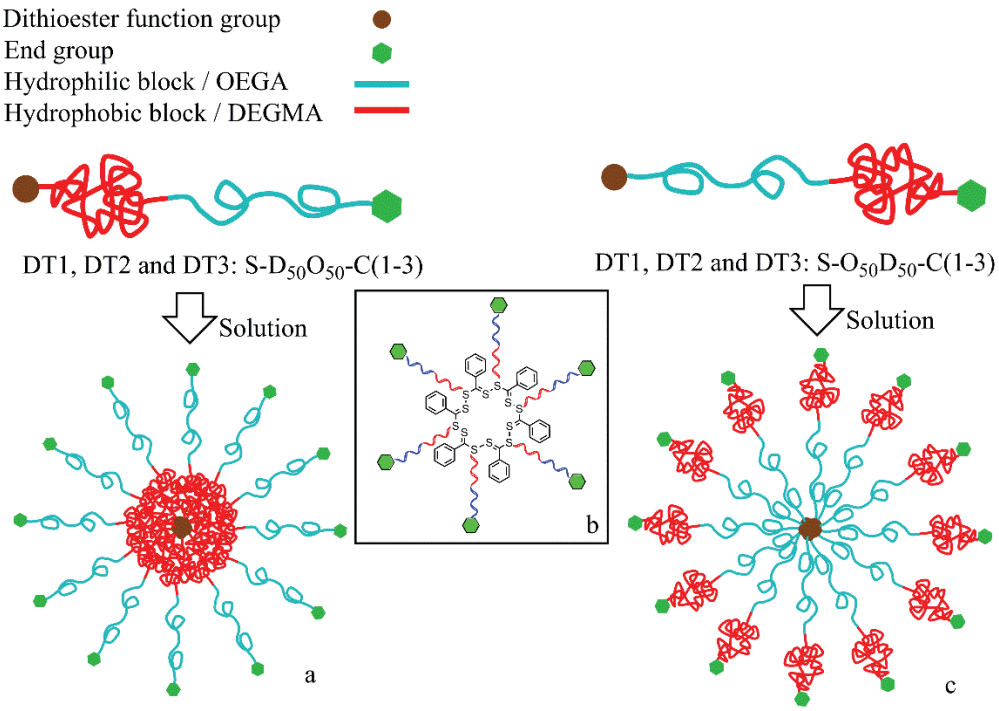


Figure 3.6 Affect of temperature on conformations of (a) S-DxOy-C, where chain end and block polarity are matched; (b) possible interactions between dithioester chain ends in the micellar core; and (c) S-OyDx-C, where chain end and block polarity are mismatched.

Figure 3.5a-c illustrates the significant differences in CP and $D_h$ that result from that pairing the hydrophobicc end to the hydrophobic DEGMA block giving S-DxOy-C (DT1-3) compared to when the pairing is reversed. The “mixed pairing“ of the

hydrophobic chain end to the hydrophilic block (S-OyDx-CDT1-3) gives a significantly lower CP because it results in a less orderly and efficient hydration sphere, so less energy is required to collapse the coil (Figure 3.6a).

This same effect causes a clear correlation between end group pairing and the $D_h$ (Figure 3.5b). For example, for the three diblock copolymers where the hydrophobic chain end is paired to the hydrophobic DEGMA (S-DxOy-C) block the only CP detected is near ~55 ˚C and the $D_h$ is ~ 150 nm. Conversely, for the three copolymers where the end group pairing is reversed, i.e. S-OyDx-C copolymers, the CP is near ~30 ˚C and the $D_h$ is ~ 250-300 nm. Compared to the effects of end group placement, the effect of identity of the hydrophilic end group on CP and $D_h$ was quite small. Figure 3.5c shows the correlation also exists between chain end pairing and $D_h$ and $\Delta T$ of the coil collapse. Pairing the hydrophobic chain end with the hydrophobic block results in a smaller $D_h$ and a significantly smaller $\Delta T$ compared to the mixed pairing of the hydrophilic chain end to the hydrophobic block.

It is clear that pairing the hydrophobic chain end with the hydrophobic block the impact on the CP, $D_h$ and $\Delta T$ are substantial. All of these effects arise from a small and well-ordered micellar structure, where the hydrophobic block is already collapsed, or nearly collapsed, and the hydrophilic block is well hydrated with the hydrophilic chain end facilitating that hydration. The chain end pairing may lead to structures something like that shown in Figure 3.6a for temperatures below the CP. A structure like this could also account for why a separate CP is not detected for the DEGMA block in the core, since it is either completely collapsed or nearly so, and the CP of pure PDEGMA with similar

chain ends is ~25 ˚C[12]. Therefore, since it is so poorly hydrated we did not detect any additional change. The orderly structure within the hydrophobic core may also be assisted by interactions between the dithioester groups, such as those suggested in Figure 3.6b.

Conversely when the chain end polarity and block polarity are mismatched, a structure more like that shown in Figure 3.6c may exist. This type of structure would be expected to have a lower CP and a greater $D_h$, compared to the structure shown in Figure 3.6a, because of a less hydrated OEGA coil within the micellar core, along with a less orderly collapse from the expulsion of water from the hydrated OEGA block. Because this coil is less ordered, the ΔT is broader than the values measured for the S-DxOy-C copolymers.

As stated above the exact identity of the polar chain end does have some impact on the CP and $D_h$ even for the same block sequence (but with difference CTAs), but this is far less than the effect from changing block sequence. For example, when the block sequence was the same the polar chain end identity resulted in no more than a 7.7 ˚C impact on CP (S-$O_{50}D_{50}$-C2 and S-$O_{50}D_{50}$-C1), and no more than a 53 nm impact on the $D_h$ (S-$O_{50}D_{50}$-C2 and S-$O_{50}D_{50}$-C3. But when comparing the same CTA but with the block sequence reversed we found the CP have the of as much as 24$^{o}$C (S-$D_{50}O_{50}$-C3 and S-$O_{50}D_{50}$-C3) and the $D_h$ difference increased to 163nm (S-$D_{50}O_{50}$-C3 and S-$O_{50}D_{50}$-C3).

**Trithiocarbonate CTAs (TC1 and TC2) and their symmetric copolymers**

Trithiocarbonate CTAs were used to produce symmetrical triblock ($O_{25}D_{50}O_{25}$ or $D_{25}O_{50}D_{25}$) copolymers. The trithiocarbonate CTAs, TC1 and TC2, also gave symmetric hydrophobic or hydrophilic chain ends respectively, where the hydrophilic chain ends are designated as “C”, and the hydrophobic chain ends are designated as “Ph”. The thermal

data shown in Figure 3.7 are also summarized in Table 3.2. Model structures for these copolymers are proposed in Figure 3.8.

Table 3.2 Effect of end groups on thermoresponse of symmetrical triblock copolymers

| Polymers | CTA | CP (°C) | $D_h$ (nm) | ΔT (°C) |
|---|---|---|---|---|
| C-$O_{25}D_{50}O_{25}$-C | TC1 | 29.2 | 103 | 2.5 |
| Ph-$O_{25}D_{50}O_{25}$-Ph | TC2 | 40.5 | 184 | 4.5 |
| C-$D_{25}O_{50}D_{25}$-C | TC1 | 31.8 | 266 | 5.7 |
| Ph-$D_{25}O_{50}D_{25}$-Ph | TC2 | 25.2 | 115 | 2.0 |

When the chain end and terminal block polarity are matched (i.e. hydrophobic end groups are paired with terminal hydrophobic blocks or hydrophilic chain ends are paired with terminal hydrophilic blocks) the CP, $D_h$, and ΔT are similar**.** Specifically, the CP's for C-$O_{25}D_{50}O_{25}$-C and Ph-$D_{25}O_{50}D_{25}$-Ph were 29.2 ad 25.2 ˚C, the $D_h$'s were 103 and 115 nm, and ΔT's were 2.5 and 2.0 ˚C. Therefore, these copolymers produced similar micelle size and hydration and an orderly coil collapse.

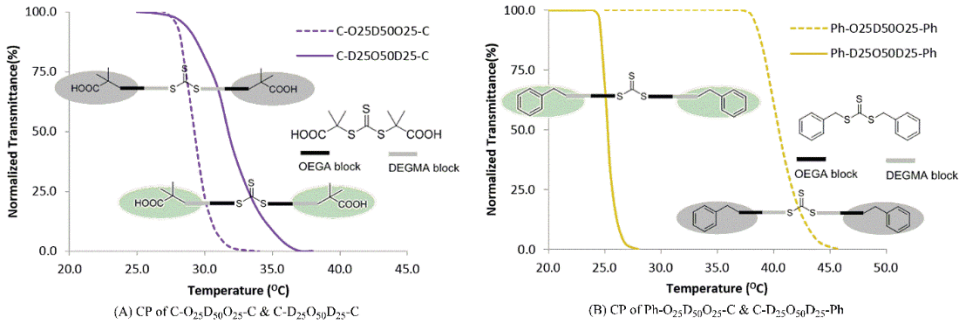


Figure 3.7. Graphs of transmittance v. temperature for symmetrical triblock copolymers that have both (a) hydrophilic and (b) hydrophobic, symmetric chain ends.

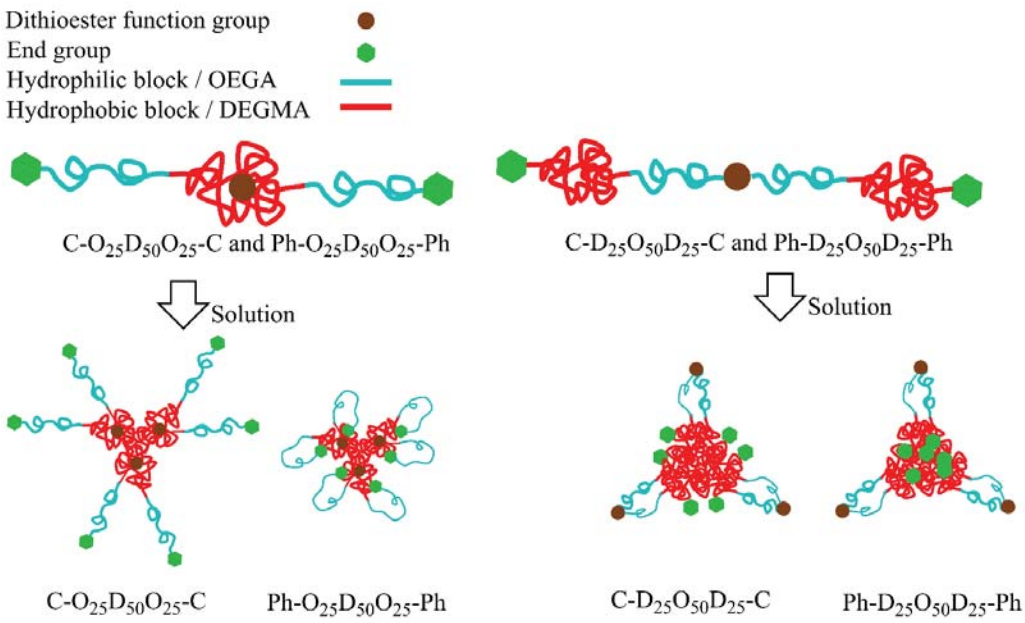


Figure 3.8: Proposed structures for symmetrical triblock copolymers from TC1 and TC2 in aqueous solution.

When the chain end and block polarity of the triblock copolymers are mismatched the CP, $D_h$, and $\Delta T$ are higher than those of the triblocks with matched chain end and block polarity. Also, the properties of the "mismatched polarity" triblock pair differ significantly from each other, while the properties of the "matched polarity" triblock pair were very similar to each other. For example, C-$D_{25}O_{50}D_{25}$-C has DEGMA blocks with hydrophilic chain ends, and has a CP a little higher than the two matched triblocks, 31.8 ˚C compared to 29.2 ˚C and 25.2 ˚C for C-$O_{25}D_{50}O_{25}$-C, and Ph-$D_{25}O_{50}D_{25}$-Ph respectively, but the CP of Ph-$O_{25}D_{50}O_{25}$-Ph, with OEGA blocks bonded to hydrophobic chain ends, is 40.5 ˚C. The two "mismatched polarity" triblock copolymers also have significantly larger $D_h$'s and broader $\Delta T$'s than the "matched polarity" triblock copolymers. The C-$D_{25}O_{50}D_{25}$-C has a $D_h$ of 266 nm and a $\Delta T$ of 5.7 ˚C, more than twice as large as those of the "matched polarity" triblock copolymers, and Ph-$O_{25}D_{50}O_{25}$-Ph has

$D_h$ of 184 nm and a ΔT of 4.5 ˚C. Possible structures arising from these mismatched polarity triblock copolymers in water are also given in Figure 3.8. The larger $D_h$ of 266 nm and ΔT of C-$D_{25}O_{50}D_{25}$-C suggests that the short DEGMA blocks are not effectively collapsed and the collapse above the CP is not efficient. But the results from Ph-$O_{25}D_{50}O_{25}$-Ph are difficult to explain. The CP of this triblock copolymer is almost 9 ˚C greater than that of the other triblock structures. However, it is also important to note that the composition of this triblock copolymer also differed more that the other copolymers from the theoretical value. The Ph-$O_{25}D_{50}O_{25}$-Ph copolymer had a Fo of only 42, while the Fo was 53-60 for the other triblock copolymers. Nevertheless these data do not seem consistent with the other findings.

**Star block copolymers (TDT)**

The CP curves of three-arm star copolymers with diblock arms having different block sequence are shown in Figure 3.9. Only hydrophobic chain ends were studied here because carboxylate groups were not successfully achieved on the terminal phenyl groups. The architecture of a star polymer was expected to facilitate a simple and orderly collapse of the arms at the CP, so it was not surprising that both copolymers had a narrow ΔT (2.0 and 1.2˚C). The block sequence gave a somewhat greater effect on the $D_h$ with S-$(O_{50}D_{50})_3$-C6 giving a larger micelle (130 nm) than S-$(D_{50}O_{50})_3$–C6 (95 nm) where the hydrophilic blocks formed the micelle's shell. When the hydrophobic DEGMA block is buried in the interior of the micelle it is more poorly hydrated than when it is the shell layer of the micelle, and so it is already collapsed or nearly collapsed, as illustrated in Figure 3.10. However, the OEGA block is well hydrated. Surprisingly though, the CPs of

the two star copolymers are quite different, with S-$(D_{50}O_{50})_3$–C6 having a CP that at 57.5 ˚C is nearly 33 ˚C higher than the star copolymer with the inverse block sequence, S-$(O_{50}D_{50})_3$-C6 which had a CP of 24.6$^{o}$C. It is thought that neither the OEGA nor the DEGMA blocks of the S-$(O_{50}D_{50})_3$-C6 copolymers are well hydrated.

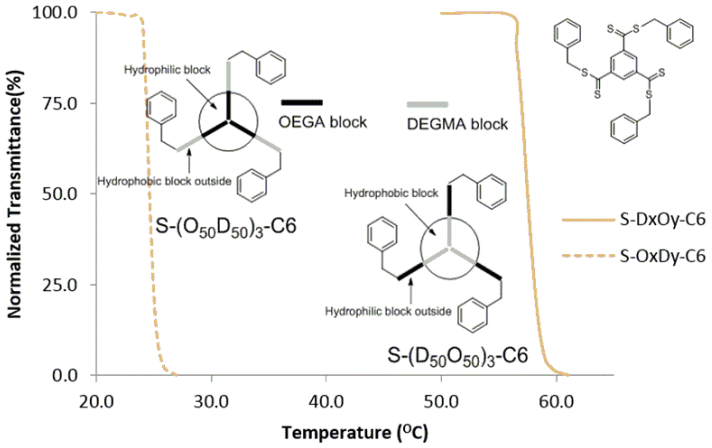


Figure 3.9: CP for Star copolymer

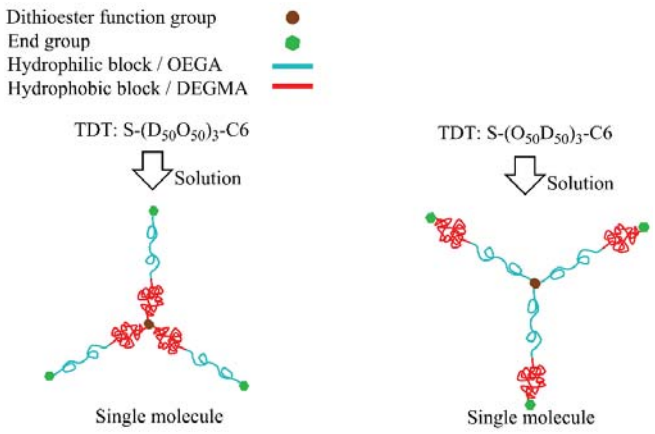


Figure 3.10: Star polymer structure in aqueous solution

## 3.5 Conclusions

Di- and triblock copolymers were easily prepared by RAFT polymerization using the hydrophilic OEGA and comparatively hydrophobic DEGMA with a series of different CTAs to study amphiphilic copolymers with different architectures and end groups. Linear diblock copolymers with amphiphilic end groups allowed the thermoresponse properties of diblock copolymers where the polarity of the blocks and chain ends was matched, to be compared to those of diblock copolymers with similar compositions but with block and chain end polarity being mismatched. Other CTAs allowed the synthesis of symmetrical triblock copolymers and allowed the effect of block sequence to be studied in conjunction with end groups that were matched or mismatched with respect to block polarity, and star diblock copolymers allowed the effect of block sequence with hydrophobic end groups to be studied in an architecture that will facilitate an orderly collapse of the chains.

When comparing the diblock copolymers the effect of pairing end groups to blocks with different hydrophobicity is clear. Pairing the hydrophilic block with the hydrophobic chain end yields micelles with a lower CP and a higher $D_h$ and $\Delta T$. The $D_h$ is almost twice as large as when the hydrophobicity of the block and chain end is better matched. When the blocks and chain ends are matched the hydrophilic block forms an efficient hydration sphere, giving the higher CP, while the hydrophobic block is effectively collapsed giving a smaller $D_h$ and $\Delta T$. However, mismatching disrupts the hydration giving a lower CP, and the hydrophobic block with hydrophilic chain end is also partially hydrated and perhaps aggregated leading to a larger $D_h$ and $\Delta T$. The star polymer shows a different trend because the architecture inhibits aggregation, so the difference in $D_h$ and

ΔT is less significant but placing the hydrophilic block on the outer shell clearly allows a more effective and orderly hydration sphere as proven by the much higher CP. The triblock copolymers showed slightly more complicated result. Matching chain ends to block hydrophobicity/philicity yielded the smallest $D_h$ and ΔT supporting the concept of the hydrophobic block being pre-collapsed and the small ΔT collapse of the hydrated hydrophilic block. However, when the chain ends were mis-matched to block polarity the results were contradictory. The larger $D_h$ and ΔT supported a less orderly micelle structure with a less orderly collapse, but the CPs were not consistent. The mismatched triblock with hydrophilic chain ends yielded a CP nearly identical to those of the triblock copolymers with matched chain ends and blocks, while the triblock with hydrophobic chain ends paired to hydrophilic blocks gave a much higher CP, suggesting an efficient and orderly hydration sphere.

Overall, the results are consistent with hydrophobic chain ends controlling micelle formation and hydrophilic blocks controlling hydration, and the data show that mismatching the hydrophilicity of the block to that of the chain end leads to disruption of the hydration sphere with a lowering of the CP and a broadening of the temperature range for the chain collapse. The architecture of a three-arm start reduced the extent of these effects, but was still consistent overall. The one exception to this was found for a symmetrical triblock copolymer with hydrophobic chain ends paired to hydrophilic blocks. The reason for this is not clear. Other analytical methods such as Small Angle Neutron Scattering will be needed to fully understand how pairing blocks with end groups of different hydrophobicity affect the hydration, aggregation and collapse of amphiphilic copolymers, but given the likely growing importance of these EG-containing

monomers and their thermo-response properties in the biomedical area, these materials are worthy of more study.

# Chapter 4 GNP-polymer drug delivery system

## 4.1 Introduction

Thermoresponsive polymers are a type of "smart" material that change phase in response to temperature.[1] These polymers may possess a lower critical solution temperature (LCST) or an upper critical solution temperature (UCST).[2] This research focuses on polymers with an LCST, and their value as drug delivery vehicles.[1a, 3]

The drug delivery field has advanced significantly in recent years, with much of the focus being in the area of targeted delivery, which seeks to maximize delivery of the drug at the target site and so maximize drug efficacy.[4] When the drug is potentially toxic, like a chemotherapy agent, an ideal drug delivery process would help to protect healthy tissues from damaging effects.[4c]

Three key factors to design an "ideal" drug delivery process are: delivery to the right area, delivery at the right time, and delivery in the right concentration. These are each discussed in the paragraphs below.

If a given drug is injected into the bloodstream there is no specific targeting, though there can be preferential adsorption into some tissues. However, drugs or drug carriers can be designed to carry targeting devices to give them the ability to target specific cell types or areas of treatment. For example, aptamers are single-stranded DNA or RNA molecules, and different aptamers are known to be specific to certain cell receptors.[5] Cell targeting is particularly desirable for highly toxic drugs, such as chemotherapy agents. Effectively targeting the cancer cell allows pharmaceutical efficacy while protecting healthy cells from the chemotherapeutic agent's toxicity. Using a targeting ligand that is specific to a

single type of cell is highly effective targeting.

Other methods are known that are less expensive but also less specific. For example, cell targeting may rely on differences in cell needs. Cancer cells reproduce more rapidly than normal cells and so they require more glucose than normal cells.[6] Because the cancer cells absorb so much glucose and it possesses many functional groups, glucose has been a convenient "vehicle" to transport other species into cancer cells. Glucose also is advantageous because sugar-macromolecule conjugates readily pass through cell wall barriers.[7]

Another reported example of cell targeting used magnetic nanoparticles.[8] The magnetic nanoparticles, already loaded with a drug(s), are injected to the blood stream, and an external magnetic field is applied near the target (illness) area. This draws the magnetic nanoparticles to the target site. This "passive" targeting does not rely on bonding the nanoparticles to a particular cell type, but if there is a well-defined tumor site it can be fairly selective.

The second desirable trait for the drug carrier is the ability to release the drug at a desired time. One way this is accomplished is by incorporating the drug in a "smart" stimulus-response drug carrier. Thermoresponsive polymers are a good choice for these drug carriers, because the polymer chains of the carrier collapse and expel water at the LCST, which also results in the expulsion of the drug. Other smart materials that have been investigated as smart drug carriers include those that expel the drug in response to a change in pH[9] or a magnetic field[10].

The third key trait for an ideal drug delivery system is the ability to release the drug at the proper concentration. This is perhaps the most challenging task in an ideal drug delivery

system, with many different variables. Of concern here is that the drug carrier should not release drug as it travels through the bloodstream and non-target tissues, but then must release the drug at the target site. Approaches to try to retain the drug in the carrier include designing systems that permit hydrophilic-hydrophobic interactions to for between carrier polymer and drugs[11], capsule techniques[12] and covalent bonding between carrier polymer and drugs[13]. The typical approach to releasing drug at a desired concentration is based on loading capacity (mass of the loaded drug / mass of the carrier × 100%)[14] of the carriers.[15] To date, the only method designed to release a specific quantity of drug into the blood stream at a specific time seems to be reservoir methods such as insulin pumps[16].

In this work we studied the drug delivery process of hybrid polymer systems prepared using thermoresponsive polymers and gold nanoparticles (GNPs). The thermoresponsive polymers are biologically safe amphiphilic diblock copolymers, with each block prepared from monomers that are known to give thermoresponsive polymers. The hydrophobic block is from diethylene glycol methacrylate monomer (DEGMA), and is intended to provide a suitable domain for hydrophobic drugs via hydrophobic-hydrophobic interactions. The hydrophilic block is from oligoethylene acrylate (OEGA) monomer, and is designed to stabilize the nanoparticle in the blood stream and extend its circulation time by preventing non-specific protein absorption as well as to possess a suitable chain end (here a carboxylic acid group from a RAFT chain transfer agent) that can be functionalized with a targeting device, such as an aptamer.

The GNPs are included in the formulation because they are able to absorb biologically safe wavelengths of light and convert them to heat, and as long as the GNP size is

appropriate they are generally considered safe to use in the human body[17]. The ability to convert light to heat is desirable for two reasons: it allows a secondary form of chemotherapy called hyperthermia[18], and is of particular interest here, because we can use this property to allow us to stimulate drug release from a thermoresponsive polymer with a "high" LCST (LCST >> 37 ˚C). The reason this is useful is that by using a nanoparticle with an LCST >> 37 ˚C we can reduce the amount of passive drug released in the bloodstream before the nanoparticles reach their target. If a sufficiently high LCST can be used to prevent all or most premature drug release in the blood, then damage to healthy cells and painful side effects from chemotherapy can be reduced, and once the nanoparticles are at the target site the appropriate light source can be used to heat the local tissues with the nanoparticles to above the LCST and trigger the drug release. This should increase drug efficacy and also allow the use of less drug.

To test this hypothesis we studied the drug releasing properties of two "high" LCST nanoparticles at four different temperatures: 20 ˚C, 37 ˚C (the temperature of the human body), 50 ˚C and 60 ˚C. The specific steps performed to test this hypothesis were: 1) synthesis of two diblock copolymers with cloud points (CP, used as an approximation of the LCST) that were higher than 37 ˚C; 2) the thioester end group of each polymer was converted to the desired thiol (-SH) end group, which can bond to the GNPs; 3) graft the diblock copolymer to GNP nanoparticles by a grafting-to route; and 4) load a model drug and measure the drug release profile of the GNP-polymer nanoparticles at different temperatures.

The overall hybrid design sequence is illustrated in Figure 4.1, however some minor changes were made to this design for this "proof-of-concept" work. Because the

absorption of light by gold to cause local heating is well established[19], we did not use light as the thermal trigger since it would not be possible with our facilities to measure or maintain a constant temperature. Also, because of the high cost of chemotherapeutic drugs, we used a less costly model drug, ibuprofen, to prove the concept of reduced drug release using thermoresponsive nanoparticles with a higher CP than typically studied, i.e. thermoresponsive nanoparticles with the CP near 37 ˚C are typically of interest[11, 20]. The most commonly used thermoresponsive polymers for biomedical applications have LCSTs in the range of 20-40 ˚C[1a, 21]. Also, much of this research used PNIPAM, with an LCST near 37 ˚C. We selected and prepared diblock copolymers with CPs around 50 ˚C and 60 ˚C. Finally, because of cost and the fact that cell work was not a part of this project we did not bond a targeting aptamer to the nanoparticles. While the aptamer might affect the CP of the final nanoparticles, again the hypothesis can be tested without the costly aptamer.

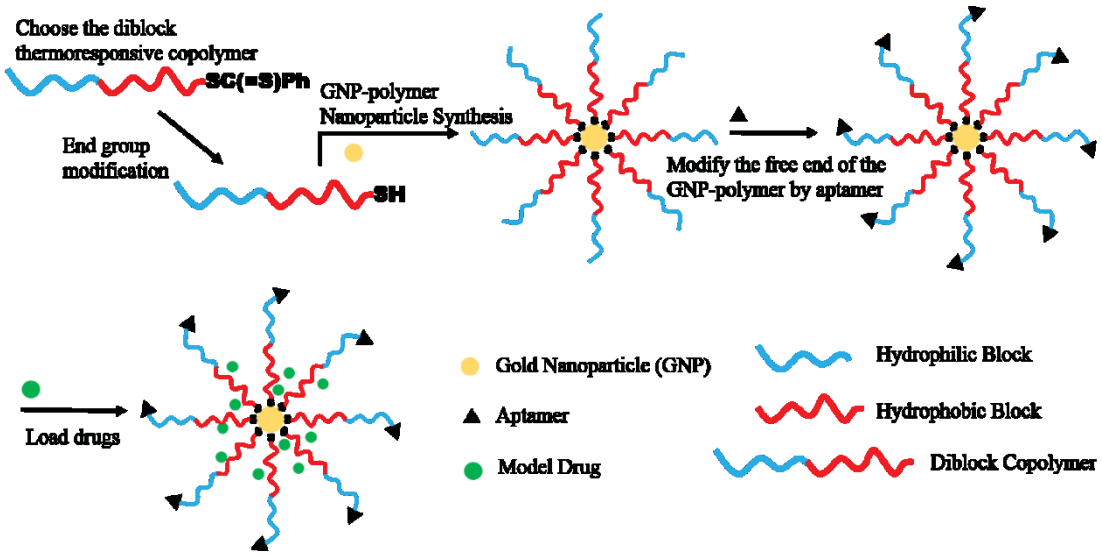


Figure 4.1: GNP-polymer synthesis and drug delivery property test

## 4.2 Experimental

### 4.2.1 Materials

The chain transfer reagent (CTA), S-(thiobenzoyl)thioglycolic acid, was used as received. The initiator, 2, 2'-azoisobutyronitrile (AIBN), was recrystallized from ethanol. Di (ethylene glycol) methyl ether methacrylate (DEGMA Mn=188.2 g/mol) and oligo (ethylene glycol) methyl ether acrylate (OEGA Mn=480g/mol), were purified by passing over a neutral aluminum oxide column to remove residual inhibitor. 1, 4-Dioxane, hexane, 1-hexylamine, dichloromethane (DCM), gold (III) chloride trihydrate ($HAuCl_4 \cdot 3H_2O$) and sodium citrate ($Na_3Ct$), were used as received.

### 4.2.2 Syntheses: S-$D_{50}O_{50}$-C and S-$D_{40}O_{60}$-C

The diblock copolymers, S-$D_{50}O_{50}$-C and S-$D_{40}O_{60}$-C, were prepared by the same method shown in Figure 4.2. For example, S-$D_{50}O_{50}$-C was synthesized using OEGA (4.8 g, 0.01 mol), CTA (0.0424 g, 0.2 mmol), AIBN (0.0016 g, 0.05 mmol) and 1, 4-dioxane (30 mL). These reagents were mixed and degassed under nitrogen for 30 min, and then heated at 85 ˚C under the continuing protection of nitrogen gas for 48 h. The resulting macro-CTA (S-$O_{50}$-C) solution was concentrated using a rotary evaporator to isolate the crude produce, which was then purified by re-dissolving in fresh dioxane and precipitating (3 times) in cold hexane (0 ˚C, ice bath). After drying at 80 ˚C for 3 h in vacuo, the purified macro-CTA was obtained (4.72 g, 97.4%).

In the second step, the macro-CTA (4.72 g), DEGMA (1.88 g, 0.01 mol), AIBN (0.0016 g, 0.05 mmol) and 1,4-dioxane (30 mL) were combined, degassed for 30 min, and then

heated and stirred for 48 h at 85 ˚C under continued nitrogen gas protection. The reaction mixture was concentrated and precipitated in cold hexane (0 ˚C, ice bath) and then dried in vacuo at 80 ˚C for 3 h. The overall yield of S-$D_{50}O_{50}$-C is 81.6% (5.49 g).

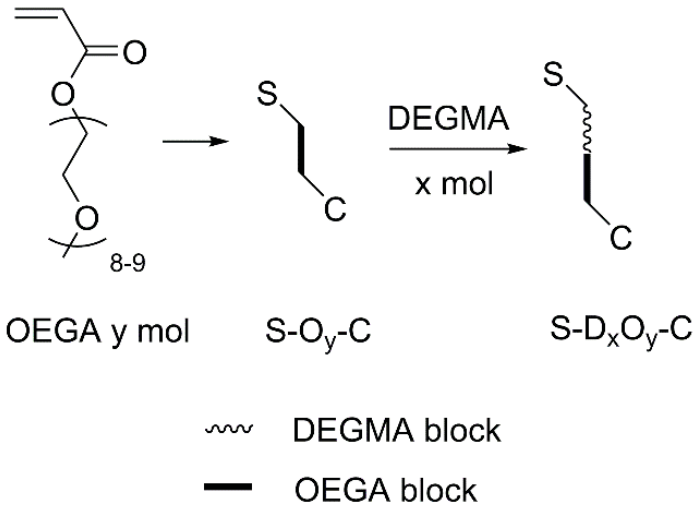


Figure 4.2: Diblock copolymer synthesis procedure

### 4.2.3 Reduction of the Dithioester group to a Thiol group

The dithioester end group is reduced to a thiol using a published aminolysis method.[22] As an example, the thioester (S) end of the S-$D_{50}O_{50}$-C is reduced as follows. Hexylamine (0.13 mL, 10 equiv) is added to a solution of S-$D_{50}O_{50}$-C (2.95 g, 1 equiv) in 3 mL of DCM. The reaction mixture is stirred overnight at room temperature under nitrogen gas protection. The product is precipitated into hexane and dried in vacuo at 25 ˚C for 3 h, giving the thiol terminated polymer, T-$D_{50}O_{50}$-C, in good yield (2.35 g, 79.7%).

### 4.2.4 Synthesis of GNPs (20 nm)

GNPs (20 nm) are prepared using a published method.[23] Specifically, $HAuCl_4$ (20 mg) is

dissolved in 200 mL deionized water, under vigorous stirring, and then heated to boiling. Then 5.0 mL of $Na_3Ct$ solution (containing 52.2 mg $Na_3Ct$) is added dropwise into the solution. The solution turns to a red color and heat and stirring are continued for 2 h more. Then the heat is discontinued and the solution is allowed to stir overnight at room temperature. The resulting solution is filtered through a 0.5 μm membrane filter, and the GNP filtrate solution is stored in a refrigerator at 4 ˚C.

### 4.2.5 Assembly of GNP-polymer hybrid nanoparticles

The GNP-polymer nanoparticles are prepared by slowly dripping a pre-cooled copolymer solution (10 mg / mL, 24 mL aqueous solution) into an aqueous solution of GNPs (100 mL, 0.2 mg/mL). The GNP: polymer mole ratio is 10:1 assuming quantitative yield of GNP from Procedure 3.2.4. This mixture is stirred overnight in darkness and at room temperature. The GNP-polymer nanoparticles are collected by centrifugation (10000 G), and then re-suspended in deionized water to yield 20 mL GNP-polymer solution (GNP concentration: 1 mg/mL). The GNP-polymer solutions are stored at 4 ˚C in darkness.

### 4.2.6 Characterization of diblock copolymers and their GNP-polymer hybrid nanoparticles

Copolymer composition was proven by $^1$H NMR. The spectra that were obtained in $CDCl_3$ on a Varian Unity Inova 400 at 400 MHz. $F_o$ is the ratio of OEGA in the diblock copolymer which was calculated using the integration values from the $^1$H NMR spectra. The full details of the calculation and methods are given elsewhere.[24]

The CPs of the diblock copolymers were measured by UV-vis spectroscopy using a Perkin Elmer UV/vis spectrometer (Lambda 35) equipped with a Peltier based temperature controller. All the spectra, and the CPs of the aqueous copolymer solutions, were determined at a wavelength of λ=500nm. The aqueous solutions were loaded into quartz cuvettes at a concentration (between 5-10 mg/mL sufficient to achieve a starting transmittance of 90%. The transmittance (T%) was recorded at 1 ˚C intervals using an initial heating rate of 1 ˚C/min but once the CP was approached this rate was reduced to 0.1 ˚C/min. The test was concluded when the T% decreased to a minimum of 2% of the maximum T%. Then, all the transmittance values were normalized onto a 0-100% scale. The CP curves were then plotted with normalized transmittance values versus temperature. The temperature at which the normalized T%=50% was defined and recorded as the CP of that specimen.

A dynamic light scattering (DLS) instrument (Coulter NP4 plus, Beckman Coulter, Fullerton, CA) was used to test the hydrodynamic diameter ($D_h$) of the nanoparticles in aqueous solutions. The temperature range tested was from 20 ˚C to 60 ˚C, and measurements made at each 5 ˚C interval using the instrument program.

### 4.2.7 Loading and controlled release of ibuprofen of GNP-diblock copolymer hybrids

The release profile of ibuprofen, a model hydrophobic drug, was measured in phosphate-buffered saline (PBS buffer, pH = 7.4) at 20 ˚C, 37 ˚C, 50 ˚C, and 60 ˚C. The release studies were performed using the hybrid nanoparticles, GNP-$D_{40}O_{60}$-C and GNP-$D_{50}O_{50}$-C. The procedures for the ibuprofen loading and ibuprofen release, are given for GNP-

$D_{40}O_{60}$-C as an example. The drug is loaded by combining the GNP-polymer solution (20 mL, solution concentration 1 mg/mL GNP, as described in section 3.2.5) with ibuprofen (6.0 mg). This mixture is then diluted to a final volume of 30 mL. The mixture is shaken and stirred for 30 min to load ibuprofen into the GNP-polymer particles, and then the nanoparticles and unincorporated drug are separated by centrifugation at 10000 G. The supernatant is collected to calculate the unincorporated ibuprofen, and allow for determining the ibuprofen content in the nanoparticles by mass balance. The precipitate is re-suspended in deionized water to give 10 mL GNP-polymer-ibuprofen solution.

The drug release tests are performed by separating this 10 mL solution into 4 dialysis tubes, with each tube containing 2.5 mL GNP-polymer-ibuprofen solution (5 mg GNP and 1.5 mg ibuprofen). These 4 dialysis tubes are then immersed in 50 mL of PBS buffer for controlled release tests over 24 h at 20 ˚C, 37 ˚C, 50 ˚C and 60 ˚C independently. The beakers containing the dialysis tubes are sealed to maintain constant volume during controlled release tests. At each selected time interval, a 1.5 mL aliquot of PBS solution containing released drug is collected from the beaker and the same volume of fresh PBS buffer is added back to keep the total volume constant. This procedure is repeated until the release test is completed. Each reported data point is the result of 3-5 replicate experiments. The amount of ibuprofen released was calculated against standard curves (Figure 4.3), prepared from PBS buffer. The absorption peak of ibuprofen by UV-*vis* spectrometry is at 264 nm, however, because of the low solubility of the ibuprofen, the highest concentration possible in PBS was 0.055 mg/mL.

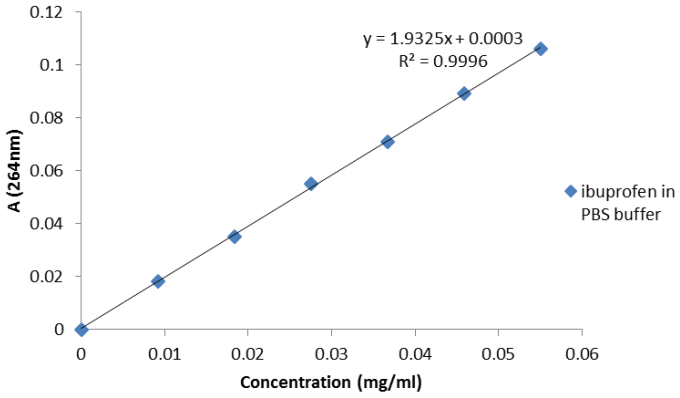


Figure 4.3 Standard curve of ibuprofen in PBS buffer.

Equation 4.1 shows how the ibuprofen concentration is determined.

$$c = (A - 0.0003) / 1.9325 \quad \text{unit: mg / mL} \qquad \text{Equation 4.1}$$

## 4.3 Results and discussion

Our objective was to prove the hypothesis that a high CP polymer matrix could be used as a drug carrier that would reduce the loss of drug occurring near the temperature of the human bloodstream (i.e. 37 ˚C) but achieve an efficient triggered release at a desired higher temperature, and to determine how much reduction in the premature drug release the higher CP would permit. This release would, in principle, be induced by photothermal heating of the GNP-polymer hybrid nanoparticles. A CP between 50 ˚C to 60 ˚C was postulated as a suitable range for this objective, as it was thought the CP was high enough to have limited release below 40 ˚C but significant release at e.g. 45 ˚C, which is easily achieved by photothermia. Based on prior published results[24], we choose S-$D_{50}O_{50}$-C (CP=51.9 ˚C) and S-$D_{40}O_{60}$-C (CP=58.9 ˚C) as the two diblock copolymers

to be studied.

These two copolymers were synthesized and characterized with both the dithioester and the thiol chain ends, then the GNP-polymer hybrids were prepared and characterized, to ensure similar nanoparticle size and that the CP was in the desired range; and finally the drug release profiles for the GNP-polymer nanoparticles were assessed above and below the CPs, using ibuprofen as the model drug.

## 4.3.1 Characterization of the Diblock Copolymers

### 4.3.1.1 Composition

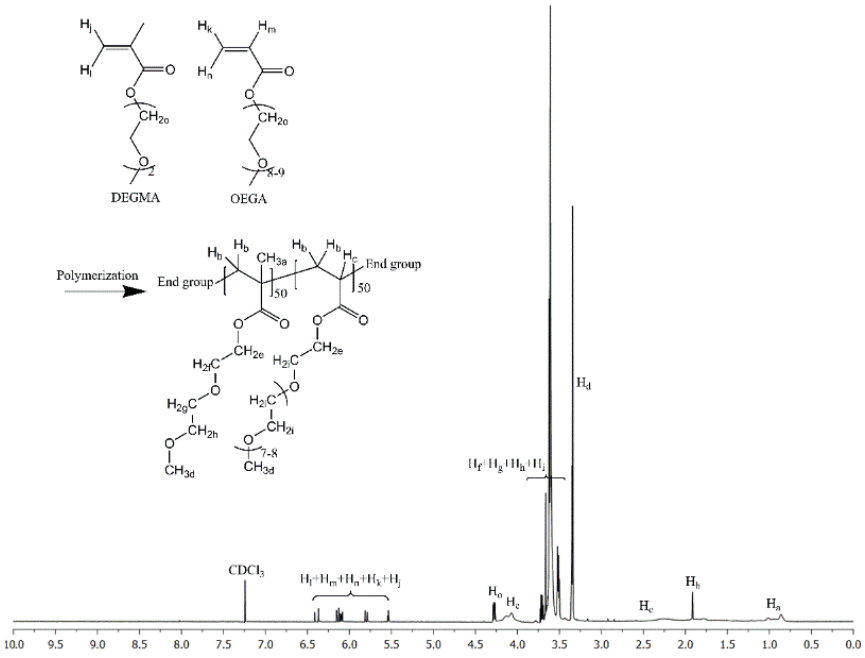


Figure 4.4 The $^{1}$H NMR spectrum of S-$D_{50}O_{50}$-C.

$$\frac{3\times(1-Fo)+3\times Fo}{6\times(1-Fo)+32\times Fo} = \frac{integration\ of\ Hd}{integrations\ of\ (Hf+Hg+Hh+Hi)} \qquad \text{Equation 4.2}$$

The copolymers S-$D_{50}O_{50}$-C and S-$D_{40}O_{60}$-C were synthesized at a theoretical monomer ratio of 50:50 and 40:60. $^{1}$H NMR (Figure 4.4) shows the typical absorbance peaks of the

hydrogen atoms of OEGA and DEGMA using the copolymer S-$D_{50}O_{50}$-C. The peaks appear at the same positions for S-$D_{40}O_{60}$-C. The actual composition of OEGA/DEGMA was then calculated using Equation 4.2. The specific H atoms are identified in Figure 4.4 and Fo is the mole fraction of OEGA monomer in the polymer.)

The conversion of the dithioester chain end to a thiol by aminolysis[22] is evident visually as shown in Figure 4.5a. The dithioester copolymer gives a golden-yellow colored solution in methylene chloride but after the aminolysis the thiol-terminated copolymer solution is a pale yellow.


Figure 4.5a Photos showing the change in color after a solution of S-$D_{50}O_{50}$-C (dithioester end group) dissolved in $CH_2Cl_2$ (left) is subjected to aminolysis to give a thiol-terminated copolymer T- $D_{50}O_{50}$-C in $CH_2Cl_2$ (right, after the product is isolated and re-dissolved in $CH_2Cl_2$).

The change in end group is confirmed by comparing the FTIR spectra of S-$D_{50}O_{50}$-C and T-$D_{50}O_{50}$-C (Figure 4.5b). The end groups comprise a small portion of the polymer chain, nevertheless after aminolysis a distinct reduction is seen in bands associated with the aromatic ring; i.e. the C=C bending peak at 1639 $cm^{-1}$ is reduced and the aromatic C-H bending peak at 873 $cm^{-1}$ shows that the sharp band from the dithioester appears to have disappeared from the spectrum of T-$D_{50}O_{50}$-C.

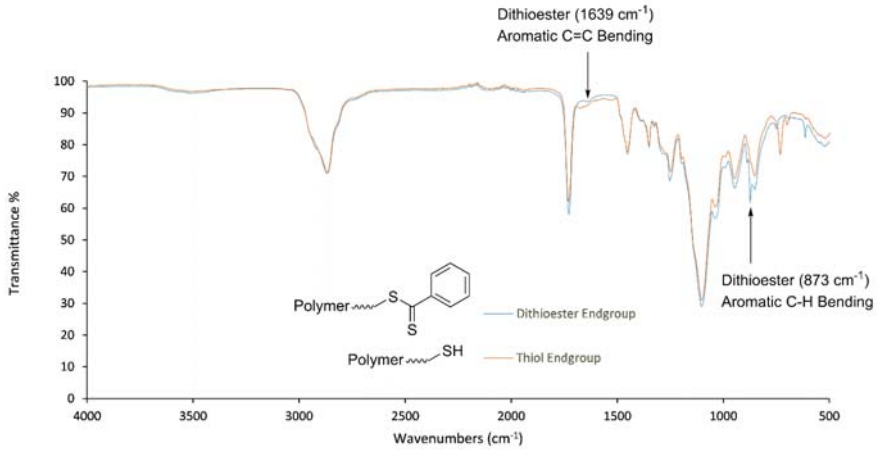


Figure 4.5b FTIR of S-$D_{50}O_{50}$-C and T-$D_{50}O_{50}$-C

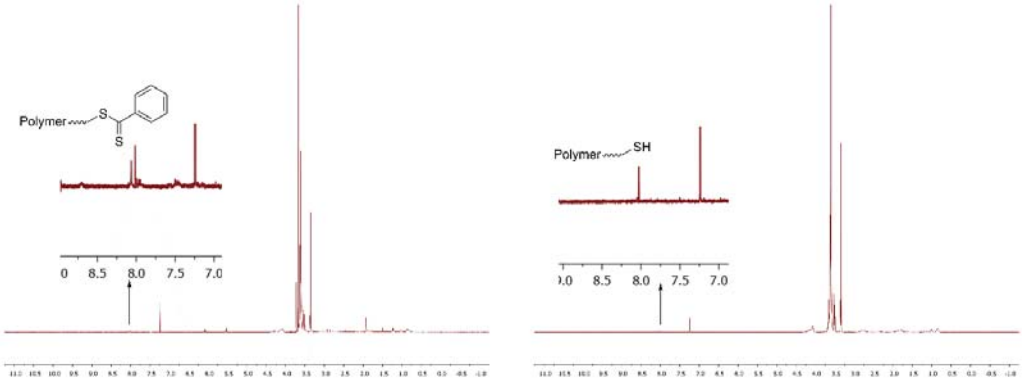


Figure 4.6 $^{1}H$ NMR of S-$D_{50}O_{50}$-C (left) and T-$D_{50}O_{50}$-C (right).

The $^{1}$H NMR spectra also support the successful conversion of the dithioester to thiol, as shown in Figure 4.6. The bands at 7.4-8.5 ppm are clearer in the T-$D_{50}O_{50}$-C copolymer with thiol end groups than in the S-$D_{50}O_{50}$-C copolymer with dithioester end groups. Other differences in the spectrum of S-$D_{50}O_{50}$-C, are observed where several peaks belonging to the benzene ring are seen at 7.4, 8.0, 8.1 and 8.6 ppm, while in the spectrum of T-$D_{50}O_{50}$-C, only a single peak at 8.0 ppm is seen. Collectively, all these changes support the successful conversion of the dithioester chain ends to thiol chain ends.

#### 4.3.1.2 Characterization of T-$D_{50}O_{50}$-C and T-$D_{40}O_{60}$-C

The experimentally determined copolymer composition along with the CP and $D_h$ of the copolymers are summarized in Table 4.1. While the synthesis targeted equal block lengths for the OEGA and DEGMA blocks, analysis showed that the percent yield of OEGA was higher, and so the length of the OEGA block in the copolymer was longer than theoretical, while the percent yield of DEGMA in the copolymer was closer to the target. This is thought to be due to the fact that the OEGA block is synthesized first, and the pendant oligomeric ethylene glycol unit may result in some hindrance around the reaction site.

Table 4.1 Characteristics of the Diblock Copolymers

| Sample | $Y_D$(yield %) | $Y_O$(yield %) | $Y_{overall}$(%) | Fo (%) | CP(°C) | $D_h$(nm) |
|---|---|---|---|---|---|---|
| S-$D_{50}O_{50}$-C | 47 | 83 | 73.0 | 49 | 51.9 | 165 |
| T-$D_{50}O_{50}$-C | - | - | 79.7[a] | - | 51.5 | - |
| S-$D_{40}O_{60}$-C | 62 | 83 | 79.0 | 57 | 58.9 | 132 |
| T-$D_{40}O_{60}$-C | - | - | 85.0[a] | - | 59.8 | - |

[a] Aminolysis yield from S-DxOy-C, [b] Calculated from Equation 4.2

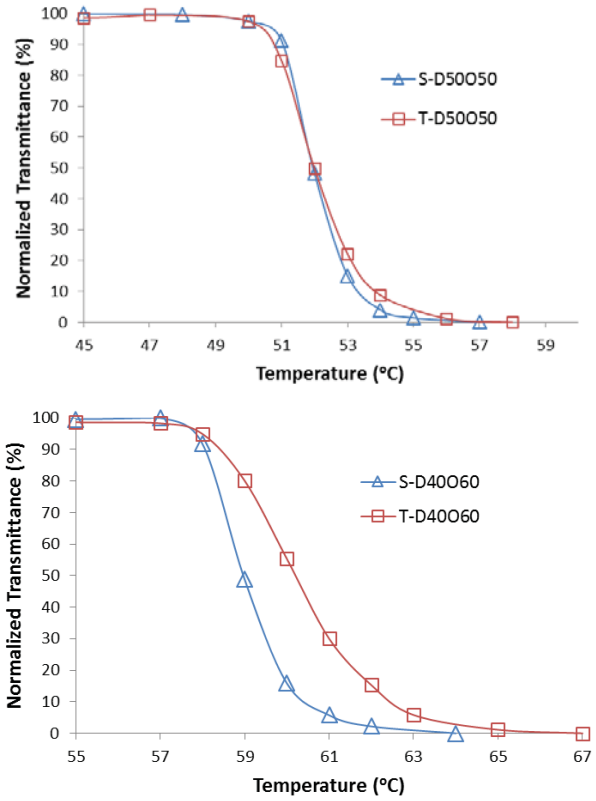


Figure 4.7 CP curves of a) S-$D_{50}O_{50}$-C and T-$D_{50}O_{50}$-C; and b) S-$D_{40}O_{60}$-C and T-$D_{40}O_{60}$-C

Figure 4.7 shows the CP curves of the S-DxOy-C and T-DxOy-C. The change of end group has little effect on CP, but the compositional change between the two block copolymers caused a difference in CP of ~7 ˚C, with the S/T-$D_{50}O_{50}$-C having a CP of ~52 ˚C and S/T-$D_{40}S_{60}$-C having a CP of ~59-60 ˚C. Because the copolymers now possessed the desired thiol end groups and the CPs were in the target range of 50-60 ˚C the copolymers were then bonded to the GNPs.

## 4.3.2 GNP-polymer nanoparticles

### 4.3.2.1 Characterization of GNP-polymer nanoparticles

Gold nanoparticles with a 20 nm diameter were prepared using established methods. Gold nanoparticles of this size form a ruby red solution as shown in Figure 4.8 (left). However, once these nanoparticles are completed with the thiol terminated nanoparticles the color changes to a light purple (Figure 4.8, right), and the resulting hybrid nanoparticles have a $D_h$ of ~70 nm.

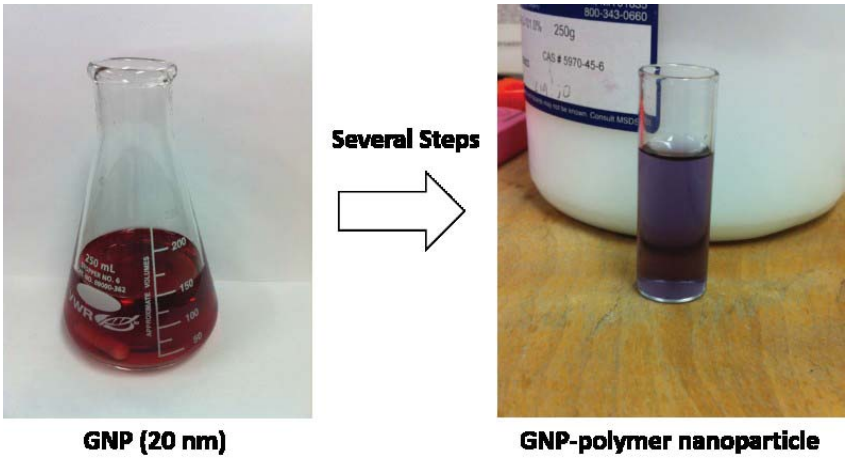


Figure 4.8 Color of GNPs (left) and GNP-polymer nanoparticles (right).

### 4.3.2.2 DLS analysis of GNP-polymer hybrids

Interestingly, in this work we failed to observe the CP of the GNP-polymer hybrids, while in prior research in our lab the CP of the GNP hybrids was clearly visible.[23]. In that prior work, the dithioester group was reduced to thiol by $NaBH_4$, whereas in this work aminolysis was used to convert the diothioester group to a thiol. Aminolysis (Figure 4.9) only reacts with the dithioester chain end, while reduction with $NaBH_4$ may reduce the diothioester as well as some of the carbon-oxygen double bonds of the polymer side

chains. This may account for some changes in the thermoresponsive properties between the two systems based on the reduction mechanism.

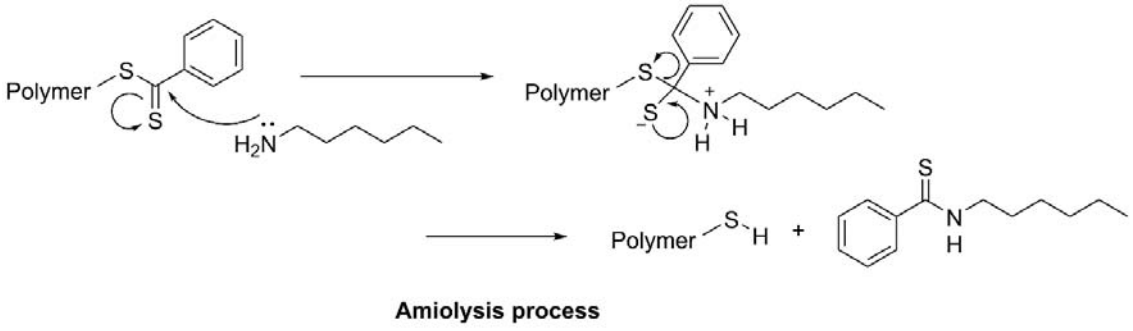


Figure 4.9 The mechanism of aminolysis.

GNP-polymer hybrids of the type S/T-DxOy-C will naturally form a core-shell structure in water. The GNP is expected to form the core leaving the amphiphilic diblock to form a two part shell: the more hydrophobic DEGMA block will form an inner shell and the more hydrophilic OEGA block will form the external shell. This design is also expected to result in most of the hydrophobic drug loading into the internal shell, while the external OEGA shell aids the stabilization of the GNP-polymer hybrid nanoparticles in aqueous media. The CP (Table 4.1 and Figure 4.7) of the diblock copolymers did not change much by converting the diothioester end group to a thiol, but it was expected that coupling that chain end to a GNP would have a greater effect on the thermoresponse properties. UV-vis failed to detect any change in transmittance, which means there was no aggregation when the temperature increased (Figure 4.10a). However, the DLS showed distinct reductions in the $D_h$ when the temperature increased, especially from 30 ˚C to 35 ˚C. Although OEGA is more hydrophilic than DEGMA, both are hydrophilic monomers. When the GNPs bond to the thiol end groups and become the core of the polymer, this reduced the ability of the nanoparticles to aggregate (Figure 4.10b).

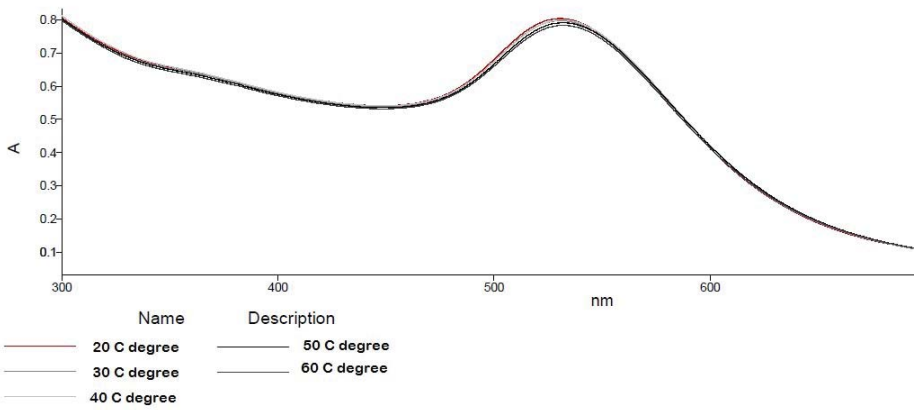


Figure 4.10a Temperature dependent spectra of GNP-$D_{50}O_{50}$-C

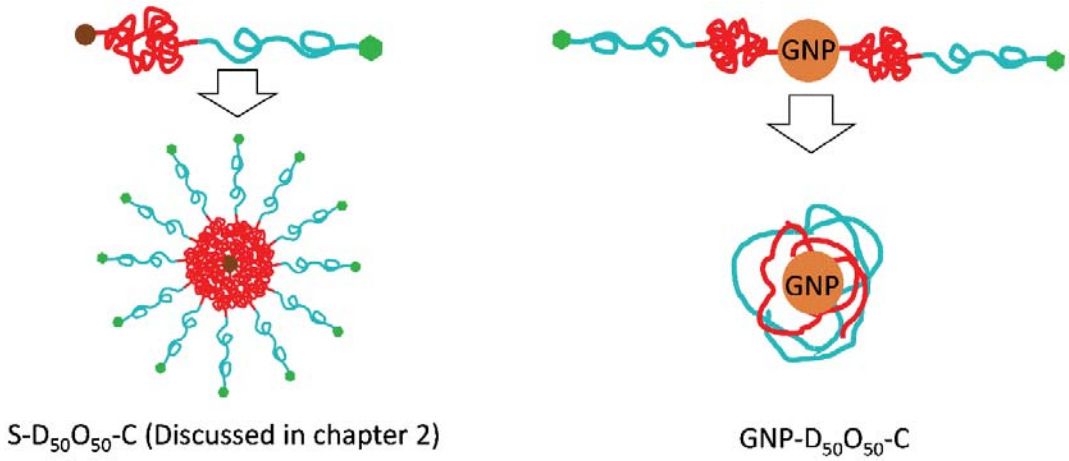


Figure 4.10b Proposed structure differences of S-$D_{50}O_{50}$-C and GNP-$D_{50}O_{50}$-C in aqueous solution.

These effects are evident in the temperature-dependent $D_h$ data, as shown in Table 4.2. The 20 ˚C $D_h$ supports the structures shown in Figure 4.10b, with S-$D_{50}O_{50}$–C having a diameter of 165 nm and GNP-$D_{50}O_{50}$–C having only a 74 nm diameter. Figure 4.11 shows the differences in the temperature-dependent $D_h$ of S–$D_{50}O_{50}$–C and its GNP hybrid, while Figure 4.12 compares the temperature-dependent $D_h$ of both GNP-hybrid nanoparticles, GNP–$D_{50}O_{50}$–C and GNP–$D_{40}O_{60}$–C. The $D_h$ of the free polymer, S-

$D_{50}O_{50}$-C, is initially ~169 nm and rises to 222 nm at 30 ˚C and continues to rise until 45 ˚C, where it reaches a diameter of 279 nm. These data suggest increased aggregation of the diblock copolymer, which obscures the collapse of the DEGMA block, which is expected to be between 20-30 ˚C. However a small decrease of ~ 20 nm is then observed between 45–50 ˚C, where the $D_h$ is 257 nm. This is attributed to the beginning of the collapse of the OEGA block, which has a CP of 51.9˚C (Table 4.1). As the temperature rises further the $D_h$ rapidly decreases to 89 nm at 55 ˚C, but then rises again to 214 nm at 60 ˚C due to further aggregation of the polymer coils.

Table 4.2 $D_h$ of GNP-hybrid polymers and block copolymer

| $D_h$(nm) under different Temperature | 20°C | 25°C | 30°C | 35°C | 40°C | 45°C | 50°C | 55°C | 60°C |
|---|---|---|---|---|---|---|---|---|---|
| GNP-$D_{50}O_{50}$-C | 74.4 | 74.2 | 70.9 | 50.6 | 45.2 | 41.7 | 37.5 | 35.5 | 32.9 |
| GNP-$D_{40}O_{60}$-C | 76.9 | 75.1 | 75.6 | 54.6 | 48.8 | 44.6 | 39.8 | 36.6 | 34.8 |
| S-$D_{50}O_{50}$-C | 164.9 | 168.7 | 222.2 | 256.3 | 251.2 | 279.2 | 256.8 | 89.3 | 213.9 |

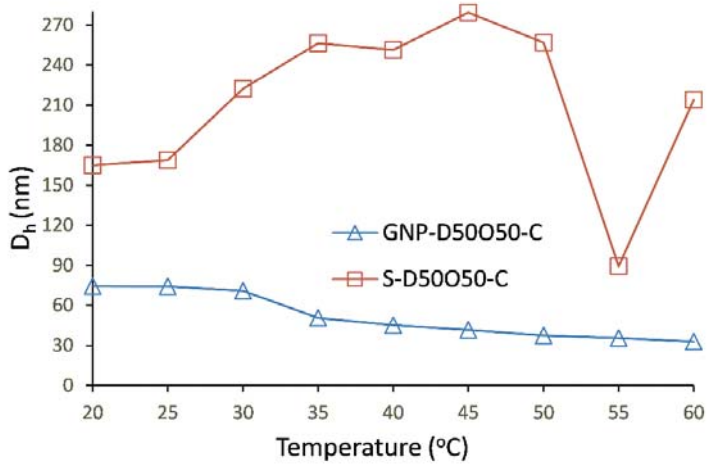


Figure 4.11 Temperature-dependent $D_h$ of S-$D_{50}O_{50}$–C and its GNP-hybrid nanoparticle

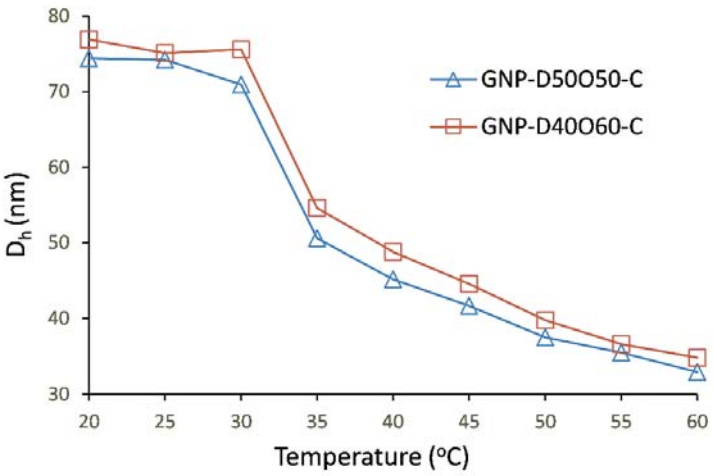


Figure 4.12 The Temperature-dependent $D_h$ of the GNP-hybrid nanoparticles

Figure 4.12 compares the temperature-dependent changes in $D_h$ of GNP-$D_{50}O_{50}$-C with that of GNP-$D_{40}O_{60}$-C. Both GNP-hybrid nanoparticles have an initial size of ~ 75 nm. This is between that of the GNPs (20 nm) and the $D_h$ of the free polymers (~ 165 nm for S-$D_{50}O_{50}$-C and ~ 132 nm for S-$D_{40}O_{60}$-C). This supports the model for the GNP-hybrid nanoparticles shown in Figure 20, which shows the polymer chains coiled about the GNP core instead of extending into the aqueous solution. From 20 ˚C to 30 ˚C, the $D_h$ remained near 70 nm, however, the $D_h$ of both GNP-hybrid nanoparticles decreased significantly at 35 ˚C. This is consistent with the collapse of a DEGMA block though it is not clear which block is collapsing.

If the above transition is from DEGMA, then the transition of the OEGA block in the GNPs is unclear. The $D_h$ of the GNP-$D_{50}O_{50}$-C and GNP-$D_{40}O_{60}$-C hybrid nanoparticles both show a slow continued decline between 40-60 ˚C. For GNP-$D_{50}O_{50}$-C the $D_h$ declined an additional 27.2% (45.2–32.9 nm) and for GNP-$D_{40}O_{60}$-C there was an additional decline of 28.7% (48.8–44.8 nm). At 60 ˚C, both these hybrids have 13-15 nm

organic shells surrounding the 20 nm GNP core, so the copolymer seems fully collapsed at this temperature, which is the upper limit of the instrument. The fact that no CP was detected shows that there is no aggregation of the GNP-hybrid nanoparticles, but the coil collapse also shows that these polymers do not have the expected higher temperature thermo-response properties and ideally narrow transition window needed to test our premise of being able to significantly reduce drug release at normal body temperature and efficiently release the drug at higher temperature.

### 4.3.3 Nanoparticle drug loading and controlled release from the nanoparticles

Although the thermo-response properties were not ideal the GNP-hybrid nanoparticles were taken to the next step, which was loading with ibuprofen and studying the release properties. Figure 4.13 shows the UV-*vis* spectrum of ibuprofen. The first spectrum is run at standard absorbance levels which is in the range of 0.1~0.9. The major absorbance band for ibuprofen is at 264 nm, while the standard Uv-*vis* range is from 300 nm to 800 nm. Furthermore, the absorbance (A) of ibuprofen is very low (0.06) which is too low to have high quantitative accuracy, but the second spectrum in Figure 4.13 shows the expanded absorbance scale to obtain quantitative data, though it is expected to have higher than usual range of error, so the conclusions from these release data can only be based on trends.

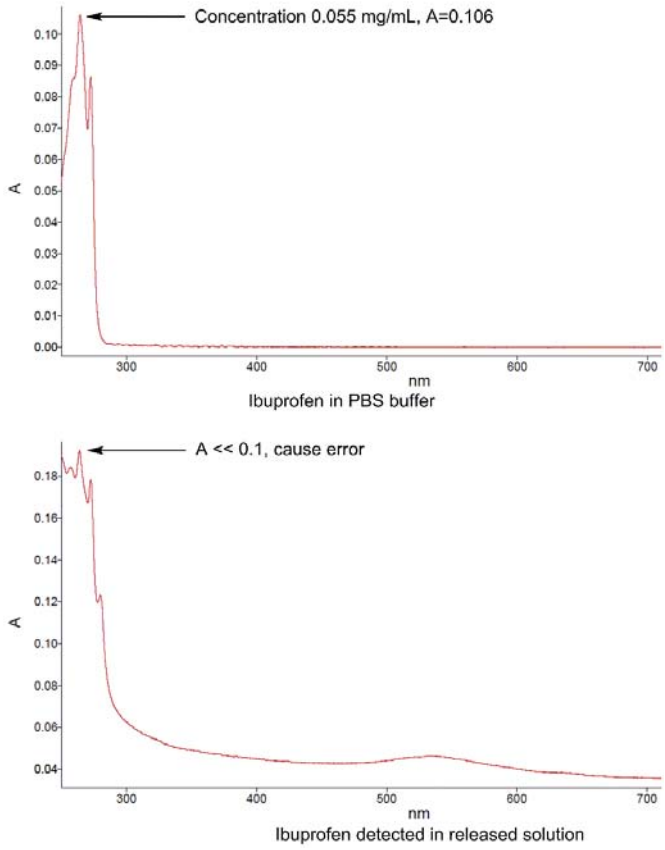


Figure 4.13 Uv-*vis* spectrum of ibuprofen

Once ibuprofen was loaded into the GNP-hybrid nanoparticles the loading efficiency was determined by isolating the free drug in the nanoparticle supernatant after centrifugation. Then, the mass balance was used to back-calculate the loaded drug. To ensure that the mass that was isolated from the supernatant did not contain any free diblock copolymer, the supernatant was dialyzed using a dialysis tube with a cutoff molecular weight was 3500 g/mol. Therefore, both residual GNP and polymer were retained in the dialysis tube, and only the ibuprofen passed into the aqueous bath. After dialysis, the extracted aqueous solutions were combined and concentrated to 30 mL. The mass of the ibuprofen in the supernatant (Ms) was calculated using Equation 4.1. Based on the total mass of ibuprofen

(Mt), the loading efficiency and actual amount loaded were found by Equations 3.3 and 3.4.

Loading efficiency = (Mt – Ms) / Mt × 100% Equation 4.3 Loading efficiency

Actual loading drug in GNP-polymers = Mt – Ms Equation 4.4 Actual loading amount

As shown in Table 4.3, ibuprofen was efficiently loaded into the nanoparticles at 90.0% and 95.4% into GNP-$D_{50}O_{50}$-C and GNP-$D_{40}O_{60}$-C respectively

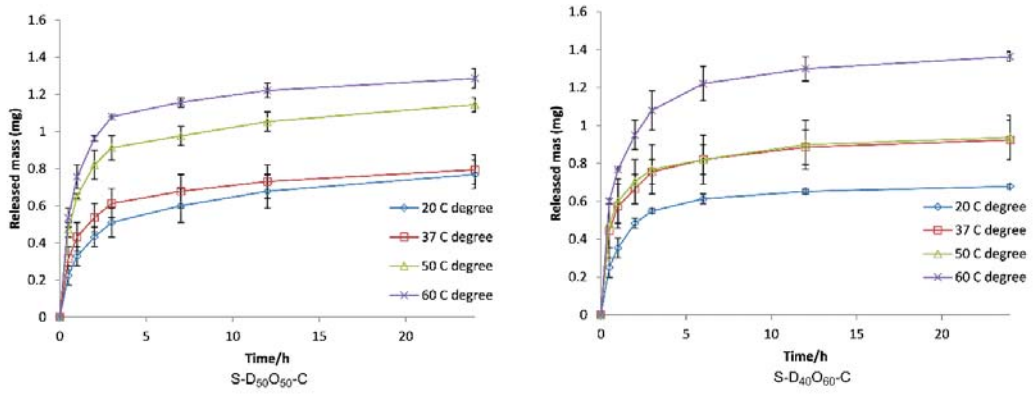


Figure 4.14a: The release curve mass vs time: a) GNP-$D_{50}O_{50}$-C b) GNP-$D_{40}O_{60}$-C

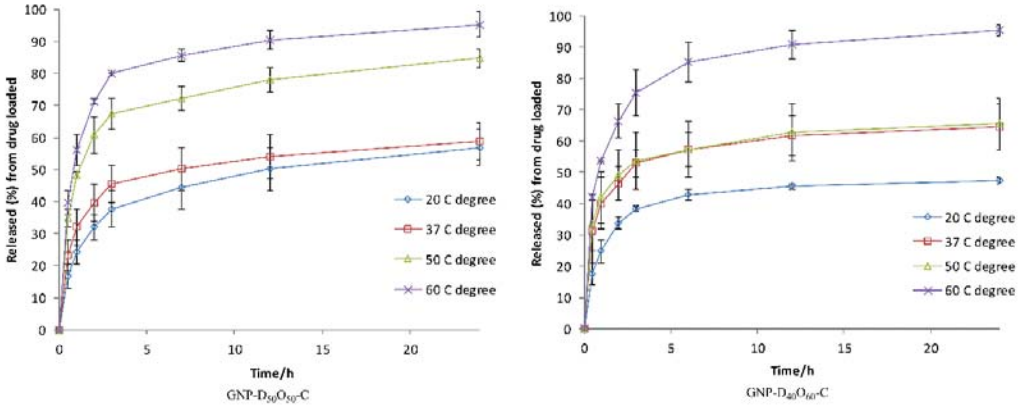


Figure 4.14b: The percent release (%) curve from drug loaded vs time:a) GNP-$D_{50}O_{50}$-C b) GNP-$D_{40}O_{60}$-C

Table 4.3 Loading efficiency and release data

| Sample | Ibuprofen (mg) | GNP (mg) | Loading efficiency (%)[a] | Drug release (%) at 0.5 h | | | | Drug release (%) at 24 h | | | |
|---|---|---|---|---|---|---|---|---|---|---|---|
| | | | | 20 ˚C | 37 ˚C | 50 ˚C | 60 ˚C | 20 ˚C | 37 ˚C | 50 ˚C | 60 ˚C |
| **GNP-$D_{50}O_{50}$-C** | 1.5 | 2.5 | 90.0 | 16.7 | 23.4 | 34.9 | 39.7 | 57.0 | 58.5 | 84.4 | 94.8 |
| **GNP-$D_{40}O_{60}$-C** | 1.5 | 2.5 | 95.4 | 17.5 | 31.1 | 33.8 | 41.9 | 47.5 | 64.6 | 65.5 | 95.0 |

[a] Loading efficiency were calculated using Equation 4.3

Table 4.3, Figure 4.14a and Figure 4.14b reveal several important features. Figure 4.14a and Figure 4.14b shows the release profiles of ibuprofen, from both GNP-$D_{50}O_{50}$-C and GNP-$D_{40}O_{60}$-C nanoparticles at 20, 37, 50 and 60 ˚C. They all appear to show typical diffusion-controlled release at all four temperatures that were tested over a 24 h period. The temperatures were 20 ˚C, which is below the CP for PDEGMA, 37 ˚C which is body temperature and above the reported CP for PDEGMA but below that of the OEGA block, 50 ˚C which is near the observed CP of the copolymers, and 60 ˚C which is above the CP of both diblock copolymers. From Table 4.3 it can be seen that at 20 ˚C and 0.5 h the amount of drug released is similar at 16.7% and 17.5 % for GNP-$D_{50}O_{50}$-C and GNP-$D_{40}O_{60}$-C nanoparticles respectively, which is less than 1 wt% difference. However, after 0.5 h at 37 ˚C there is a 7.7 wt% difference in released drug with 23.4 wt% released from GNP-$D_{50}O_{50}$-C and 31.1 wt% released from GNP-$D_{40}O_{60}$-C. The results from hydrodynamic diameter (Table 4.2) showed that the thermally-triggered collapse of the DEGMA block occurs somewhere near 35 ˚C, so the difference suggests the $D_{40}$ block

may have collapsed more effectively than the longer $D_{50}$ block to release slightly more ibuprofen. The release is not thought to be due to greater diffusion-controlled release from the more polar GNP-$D_{40}O_{60}$-C nanoparticle because after 0.5 h at 50 ˚C the release from the GNP-$D_{50}O_{50}$-C nanoparticle "caught up" and slightly exceeded that from the GNP–$D_{40}O_{60}$-C nanoparticle, though the difference is only 1.1 wt. % greater. And then, after 0.5 h at 60 ˚C, which is thought to exceed the CP of OEGA block, although it was not detected by UV-*vis*, the drug release from GNP–$D_{40}O_{60}$-C exceeded that of GNP-$D_{50}O_{50}$-C by 2.2 wt. %. These differences are too small to be definitive, but the change in trends near he expected CP of the OEGA blocks supports the different impact from even small changes in block length.

The 24 h data also support a diffusion release that is combined with a stimulated release. As with the 0.5 h release data, at 60 ˚C the amount of drug released by the two different nanoparticle systems is nearly identical, at 94.8% and 95.0% for GNP-$D_{50}O_{50}$-C and GNP-$D_{40}O_{60}$-C nanoparticles respectively. However, there are significant differences after 24 h for the other release temperatures. At 20 ˚C the GNP-$D_{50}O_{50}$-C had released 9.5% more drug than GNP-$D_{40}O_{60}$-C nanoparticles, but at 37 ˚C there was little change in the drug release from GNP-$D_{50}O_{50}$-C nanoparticles while GNP-$D_{40}O_{60}$-C nanoparticles had released much more. This is the same trend as observed after 0.5 h, and suggests that the $D_{40}$ DEGMA block releases drug at a lower temperature than the $D_{50}$ DEGMA block. Once the temperature is raised to 50 ˚C, there is little additional drug release from the $D_{40}$ DEGMA block, presumably because this block has already released its drug, but a significant increase in released drug (25.9 wt. %) is now seen from GNP-$D_{50}O_{50}$-C nanoparticles. Therefore this higher temperature was required for collapse of the larger

$D_{50}$ DEGMA block. Finally, at 60 ˚C, a significant additional drug release of 29.5 wt. % is seen from the GNP-$D_{40}O_{60}$-C nanoparticles while an additional 10.4 wt. % drug release is measured from. GNP-$D_{50}O_{50}$-C nanoparticles. At 60 ˚C both nanoparticle systems had released about 95% of the drug, so the large difference in amount of drug released between 50 and 60 ˚C may be that a higher temperature was required to completely collapse the $O_{60}$ block in the GNP-$D_{40}O_{60}$-C nanoparticles than was required to collapse the $O_{50}$ block in the GNP-$D_{50}O_{50}$-C nanoparticles, and the complete collapse of the OEGA block was needed to release all the drug.

Even though the CP of the GNP-hybrid nanoparticles was not observed by UV-*vis*, these trends in drug release are consistent with a higher CP for the OEGA block, and the CPs of the thiolated copolymers are consistent with this. The CP of T-$D_{50}O_{50}$-C was measured at 51.5 ˚C while the CP of T-$D_{40}O_{60}$-C was measured at 59.8 ˚C.

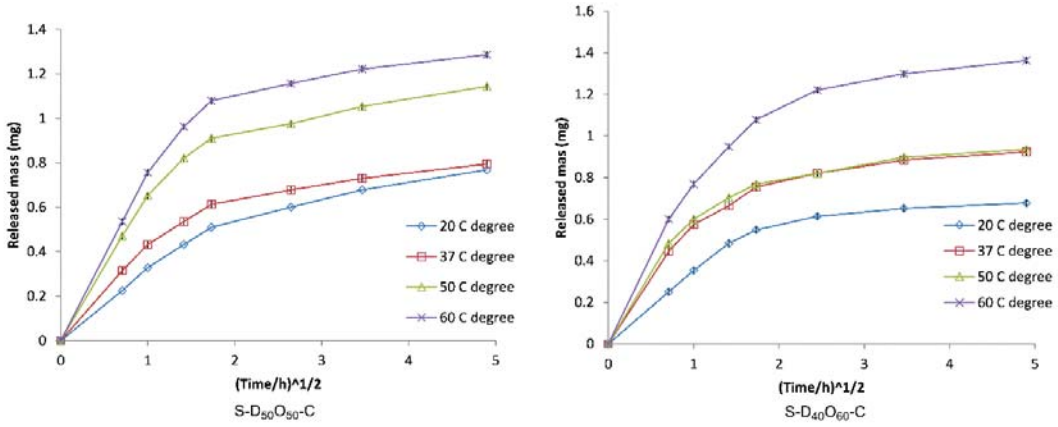


Figure 4.15 Ibuprofen release shown as release mass vs. time^1/2

To see if the drug release data were explained by diffusion alone the data were re-plotted as a function of the square root of time, which should give a straight line for standard first order release[25] (Figure 4.15). The initial drug release does appear linear, suggesting diffusion dominates the release initially, but the later release shows deviations from

linearity. These results do support two drug release mechanisms in operation.

## 4.4 Conclusions

EG-containing polymers are known to be biocompatible and acrylate and methacrylate polymers with pendant EG units seem likely to have a good future in the field of drug delivery due to their ability to be both thermo-responsive and resist protein absorption to extend survival time in the circulatory system. GNPs also appear to have value in biomedical applications such as hyperthermia. In this research we sought to combine the advantages of GNPs, which strongly absorb biologically safe wavelengths of light (530 nm) and convert it to heat, with the advantages of thermo-responsive amphiphilic copolymers from DEGMA and OEGA. The perceived advantages of this design were that less hydrophilic DEGMA block was intended to provide a domain for hydrophobic drugs while the OEGA block was intended to provide a stabilizing and non-protein absorbing shell and a relatively high CP so that relatively small amounts of drug would be released at normal body temperatures while the GNP core could be used to heat the local environment to stimulate drug release at the desired time once the nanoparticles reached a target location.

In this work two amphiphilic diblock copolymers were prepared and tested to determine the value of the design, T-$D_{50}O_{50}$-C and T-$D_{40}O_{60}$-C, with CPs of 51.5 ˚C and 59.8 ˚C, respectively, were prepared, and bonded to GNPs and then loaded with ibuprofen. At 37 ˚C the GNP-$D_{50}O_{50}$-C released only 23.4% of the drug after 30 mins, but at 50 ˚C released almost 35% after 05 h, and more than 84% after 24h. The higher length OEGA

block required higher temperatures for similar release. The data show that significant release of drug is achieved by collapsing the inner, lower CP block, but collapsing the outer higher CP block is necessary to achieve near quantitative drug release near 95%.

Overall these experiments support the hypothesis and gave some promising results. However, better results would be expected with a drug that is somewhat less hydrophobic to permit higher drug loading, and a drug that gives a higher absorbance above 300 nm would give more accurate results. Because of this, future work should use a better model drug, such as 4′, 5′-dibromofluorescein or fluorescein. Better release results might also be expected with a DEGMA-OEGA copolymer for an inner block with a slightly higher CP to lower the short-term drug release while retaining a suitable domain for the hydrophobic drug, while maintaining an external OEGA block to ensure complete release at a stimulated temperature.

# Chapter 5 Peptide-Directed Self-Assembly of Functionalized Polymeric Nanoparticles: Multiple Drug Loading Ability[b]

## 5.1 Introduction

Efficient tissue regeneration often depends on the delivery of various drugs (i.e. low or high molecular weight agents including growth factors) at appropriate rates to implanted cells. Therefore, understanding the relationship between tissue engineering, scaffolding systems, and drug delivery is crucial for the design of functional scaffolds for the desired applications.[1] For example, skin regeneration usually requires the delivery of a complex mixture of growth factors and cytokines, (e.g. fibroblast growth factor, keratinocyte growth factor, vascular endothelial growth factor and interleukin 1α) within the wound to promote cell proliferation and migration for wound healing.[2] Therefore, the fabrication of sophisticated scaffolding systems with the ability to physically support cells and at the same time deliver an appropriate "drug cocktail" at an appropriate rate to promote cell growth and health is an important advance for tissue engineering.

Self-assembled peptide nanofiber scaffolds have gained in popularity compared to scaffolding from other polymers, possibly because they are perceived as non-toxic and biodegradable, and the porous fibril structures are thought to be similar to extracellular matrix (ECM) and so will aid cell attachment.[3] Also, these materials can assemble in situ into a hydrogel at physiological environment.[3l, 3m] The first reported self-assembling "designer peptide" was EAK16-II (AEAEAKAKAEAEAKAK), isolated from a yeast

[b] The material contained in this chapter was previously published in *Macromolecular Bioscience*. See Appendix C for documentation of permission to republish this material.

protein, zuotin.[4] EAK16-II spontaneously self-assembles into stable β-sheets in aqueous conditions across a broad range of temperature and pH, even in the presence of significant quantities of a denaturing agent, such as urea or guanidium hydrochloride.[5]

The self-assembling process is driven by the hydrophobic interactions of alanine (A) domains and ion-pair interactions between negatively charged glutamic acid (E) side chains with positively charged lysine (K) side chains. The importance of the strong ion-pair interaction for successfully forming the β-sheet was supported by investigation of a complementary pair of designer peptides, that were self-repulsing but possessed strong mutually attracting peptide sequences where one of the pair possessed a sequence with positive charges (Ac-WKVKVKVKVK-amide) and the other sequence with negative charges (Ac-EWEVEVEVEV-amide).[6] On mixing this pair of complementary peptides, a rapid assembly into a viscoelastic hydrogel occurred at a concentration as low as 0.25 wt. %. This hydrogel retained mechanical strength, even after repeated shear-induced breakdowns, due to the electrostatic interactions. The strong electrostatic and selective interaction between the opposite charges demonstrated one of the key merits of using ion-complementary β-sheet motifs.

Other designer self-assembling peptide hydrogels (e.g. RADA16-I or II) have also been studied and they, along with EAK16-II, have been widely used as both controlled drug delivery systems and 3D scaffolds.[7] The drug delivery method is typically a simple physical mixing of a drug into the peptide mixture during the gel formation,[7-8] but it can also be chemically bonded onto the C-terminal or N-terminal.[9] Sometimes a combination of both methods is used to load multiple active agents.[10]

However, these methods all have significant limitations with respect to the quantity of drug(s) that can be incorporated, as well as the real possibility that the incorporated drug(s) may have a detrimental effect on the subsequent self-assembly process or the mechanical stability of the formed hydrogel. There is also a very limited ability to control the release rate of drugs with different properties. Therefore, the peptide itself must be designed in conjunction with the specific drug(s) that will be incorporated. Moreover, the effective distribution of multiple drugs in scaffolds is not easy to achieve.

In previous work from our group, we demonstrated a new approach to fabricate tissue scaffolding, prepared by peptide-directed self-assembly of polymeric nanoparticles into fibers and 3D scaffolds, to address these limitations.[11] This type of assembled scaffolding system is achieved by functionalizing amphiphilic triblock copolymers with self-assembling ionic complementary peptides (P1-ABA-P1 and P2-ABA-P2). The triblock copolymer (ABA) is assembled into a core-shell nanoparticle to contain a desired drug, while the carboxylic chain ends are modified by appropriate peptides (P1 or P2) to give the peptide-functionalized core-shell nanoparticles (e.g. P1-NP-P1 and P2-NP-P2). That paper described the synthesis and assembly of the nanoparticle fiber scaffolds, demonstrated the ability to contain low and high molecular weight model drugs, and proved the incorporation and controlled release of insulin from the peptide conjugate nanoparticles and the assembled scaffold. The first paper also described other potential variables that affected scaffold morphology and the advantage of being able to design and make assembled nanoparticle scaffolds where different desired drugs could be incorporated into a nanoparticle that had a size, composition, and release rate that were designed for that drug. The size of the particles is controllable and can range from nano-

to microparticle, and can be designed to swell significantly or only a little in aqueous media depending on the composition and size of the shell in core-shell particle scaffolds. When the peptide-functionalized nanoparticles are combined they assemble into continuous "nanoparticle fibers" and, given time, 3D scaffolds form that have a "sponge-like" appearance in aqueous solution.

The nanoparticle self-assembly approach is expected to possess the ability to: (1) incorporate multiple drugs, regardless of that drug's hydrophilicity or hydrophobicity, within nanoparticles in the scaffolding; (2) independently control the release of each drug from a nanoparticle whose composition is designed for that specific drug; (3) control the distribution of the different drugs within the scaffold, by the assembly sequence; and (4) be able to be introduced into a patient by injection followed by controlled self-assembly of the scaffold in situ. These abilities provide this type of assembled fiber system with significant advantages over electrospun fiber scaffolding as well as peptide-only scaffolding.

Here we illustrate the self-assembly behavior and versatility of peptide-functionalized nanoparticles using different particle sizes that can alter scaffold porosity and affect mechanical stability, and also show the ability to load and independently control the simultaneous release of three drugs within a single scaffold. We used two hydrophobic model drugs (4', 5'-dibromofluorecein as moderately hydrophobic and fluorescein as somewhat more hydrophobic), and a slightly hydrophilic model drug (nitrofurazone). The assembly sequence of the self-assembled nanoparticles, having already been loaded with drugs, is illustrated in Figure 5.1.

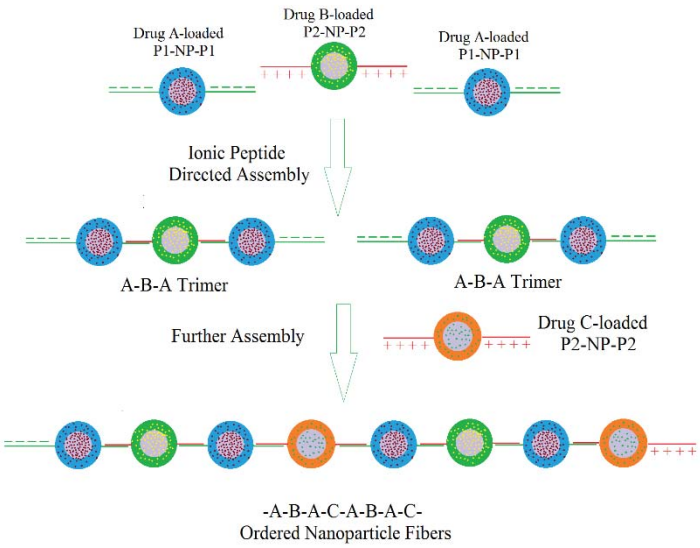


Figure 5.1 Illustration of the assembly of a 3-nanoparticle system

## 5.2 Experimental

### 5.2.1 Materials

The ionic complementary peptides (P1: H2N-TTTT-AEAEAEAE-amide and P2: H2N-TTTT-AKAKAKAK-amide) was described in previous work. 1-Vinyl-2-pyrrolidinone (VP) (≥99%), methyl methacrylate (MMA) (99%), 1,4-dioxane (99+%), 2,2′-azobisisobutyronitrile (AIBN) (98%), dimethyl formamide (DMF, 99.9%), phosphate buffered saline (Biotech) and model drugs of nitrofurazone (NF), 4',5'-dibromofluorescein (DBF) and fluorescein (FL) were purchased from Sigma-Aldrich. Ethyl alcohol (200 proof, anhydrous) was from PHARMCO-AAPER, and diethyl ether (anhydrous) and dimethyl sulfoxide (DMSO) were from Mallinckrodt Baker Inc. (Phillipsburg, USA). VP was purified prior to use by passing through a neutral alumina column. MMA was distilled before use. All other reagents were used as received.

Ultrapure deionized water (>17.6 MΩ-cm) was obtained from MEG-PURE SYSTEM (MP-190 LC).

### 5.2.2 Synthesis of Amphiphilic Triblock Copolymers

Amphiphilic triblock copolymers of PVP-b-PMMA-b-PVP, with reactive carboxylic acid terminals (HOOC-ABA-COOH), was synthesized by RAFT polymerization using S,S′-bis(α,α′-dimethylacetic acid) trithiocarbonate (BDAT) as a chain transfer agent (CTA) and 2,2′-azobisisobutyronitrile (AIBN) as the initiator, as described in previous work.[11] Briefly, the polymerization was done in two steps to build up the amphiphilic block copolymer. In the first step the hydrophilic block (PVP) was prepared in dioxane at 70°C (24 h under nitrogen atmosphere) using the following ratio of reagents: $[M]_o$: $[BDAT]_o$: $[AIBN]_o$=1000:5:1. The product was precipitated in cool diethyl ether to obtain the PVP solids. The precipitation was repeated 3 times to remove any unreacted monomer. The polymer containing the hydrophilic block was vacuum-dried at 50 °C for 12 h. In the second step, the hydrophilic polymer was used as a macro-CTA to copolymerize with MMA in a dioxane/DMF (4:1 v/v) solvent mixture with additional AIBN added (0.0012 g). The reaction was continued at 70 °C (48 h) under nitrogen atmosphere to obtain the amphiphilic triblock copolymer. The as-made copolymer solution was purified by precipitating in cool diethyl ether 3 times to remove unreacted residues and vacuum-dried at 50 °C for 12 h. The reactant ratios and the theoretical data of triblock copolymer were shown in Table 5.1.

Table 5.1 Reactant ratios and theoretical data of triblock copolymer

| **Macro-CTA** | **$[M]_o:[CTA]_o:[I]_o$** | **$X_N$** |
|---|---|---|
| PVP | 1000:5:1 | 200 |
| **Copolymer** | **Mass Ratio** $_{(Macro\text{-}CTA)_o:(MMA)_o}$ | **$X_N/X_M$** |
| PVP-b-6PMMA-b-PVP | 1:3 | 200/66 6 |

Theoretical molecule: $PVP_{100}$-$PMMA_{666}$-$PVP_{100}$

### 5.2.3 Coupling Reaction of Copolymer with Peptide (P1 and P2)

The synthesized peptides (P1 and P2) were coupled with the desired amphiphilic copolymer to form peptide-copolymer conjugates. The coupling reaction was performed between the carboxylic acid terminals of the desired polymer and the amine terminal of the desired peptide using 2-(7-aza-1-H-benzotriazol-1-yl)-1,1,3,3-tetramethylaminium (HATU) as the coupling agent, as reported previously.[11] In this work the polymer molecular weight differs from that in the previous work, so the reactant quantities and ratios are slightly different that reported previously. The process for the PVP-b-12PMMA-b-PVP system is described as an example. The copolymer (1.0 g, ~1.6 x $10^{-5}$ mol) was dissolved in DIPEA/DMF (8.0 mL, 0.9 M DIPEA in DMF) at room temperature in a 25 mL three neck round bottom flask with magnetic stirring. The reaction solution was degassed for 15 min with nitrogen gas and then HATU (0.012 g, 3.2 x $10^{-5}$ mol) was added to activate the carboxylic acid groups. P1 (0.10 g, 8.2 x $10^{-5}$ mol) was pre-dissolved in DMF (5.0 mL) in a glass vial, and then transferred into the activated copolymer solution via syringe. The reaction was continued for 45 min at room

temperature with magnetic stirring and nitrogen gas bubbling through the solution. P2 was similarly coupled with a second batch of copolymer. The peptide-copolymer conjugate was precipitated in cool diethyl ether and centrifuged to remove unreacted chemicals. The precipitates were washed 3 times to obtain purified conjugate solids, and dried under reduced pressure for 12 h at 50 °C before storing in a sealed vessel in the refrigerator at 4 ˚C.

### 5.2.4 Self-Assembly Study of Peptide-Copolymer Conjugates in Aqueous Solution

All peptide-copolymer conjugates nanoparticles were first self-assembled in separate aqueous solutions to form the peptide-functionalized nanoparticles designated P1-NP-P1 and P2-NP-P2. The P1-NP-P1 and P2-NP-P2 nanoparticles, bearing complementary peptides were then combined to further assemble into 1D nanoparticle fibers and eventually formed 3D scaffolds as directed by the ionic complementary assembly between P1 and P2.

The assembly of the nanoparticles into nanoparticle fibers was accomplished in three steps as follows. First the P1-copolymer conjugates (20 mg) were dissolved in DMSO (2 mL) to give a clear precursor solution, and this precursor solution was slowly injected (0.4 mL/min) into weakly basic deionized water (10 mL, pH 9.0, adjusted by 1 M NaOH solution), using a 31 G syringe, while being stirred at 700 rpm by a magnetic stirrer. This resulted in the first level of assembly to give the P1-NP-P1 suspension. After completing the injection of the precursor solution, the magnetic stirring was continued for 30 min and then sonicated 3 minutes to form a stable peptide-nanoparticle suspension. Separately, in

the second step, the P2-copolymer conjugates were dissolved in DMSO to form another precursor solution and then injected into weak acidic D.I. $H_2O$ (10 mL, pH 5.4, adjusted by 1 M HCl) and also sonicated for 3 min to give a P2-NP-P2 suspension.

The individual nanoparticle suspensions were formed in basic (pH 9.0) and acidic (pH 5.4) D.I. $H_2O$ to better ionize the carboxylic acid side groups of P1 and amine side groups of P2 to bear negative and positive charges respectively. This ensures that the newly formed nanoparticles bear complementary peptides that are also self-repulsive. However we can also accomplish assembly at neutral pH or PBS (pH 7.4).[11] The typical yield for these scaffold systems ranges from 90-95%.

### 5.2.5 Controlled Release Testing

The selected peptide-copolymer conjugate is dissolved in DMSO together with the desired drug to give a precursor solution. For example, for a two-drug scaffold, we prepared NF/P1-PVP-b-6PMMA-b-PVP-P1 (38 mg + 5.0 wt. % NF) in 1.5 mL DMSO and DBF/P2-PVP-b-6PMMA-b-PVP-P2 (38 mg + 5.0 wt. % DBF) in 1.5 mL DMSO. The NF/P1-copolymer precursor solution was then slowly injected into deionized water (10 mL) to give an NF-loaded core-shell nanoparticle suspension (NF-loaded P1-NP-P1 suspension). A DBF/P2-copolymer precursor solution was similarly prepared and injected into deionized water (10 mL) to give a DBF-loaded self-assembled core-shell nanoparticle suspension (DBF-loaded P2-NP-P2). The DBF-loaded P2-NP-P2 suspension was then slowly injected (23 G syringe) into the NF-loaded P1-NP-P1 suspension with gentle magnetic stirring at 400 rpm for 1h to give a uniform mixture, which was then allowed to self-assemble into a 3D nanoparticle scaffold with magnetic stirring at 100 rpm and settled to the bottom of the vial.

The nanoparticle scaffolds were collected by centrifugation at 4000 rpm for 20 min to isolate any NF and DBF that were not captured by the nanoparticles or just loosely adsorbed onto the nanoparticle surfaces. They were then washed with fresh D.I. $H_2O$ (2.0 mL each time). The centrifugation and washing process were repeated two additional times. All supernatant fractions were combined to collect all uncaptured NF and DBF, so that the actual loading (wt %) of NF and DBF in nanoparticles was calculated based on Equation 5.1. The washed scaffold solids were then used to set up the controlled release study.

$$Actual \quad wt.\% = \frac{W_{\text{int}ial \ \ drug} - W_{uncaptured \ \ drug}}{W_{drug-loaded \ \ nanopartite}} \times 100\%$$

Equation 5.1 Actual loading efficiency (wt. %)

The three drug loading process was similarly accomplished, but in this case, the ratio of P2-NP-P2 (DBF loaded) to P1-NP-P1 (NF loaded) to P2-NP-P2 (FL loaded) was set up at 1:2:1 wt. /wt. to achieve the loading of three drugs into a single scaffold. Briefly, DBF/P2-PVP-b-6PMMA-b-PVP-P2 (19 mg + 5.0 wt.% DBF)/DMSO (0.75mL) solution, NF/P1-PVP-b-6PMMA-b-PVP-P1 (38 mg + 5.0 wt.% NF)/DMSO (1.5mL) solution and FL/P2-PVP-b-6PMMA-b-PVP-P2 (19 mg + 5.0 wt.% FL)/DMSO (0.75mL) solution were prepared and each was separately injected into D.I. $H_2O$ (5 mL, 10 mL and 5 mL correspondingly) to give the three model drug-loaded nanoparticle suspensions. The DBF-loaded P2-NP-P2 suspension was slowly injected into the NF-loaded P1-NP-P1 suspension with gentle magnetic stirring at 400 rpm for 1h to give a uniform mixture. Due to the ratio of P1-NP-P1 to P2-NP-P2 was 2:1, at this stage the self-assembled nanoparticle fibers will favor “nanoparticle trimers” terminated with P1 on both ends.

Then, the third drug-loaded nanoparticle suspension (FL-loaded P2-NP-P2 suspension) was slowly injected into the above P1-terminated nanoparticle fiber suspension, restoring 'peptide stoichiometry', and gentle magnetic stirring was continued to advance the assembly and give the triple drug loaded scaffolding.

The triple drug-loaded scaffold solids were isolated and washed with fresh D.I. $H_2O$ (2.0 mL each time, washing 2 additional times to collect all free model drugs in supernatant. Again the actual drug loading (wt. %) was calculated according to Equation 5.1 after the uncaptured drugs were quantified by UV spectrometry.

Both the two and three-drug loaded scaffold solids were set up for controlled release tests over 24 h at 37 $^{o}$C in PBS media. The scaffold solids were re-dispersed in PBS (5.0 mL) and then transferred into dialysis tubing, which was then immersed into 100 mL of PBS buffer in a beaker at 37 $^{o}$C. The beaker with dialysis tubing was sealed to keep total mass constant during controlled release tests. If solvent loss was detected, D.I. $H_2O$ was added to keep total mass consistent. At each time interval, a 1.5 mL aliquot of PBS solution with released drug was removed from the beaker and the same volume of fresh media was added to keep the total volume at 100 mL. This procedure was repeated until the controlled release test was completed.

## 5.3 Results and Discussions

### 5.3.1 Proof of self-assembling by DLS

The hydrodynamic diameter of the system after different levels of nanoparticle assembly is shown in Figure 5.2. After initial assembly to give individual peptide-functionalized

nanoparticles the two nanoparticles have a similar size (Figure 5.2 a and b) at 174 nm and 167 nm. After 1 h the nanoparticle size prepared by combining a 2:1 ratio of P1-NP-P1 and P2-NP-P2 possessed a hydrodynamic diameter measured by DLS that was consistent with a "trimer", assuming a roughly "linear" conformation. After 20 h the size (Figure 5.2c and Table 5.2) was not significantly different indicating stoichiometric control, consistent with a step-growth process. We then restored stoichiometry to this system by adding the requisite equivalents of P2-functionalized nanoparticles, and re-measured the size again after 1 h and 20 h of reaction.

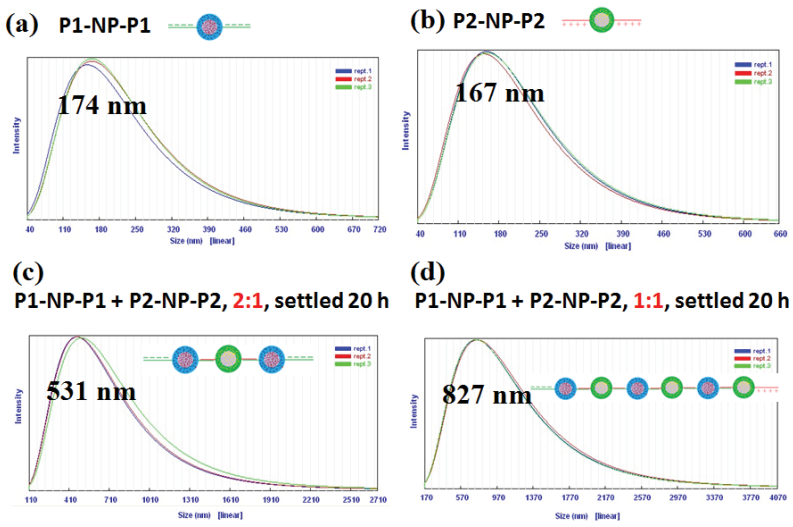


Figure 5.2 DLS test showing the hydrodynamic diameter resulting from different stages of self-assembly. (a) and (b) Hydrodynamic diameter of the individual nanoparticles P1-NP-P1 and P2-NP-P2; (c) Hydrodynamic diameter of an assembled nanoparticle trimer form by mixing P1-NP-P1 with P2-NP-P2 at 2:1 ratio after 20 h of assembly time; (d) Hydrodynamic diameter of an assembled nanoparticle fiber by mixing P1-NP-P1 with P2-NP-P2 at 1:1 ratio after 20 h of assembly time.

We saw additional growth after 1 h and still further growth after 20 h (Table 5.2). While the chain conformation is not expected to approximate linear as the assembly sequence gets longer, here we approximate the chain length of five nanoparticles ($X_N$ ~5, using a nanoparticle diameter of 170 nm and assuming a linear chain), which suggests that significant chain extension has not occurred. The slow growth in size is consistent with step-growth processes, but here we attribute the low chain extension to be primarily due to the dilute conditions required for a DLS test. However, the importance of perfect stoichiometry to achieving a high degree of assembly cannot be ignored. Either slow growth or any error in peptide stoichiometry, or some combination of both, will result in a much shorter nanoparticle chain. Here, we know that the system was dilute that is a contributor to the small chain size. On the other hand, the non-uniform copolymer chain length and possibly different coupling reaction between P1 and P2 with the copolymer will give variables for P1- and P2-copolymer conjugates, leading to deviation of stoichiometric control between P1- and P2- functionalized nanoparticles. This is considered as another contributor to the low chain growth. So, the nanoparticle assembly process requires more exploration by adjusting the ratio between P1- and P2-functionalized nanoparticles to achieve an optimized condition for a perfect stoichiometric system to follow step growth principle to give more effective nanoparticle chain growth.

Table 5.2 Hydrodynamic diameter of a scaffold "Trimer" and the full scaffold after restoration of peptide-functionalized nanoparticle stoichiometry.

| Samples | Assembled NP name | Scaffold Assembly time (h) | NP Size (nm) |
|---|---|---|---|
| P1-PVP-b-6PMMA-b-PVP-P1 | P1-NP-P1 | -- | 174±4 |
| P2-PVP-b-6PMMA-b-PVP-P2 | P2-NP-P2 | -- | 167±2 |
| P1-NP-P1 : P2-NP-P2 Ratio 2:1 | NP "Trimer" | 1 | 518±22 |
| | | 20 | 531±19 |
| P1-NP-P1 : P2-NP-P2 Ratio 1:1 | NP fiber | 1 | 620±10 |
| | | 20 | 827±9 |

## 5.3.2 Drug delivery calculation

Three model drugs of nitrofurazone (NF, $\lambda_{max}$=375nm), 4′,5′-Dibromofluorescein (DBF, $\lambda_{max}$=502nm) and Fluorescein (FL, $\lambda_{max}$=490nm) were incorporated into assembled nanoparticle scaffolds to test the multiple drug loading ability and control over release rate of each loaded drug. The chemical structures of the three molecules are shown in Figure 5.3. Among these three drugs, NF is considered a slightly hydrophilic model drug (more soluble in PBS than DBF and FL), and both DBF and FL are moderately hydrophobic model drugs, but DBF contains two bromide groups, and thus is more polar than FL.

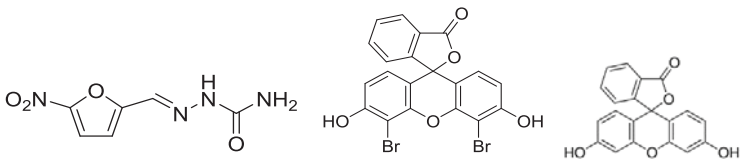


Figure 5.3 Chemical structure of the model drugs. (a) Nitrofurazone (NF), (b) 4′,5′-Dibromofluorescein (DBF) and (c) Fluorescein (FL).

Measurement of the simultaneous release of multiple drugs from a single scaffold is not a trivial process, since many drugs will have some absorption at the same wavelengths. To try to find the suitable wavelengths for measuring simultaneous drug release several sets of standard curves were made to determine the quantity of drugs released from the scaffolds. Figure 5.4 shows the three standard curves of NF, DBF and FL in PBS buffer (pH 7.4) with concentration ranging from 0 to 0.5 mg/100mL, and measuring the drug at different wavelengths.

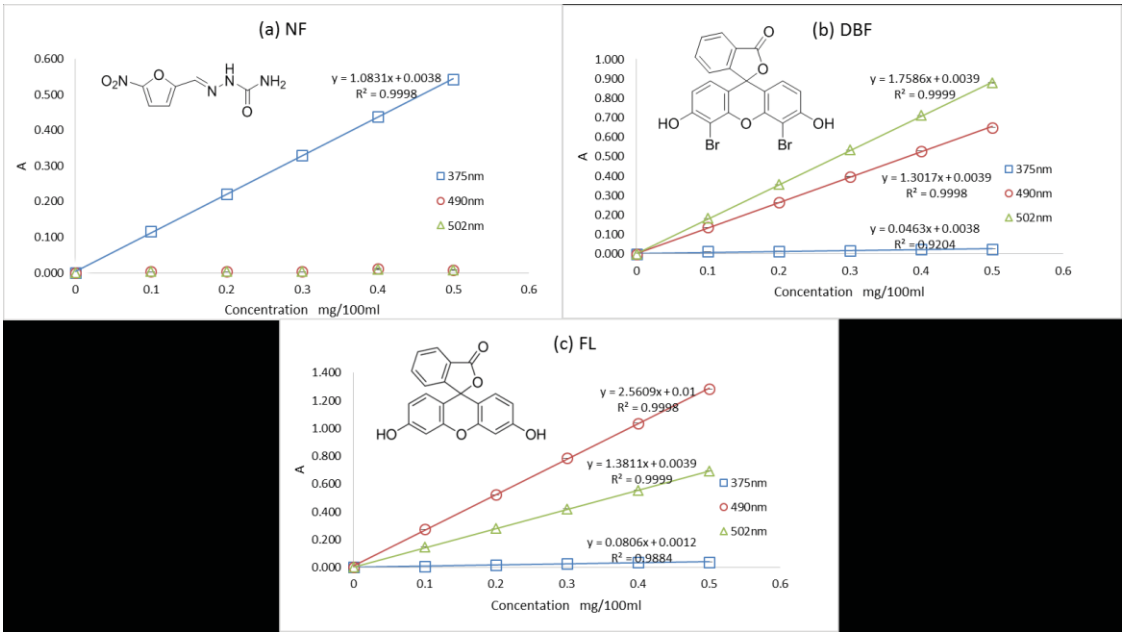


Figure 5.4 Standard curves of NF, DBF and FL used for the quantitative determination of the multiple released drugs (Test done in PBS).

A two drug-loaded scaffold was prepared for the simultaneous controlled release of NF and DBF. The quantity of released drug was calculated using the equations given below, where $X_1$ is the concentration of the released NF at each time interval and $X_2$ is the concentration of the released DBF. $A_1$ is the absorption of $\lambda$ =375nm and $A_3$ is the

absorption of λ=502nm. The absorption of each λ gives the sum of the absorption of each single model drug. Based on this, we can get two equations:

$\lambda$=375nm, $A_1$=1.083 $X_1$ + 0.046 $X_2$ + 0.008

$\lambda$=502nm, $A_3$=1.759 $X_2$ + 0.009

After solving this equations, we can get the concentration for each model drug:

$X_1 = [A_1 - 0.008 - 0.046 X_2] / 1.083$

Equation 5.2a The concentration calculation of model drug (NF)

$X_2 = (A_3 - 0.009) / 1.759$

Equation 5.2b The concentration calculation of model drug (DBF)

NF, DBF and FL model drugs were used in the triple drug-loaded scaffold for controlled release testing. We calculate the concentration of each drug in the drug-loaded scaffold using the equations at three different wavelengths. $X_1$ is the concentration of the released NF at each time interval, $X_2$ is the concentration of the released DBF and $X_3$ is the concentration of the released FL. $A_1$ is the absorption of $\lambda$=375nm, $A_2$ is the absorption of $\lambda$=490nm and $A_3$ is the absorption of $\lambda$=502nm. According to the standard curves, we can get these equations at each wavelength:

$\lambda$=375nm, $A_1$=1.083 $X_1$ + 0.046 $X_2$ + 0.081 $X_3$ + 0.009

$\lambda$=490nm, $A_2$=1.302 $X_2$ + 2.561 $X_3$ + 0.019

$\lambda$=502nm, $A_3$=1.759 $X_2$ + 1.381 $X_3$ + 0.013

Solving these equations, the concentration for each component is:

$X_1 = (A_1 - 0.046 X_2 - 0.081 X_3 - 0.009) / 1.083$

Equation 5.3a The concentration calculation of model drug (NF)

$X_2 = (A_2 – 2.561\ X_3 – 0.019) / 1.302$

Equation 5.3b The concentration calculation of model drug (DBF)

$X_3 = (1.351A_2 – A_3 - 0.013) / 2.079$

Equation 5.3c The concentration calculation of model drug (FL)

All samples from the release data were diluted (sample: PBS = 1:2) for testing the absorption by UV-*vis*. Each data point shown is the average of three tests.

### 5.3.3 Release data discussions

The quantity of each drug released from the scaffold was measured for the two- and three-drug system at selected time intervals as shown in Tables 4.3 and 4.4.

Table 5.3 Released quantity of model drugs from the two-drug scaffold (in 100ml PBS buffer).

| Time | $X_1$/mg | $X_2$/mg |
|---|---|---|
| 0 | 0.000 | 0.000 |
| 0.5 | 0.026 ±0.007 | 0.094 ±0.002 |
| 1 | 0.043 ±0.004 | 0.194 ±0.003 |
| 2 | 0.084 ±0.008 | 0.410 ±0.021 |
| 3 | 0.096 ±0.007 | 0.565 ±0.005 |
| 6 | 0.125 ±0.006 | 0.900 ±0.070 |
| 12 | 0.122 ±0.006 | 1.080 ±0.120 |
| 24 | 0.114 ±0.009 | 1.140 ±0.076 |
| Uncaptured | 1.540 ±0.109 | 0.123 ±0.016 |

Table 5.4 Quantity of each model drug released from the three-drug scaffold (in 100 mL PBS buffer).

| Time/h | X1/mg | X2/mg | X3/mg |
|---|---|---|---|
| 0 | 0.000 | 0.000 | 0.000 |
| 0.5 | 0.026±0.011 | 0.054±0.011 | 0.095±0.013 |
| 1 | 0.057±0.014 | 0.128±0.028 | 0.208±0.019 |
| 2 | 0.086±0.012 | 0.241±0.050 | 0.376±0.025 |
| 3 | 0.102±0.008 | 0.333±0.056 | 0.500±0.039 |
| 6 | 0.122±0.011 | 0.487±0.022 | 0.706±0.118 |
| 12 | 0.120±0.012 | 0.561±0.027 | 0.820±0.062 |
| 24 | 0.116±0.011 | 0.607±0.031 | 0.911±0.014 |
| Uncaptured | 1.789±0.014 | 0.058±0.000 | 0.075±0.002 |

Any uncaptured drug in the supernatant was similarly determined by the above quantitative analysis method. The results are also shown in Table 5.3 and 4.4, labeled as Uncaptured. Using the uncaptured drug quantities, the loading efficiency of each drug and its actual loading (wt. %) were calculated by Equation 5.1.

In sum, the quantity of each drug that was not captured during nanoparticle preparation, and the quantity of released drug at each time interval, were determined by UV-*vis* spectrometry using calibration curves prepared from standard solutions of NF, DBF and FL. The drug concentration ranged from 0.001 mg/mL to 0.005 mg/mL, and was measured against the standard curves using Beer's Law equations (Figure 5.4) and Equation 5.2a-b and 4.3a-c. After the calculating by Equation 5.1, Table 5.5 gives the loading efficiency and actual loading (wt. %) of the model drugs in both the two and three drug loaded scaffolds.

Table 5.5 Loading efficiency of model drugs in two-drug and three-drug nanoparticle scaffolds.

| Scaffold | Model Drug | NP Pair | Theo. Loading wt. % | Act. Loading wt.% | Loading eff. % |
|---|---|---|---|---|---|
| 2 Drug | NF | P1-NP-P1 | 5.0 | 1.2 | 23 |
| | DBF | P2-NP-P2 | 5.0 | 4.7 | 93.8 |
| | DBF | P2-NP-P2 | 5.0 | 4.7 | 94.2 |
| 3 Drug | NF | P1-NP-P1 | 5.0 | 0.53 | 10.6 |
| | FL | P2-NP-P2 | 5.0 | 4.6 | 92.5 |

One of the major advantages of the peptide-assisted nanoparticle assembly is to impart self-assembled polymeric nanoparticle scaffolds with the ability to load desired quantities of more than one type of drugs into a single scaffold, without hindering the scaffold assembly, while still retaining control over the release rate of each drug. We tested a scaffolding system with up to three model drugs and confirmed the incorporation and sustained release of each drug. Prior work proved that we could assemble scaffolds from nanoparticles with different composition of the nanoparticles, incorporate drugs and proteins into the nanoparticles and manipulate their release rates.[11] Therefore this proof-of-concept study focused only on the simultaneous release of multiple drugs, so the overall nanoparticle composition was held constant.

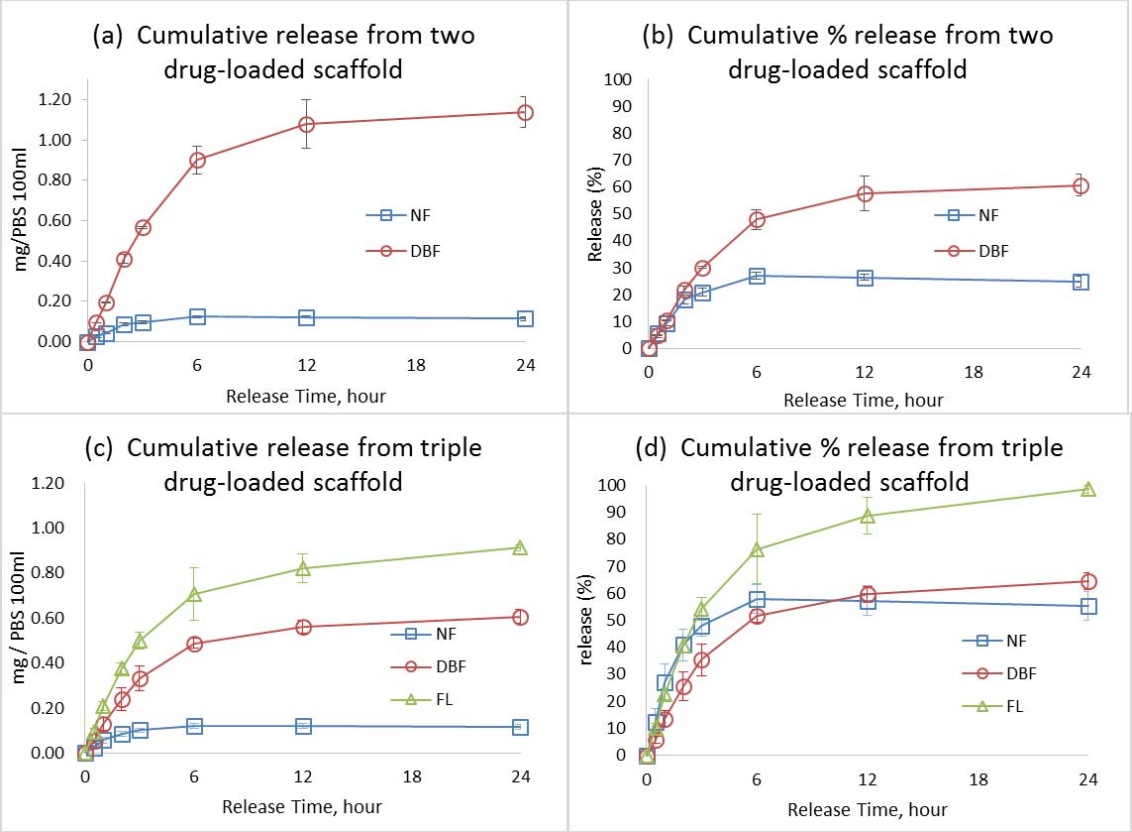


Figure 5.5 Cumulative release of model drugs from multiple drug-loaded self-assembled nanoparticle scaffolds over 24 h. (a) NF and DBF release from a two drug-loaded scaffold, mg per 100 mL PBS buffer; (b) wt.% cumulative release from two drug-loaded scaffold. (c) NF, DBF and FL release from a triple drug-loaded scaffold, mg per 100 mL PBS buffer; (d) wt.% cumulative release from triple drug-loaded scaffold.

The two-drug and three-drug loaded scaffolds were prepared as described in experimental section. Table 5.5 summarizes the theoretical loading (wt. %) of the model drugs (NF, DBF, FL) and their loading efficiency. When preparing the drug-loaded nanoparticle scaffolds, the nanoparticle assembly is based on an assumption that the individual nanoparticles (P1-NP-P1 and P2-NP-P2) possess approximately same mass which are

assembled from P1-PVP-b-6PMMA-b-PVP-P1 and P2-PVP-b-6PMMA-b-PVP-P2, so that the nanoparticle end functional group numbers of P1 and P2 for nanoparticle chain extension through step growth principle can be controlled by measuring the nanoparticle mass to give stoichiometric control. But actually, owing to the presence of polydispersity of the as-made block copolymer, the inconsistent mass of the individual nanoparticles is unavoidable, so it is required to further optimize the mass ratio of P1-NP-P1 and P2-NP-P2 to achieve a better stoichiometric balance of P1 to P2 for more efficient control over nanoparticle chain growth if this system is applied to practical application. Here we preliminarily tested the abilities of multiple drug loading and controlled release over each drug. The controlled release profiles are shown in Figure 5.5.

The release profiles in Figure 5.5 show that the model drugs undergo a burst release in the first 6 h, followed by a stable release, a typical diffusion controlled release. Analysis of the cumulative % release along with the data in Table 5.5, suggest that the release rates of the model drugs have a complex dependency on several factors. The quantity of drug loaded into the scaffold is the major factor influencing the release rate and the amount of drug released. This is evidenced by the fact that the moderately hydrophobic model drugs possess a higher loading efficiency (DBF: 93.8 to 94.2 % and FL: 92.5 %) and show faster release rates than the slightly hydrophilic drug (NF), which possessed a low loading efficiency of 10.6 % and 23 %. This result is explained by the higher loading of the drugs producing a greater concentration gradient between the nanodevices and their surrounding environment (here is PBS media), driving the drug diffusion into the media in a faster rate. And also higher loading quantity leads to a more porous structure of the

nanoparticles, which is considered to increase the channels for both aqueous penetration and drug release. Such phenomena are also seen elsewhere.[12]

In principle, hydrophilic NF is more easily released into PBS media due to its higher solubility than that of moderately hydrophobic DBF, but Figure 5.5a shows only 26.3 wt% of NF released versus 58.2 wt% of DBF over 24 h. This result implies a second important factor that also influence drug release rate, the molecular interaction between drug molecules and polymer matrix. This is evidenced by NF release behavior from the two drug-loaded and triple drug-loaded scaffolds (Figure 5.5a and c). As Table 5.5 shows, the actual loading wt% of NF in the two drug-loaded scaffold is more than two times as in the triple drug-loaded one (1.2 wt% versus 0.53 wt%), where the nanoparticle mass for NF-loading is same in both scaffolds (see experimental section), but controlled release test shows that the NF cumulative release quantity is remained constant (0.11 ± 0.01 mg) over 24 h (Table 5.3 and 4.4), though the wt% cumulative release of NF is doubled due to the difference of the initial loading quantity (Figure 5.5b, d). This means the interaction of NF molecules with polymeric matrix, especially with hydrophilic shell (PVP shell), dominates the release rate (showing constant releasing behavior), but such interaction did not enhance the loading efficiency of NF in the nanoparticle scaffolds.

According to the chemical structure of the model drugs (Figure 5.3), the moderately hydrophobic model drugs (DBF and FL) possessed higher loading efficiency (92.5 % to 94.2 %) because they were more easily incorporated into the hydrophobic domains (PMMA core) and also could effectively distribute into the hydrophilic shell (PVP shell) via polar-polar interaction due to both molecules possessing certain amount of polar

functional groups (i.e. OH and C=O). This can be seen from the burst release behavior of both model drugs, followed by a stable release (Figure 5.5a and c). However, it is interesting to note that FL was released by 94.3 % over 24 h while DBF showed much lower release rate (58.2 % in Figure 5.5b and 61.7 % in Figure 5.5d). Again, this result supports that the molecular interaction plays significant role on release rate. The only structural difference between DBF and FL is the two bromide groups on DBF (Figure 5.3), which is considered to increase the molecular polarity and thus enhance the molecular interaction with polymeric matrix. Such enhanced polarity will also increase its solubility in PBS buffer, but it is not dominant for DBF release rate. So this means it is a competitive process of solubility and molecular interaction with polymer matrix to influence the release rate of a drug in a core-shell nanoparticle. Which one is dominant depends on the drug property and nanoparticle composition.

The release rates of the drugs from the scaffolds tested here show that there are several, complex, factors influencing their release. Gaining a more complete understanding of these complex factors influencing release will allow a scaffold designer to efficiently tailor the release of drugs from core-shell nanoparticle scaffolds. Besides the obvious variables such as drug loading quantity and choice of a nanoparticle composition suitable for each drug (since release is influenced by drug solubility and molecular interaction with the polymers), other variables include core-shell ratio and nanoparticle size. Yet additional variables worth testing in future include the porosity of the scaffold, the ability to combine different size nanoparticles within a single scaffold system and/or different compositions of nanoparticles that contain the desired drug(s).

## 5.4 Conclusion

A novel self-assembled fibrous nanoparticle scaffolding system was demonstrated that employs peptide-functionalized polymeric nanoparticles that self-assemble into continuous 'nanoparticle-fibers'. This type of nanoparticle scaffold combines the advantages of nanoparticles' abilities to contain and control the release of active ingredients (demonstrated here with model hydrophobic and hydrophilic drugs) along with the ability of peptides to assemble into controlled 1D, 2D, and 3D structures. This versatile system allows the simultaneous incorporation of multiple drugs, which, when properly controlled, gives substantial ability to design a scaffold with the desired quantity of a drug or other active agent, to tailor the release rate of that active agent, and allows control over how these nanoparticles are distributed within a scaffolding system. The assembly process is step growth, and so treatment of each nanoparticle as if it were a monomer should allow all the same control over number average degree of polymerization and sequence or block length control according to the rules of step growth processes as outlined by Wallace Carothers. The versatility of this fundamental technique can be expanded to other materials or coupling techniques. The materials and peptides used here were not cytotoxic to fibroblast cells, but that the surfaces require additional modification to improve cell adhesion if it is desired, possibly by immobilizing cell adhesion ligands on the polymeric nanoparticle surfaces. In this work we also noted that the designer peptide self-assembly is easily converted into an amorphous aggregate after washing with aqueous solution, which was due to an overly water-soluble peptide structure, so alternative designer peptides with less solubility might promote a lower critical concentration to form stable self-assembled peptide nanofibers with enhanced

mechanical strength while longer and more mobile peptide motifs might yield longer nanoparticle fibers. In principle this approach can be further advanced to give both temporal and spatial control over the distribution of the drug-containing nanoparticles to allow blocks of nanoparticles with a given drug, or nanoparticle gradients to be formed in the scaffolds, while also yielding an injectable system.

# Chapter 6 Polymer Modification of Fish Scale and their Nano-mechanical Properties[c]

## 6.1 Introduction

Throughout history humans have used and benefitted from nature's materials, benefitting from the properties their hierarchical structure gives them (e.g. hides, feathers, wood), and then learning to separate component parts (e.g. gelatins, keratin, cellulose) for other uses. More recently we have sought to study ever more complicated natural designs in natural materials and to replicate properties inherent to those designs with other, often synthetic, materials, giving rise to the science of biomimetics. Perhaps the best known, and most advanced example of this, is learning to produce superhydrophobic and self-cleaning surfaces from the study of lotus leaves.[1] In recent years certain types of fish scales have elicited great interest because of their exceptional properties.[2] The two most studied scale structures are those of the arapaima[3] and alligator gar[4], whose scales have been described as dermal armor.[5]

Fish scales are designed to protect the body from predators or other damage, and to reduce friction as they move through water, but even though all scales serve these functions there can be significant differences in scale composition, design, shape, and size.[4, 6] Of the four major categories of scales (i.e. cycloid scales found on salmon and carp, ctenoid scales found on fishes such as bass, placoid scales found on sharks and rays, and ganoid scales found on sturgeon and gars), the most studied from the perspective of

[c] The material contained in this chapter was previously has been submitted to the *Journal of Applied Polymer Science*.

materials or polymer scientists are the ganoid scales of alligator gar (*Atractosteus spatula)*[4] and the ctenoid scales of the arapaima *(Arapaima gigas)*[3].

Most of the materials-focused research on fish scales has studied the hierarchical design of individual scales[7], the mechanical properties of individual scales[7b, 8], mathematical studies to simulate the mechanical properties[9] and the arrangement of scales to see how they work together as an assembly[10].

The objective of those studies is to gain a fundamental understanding of how scales achieve their exceptional properties, and presumably to be able to apply that understanding to reproduce and exceed those properties using synthetic materials, e.g. for body armor or other armors. That is why the bony scales of the alligator gar are the most studied.[4, 9] However, while the design of alligator gar scales is important from a fundamental perspective, it is not a food fish. So its scales will never be an abundant waste resource.

The ctenoid scale of the arapaima gigas is the other well-studied fish scale. These scales have been studied because they allow this South American fish to resist predation by the piranha.[5, 11] This scale has two main layers. The top layer is a calcium deficient hydroxyapatite (HAP) layer, also called the biomineral layer, because it contains organic components in addition to HAP. It has a similar composition to dentin.[3] The second layer is flexible and consists of smaller layers of alternating arrays of collagen fibers [12], with the layers arranged at 90˚ to one another. The overall thickness of the scales can vary, but the alternating collagen layers are ~50 μm thick. The collagen fibers in these stacked layers are ~1 μm, and these are made up of individual collagen fibrils of ~100 nm. The

collagen layer has many methods to dissipate energy without failure, include the ability for the individual 50 μm layers to slide past one another without damage. The arapaima is a food fish in South America, but it is also not an abundant resource and not a North American species. One study looked at the scales (ctenoid) of a North American food fish, the striped bass (*Morone saxatilis*).[11] Those researchers studied the toughness and failure modes of the scale and found that it resisted penetration more effectively than either polystyrene or polycarbonate.

With annual fish harvests estimated at ~140-176 million tonnes, the mass of waste scale, assuming it is just ~1 wt% of the fish, is still at least 1.4 million tonnes. Therefore scale waste is abundant but underutilized. When they are used industrially or in research the typical interest is in harvesting their components for individual use, i.e. HAP from the biomineral layer [6a, 8b] is harvested by high temperature alkaline treatment, and collagen is harvested using HCl to remove the biomineral layer followed by additional re-fabrication methodologies for subsequent biomedical uses.[13] The recovery of basic components from biowaste is valuable and consistent with a "bio-refinery" approach, but it also sacrifices all the properties built into the scale's hierarchical design.

Lignocellulosic materials are the most abundant biomass under investigation. Studies of this biomass and its uses include separation and chemical modification of components in a standard bio-refinery approach[14], but also size diminution of the lignocellulosic and surface modifications[15], and chemical and energy treatments to isolate cellulose nanocrystals[16] and nanofibrils[17]. Just as cellulosic materials are used in different forms and for with different modifications, fish scales may also offer a range of opportunities for use beyond simply extracting their basic components. Because of the hierarchical

design of fish scales, with the hard HAP biomineral surface and the tough collagen layer, there are numerous opportunities for selective physical and chemical modifications. On one surface and a hydroxyapatite (HAP) biomineral layer, allowing the selective manipulaton of structure and properties.

Our long-term interest in scales is to find uses for fish scale waste that can take advantage of their hierarchical structure. To that end we focus on an initial study of the cycloid scales of the lake whitefish (*Coregonus clupeaformis*), in the family of Salmonidae, which is an abundant food fish harvested throughout Canada and the northern United States. The material properties and potential value of scales of North American fish are almost never studied, with the exception of a study on the ctenoid scales of a bass[11]. In fact the material properties of cycloid scales seem to be almost unstudied, with only one paper found, used X-ray microscopy techniques, to study the collagen fiber structure of the cycloid scales of the red seabream (*Pagrus major*), harvested from the Sea of Japan.[18]

In this work we provide the first study of the nanomechanical properties of the relatively unstudied cycloid type of fish scale, and the first investigation of the ability to selectively chemically alter the different layers of the fish scale. It should be noted that we found one prior study that used scales as a support for $TiO_2$ nanoparticles for photocatalysts[19], but the chemical modification of fish scales is unstudied. The intention of this work is to show the potential to "build on" and benefit from the hierarchical design of scales rather than simply destroy the structure for its components. We hope that these studies will begin to point the way to applications for fish scales other than simply for isolatable components. Two of the most likely applications are as packaging additives and

composite reinforcements. As these applications, and many others, would likely benefit from modifying the interface, our initial studies looked at the effects of surface modifications on the spectroscopic and nanomechanical properties.

One prior study looked at unmodified scales as reinforcement in epoxy but found only modest improvement in tensile and flexural strengths.[20] Although they reported H-bonding between the epoxy and the scale this may have been insufficient for effective load transfer. Therefore, appropriate surface modification to enhance load transfer may yield better results.

## 6.2 Experimental

### 6.2.1 Materials

Whitefish scales (salmon family with cycloid scales) were used as received, harvested from fish taken from Lakes Superior, Huron and Michigan. Hydrochloric acid (HCl, concentrated), sodium hydroxide (NaOH), tetraethyl orthosilicate (TEOS), methyl methacrylate (MMA), oligo (ethylene glycol) methyl ether acrylate (OEGA, *Mn*=480g/mol), tert-butyl methacrylate (MA) and 2,2'-azoisobutyronitrile (AIBN) were purchased from Sigma-Aldrich. Clorox® was purchased from a local store. MMA and OEGA were purified by passing over a neutral aluminum oxide column to remove inhibitor. AIBN was recrystallized from ethanol. The other chemicals were used as received.

### 6.2.2 Fish scale modifications

#### 6.2.2.1 Cleaning fish scale surfaces (FS and FS-W)

As-received fish scales (FS) had been previously hand-washed in water. These scales were immersed in D.I. water (ca. 2 g fish scale in 20 mL D.I. water), and placed in an ultrasonic bath for 90 min at 42 kHz. These fish scales were decanted and rinsed three times with D.I. water, then air dried at room temperature, and used as unmodified control specimens. These scales are differentiated from the as-received FS scales by the designation FS-W.

#### 6.2.2.2 Fish scales treated by acid or base (FS-H and FS-OH)

Scales (2 g) were immersed in 20 mL of a 3.3% (w.t.%) HCl (aq) solution, then placed in an ultrasonic bath for 90 min at 42 kHz. The fish scales were decanted and rinsed three times with D.I. water. The fish scales were air dried at room temperature, and are designated as FS-H. The same procedure was used for scales that were immersed in a 3.3% (w.t.%) NaOH (aq) solution. These scales are designated FS-OH.

#### 6.2.2.3 Fish scales treated by Clorox® (FS-C)

Scales (FS) were immersed in a Clorox® solution (2 tsp per 1 gallon of water, active agent NaOCl) with stirring for 2.5 min. The scales were decanted, rinsed three times with water, and then air dried. These scales are designated FS-C.

#### 6.2.2.4 Fish scales modified with $SiO_2$ (FS- $SiO_2$ and FS- $SiO_2$-C)

Fish scales were immersed in TEOS and acidified water ($H^+$/Si = 8:1 mol:mol). The mixture was stirred at room temperature for 60 min. The scales were decanted, and the surface rinsed with D.I. water. The scales were then placed in a convection oven at 70$^o$C

and heated for 4 hours. These scales are designated as FS-$SiO_2$. For comparison, a second specimen was prepared in the same manner, except it was soaked in the same TEOS/HCl solution for only 30 min. It was also placed in a convection oven at 70$^{o}$C and heated for 4 hours. These scales are designated as FS-$SiO_2$-C.

Table 6.1 Summary of designations

| Scale Designation | Description of Scale Processing |
|---|---|
| FS | As-received scales. Hand washed in water |
| FS-W | FS scales with additional washing in water in an ultrasonic bath (40 kHz) 1.5 h. |
| FS-H | FS scales 3.3% (w.t.%) HCl(aq) solution in an ultrasonic bath (40 kHz) for 1.5 h. |
| FS-OH | FS scales 3.3% (w.t.%) NaOH(aq) solution in an ultrasonic bath (40 kHz) for 1.5 h. |
| FS-C | FS scales washed 2.5 min in Clorox® solution of 2tsp/gal water |
| FS-$SiO_2$-C | FS scales immersed in TEOS/HCl ($Si/H^+$ 8:1) for 0.5 h, followed by heat treatment (70 ˚C/4 h). |
| FS-$SiO_2$ | FS scales immersed in TEOS/HCl ($Si/H^+$ 8:1) for 1 h, followed by heat treatment (70 ˚C/4 h). |
| FS-PMMA | FS scales immersed for 1 h in monomer containing 1 w.t.% AIBN initiator, followed by heat treatment (70 ˚C/4 h). |
| FS-POEGA | FS scales immersed for 1 h in monomer containing 1 w.t.% AIBN initiator, followed by heat treatment (70 ˚C/4 h). |
| FS-PMA | FS scales immersed for 1 h in monomer containing 1 w.t.% AIBN initiator, followed by heat treatment (70 ˚C/4 h). |

#### 6.2.2.5 Polymer-modified fish scales (FS-PMMA, FS-POEGA, FS-PMA)

Fish scales were immersed in a selected monomer (MMA, OEGA, or MA) into which AIBN (1 w.t.%) had been dissolved. The fish scales in were stirred in the solution for 60

min. Excess monomer was decanted and then the scales were heated at 70 ˚C for 4 h in a convection oven. These scales are designated as FS-PMMA, FS-POEGA or FS-PMA. All the modified fish scales are shown in Table 6.1.

### 6.2.3 Preparation of Scale Cross Sections

Scales were embedded in an epoxy resin (EpoxiCure; Buehler, Lake Bluff, IL, USA) inside a cylindrical mold. The embedding resin was allowed to harden (24 hours, room temperature), and then removed from the mold. Each sample was polished using silicon-carbide paper under a continuous water jet to wash away abraded material. The specimens were polished until a cross section near the center of the scale was reached.

### 6.2.4 Modulus Using AFM

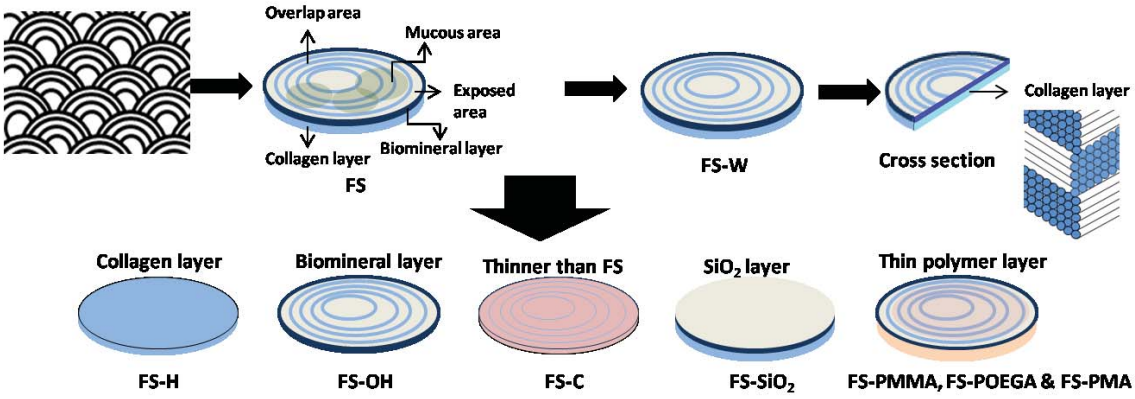


Figure 6.1 The diagram illustrates the different scale structures and modified scales. From left: an assembly of scales showing their overlap (top left); a representation of an individual scale before and after washing, and the alternating collagen layers. The second row represents the expected changes in structure resulting from chemical modifications.

All AFM experiments were carried out with a Dimension ICON AFM system (Bruker, USA). Peakforce Tapping mode was applied for all the nano-mechanical measurements

and topography imaging[21]. RTESPA silicon cantilevers (Bruker, USA) were selected. The spring constant was calibrated using Sader's methods[22] before each experiment, and the calibrated values were in the range from 32 to 49 N/m. In Figure 6.1, all the samples shown in the diagram will be tested by AFM. An additional background and explanation of the Derjaguin-Muller-Toropov (DMT) modulus is given in Appendix B.

## 6.3 Results and Discussion

### 6.3.1 Visualization and Analysis of Unmodified Scales: FS and FS-W

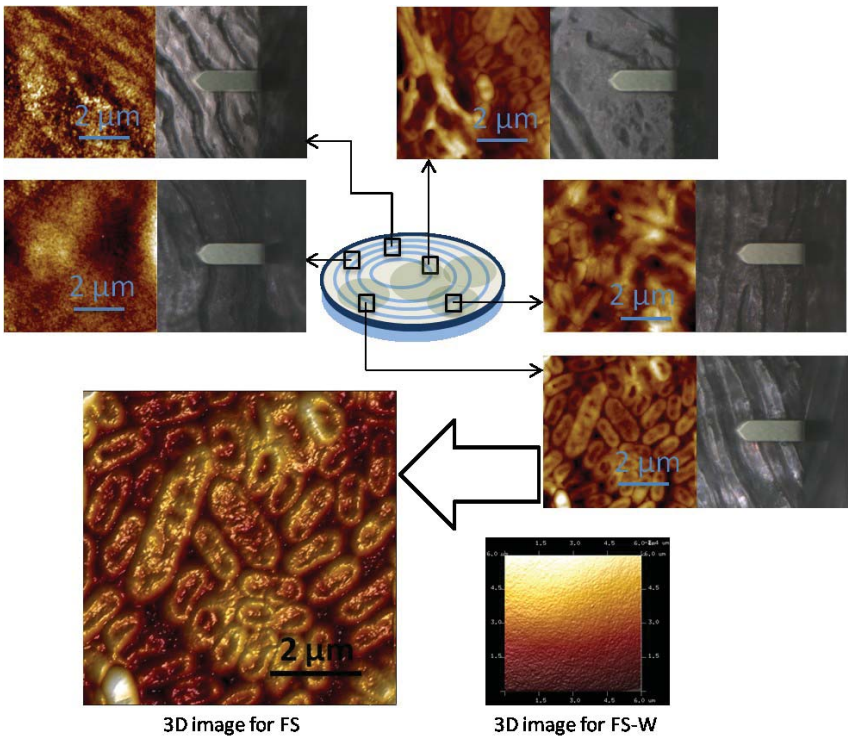


Figure 6.2 Surface of FS control scales imaged by optical microscope and AFM. The probe tip in the optical images has a 40 µm diameter. AFM images show a 6µmx6µm area. At bottom a topographical AFM image maps the roughness of the biomineral layer.

Cycloid fish scales have two types of layers: a biomineral (largely hydropxyapatite) upper surface layer and a collagen layer, consisting of alternating layers of rods at the interior and bottom surface of the scale. As Figure 6.2 shows, the biomineral surface is rough with regular ridge features of ~30–40 μm that alternate with depressions having a similar or slightly smaller diameter. These ridges are formed as the scales grow, like growth rings on a tree, so there is also a difference in scale thickness with the newer edges being thinner than the scale center. While these are the dominant features of the scales, there are other small variations in scale features depending on the scale's placement on the fish and with respect to other scales. The top of the scale that is exposed is generally rougher than the top of the scale that is overlapped by other scales. Most of these features are similar to those that have been described for other types of scales by others [5, 23]. However the scale surface that is covered by other scales shows unusual features that appear cell-like but seem to be too small for cells (≤ 1 μm). The topographical AFM image at the bottom of Figure 6.2 shows these features are oval to circular. Interestingly, these features are not observed in any scales other than the FS scales, including FS-W scales that were cleaned by ultrasonic washing. We suspect these features are associated with the cell's mucus layers, which possess the mucus/goblet cells [24], so these features might be dried remains of those cells. However, at this time we do not know what these features are.

Figure 6.3 shows a cross-section of an FS-W scale. The optical image shows multiple layers of collagen bundles with different orientations as evidenced by the light and dark grey striations. The AFM images confirm these collagen layers and the projecting collagen bundles made up of individual collagen rods are clearly seen at two different

angles in the AFM images. These alternate in a similar manner to those reported for the ctenoid scales of arapaima gigas[5]. From AFM1, the collagen is from one side to another and almost at the same surface. From AFM2, the collagen is from back to front, so the tops of the collagen rods are observed. This shows that the hierarchical structure was maintained after the ultrasonic washing and the collagen rod structure, which imparts toughness to the scales, appears undamaged.

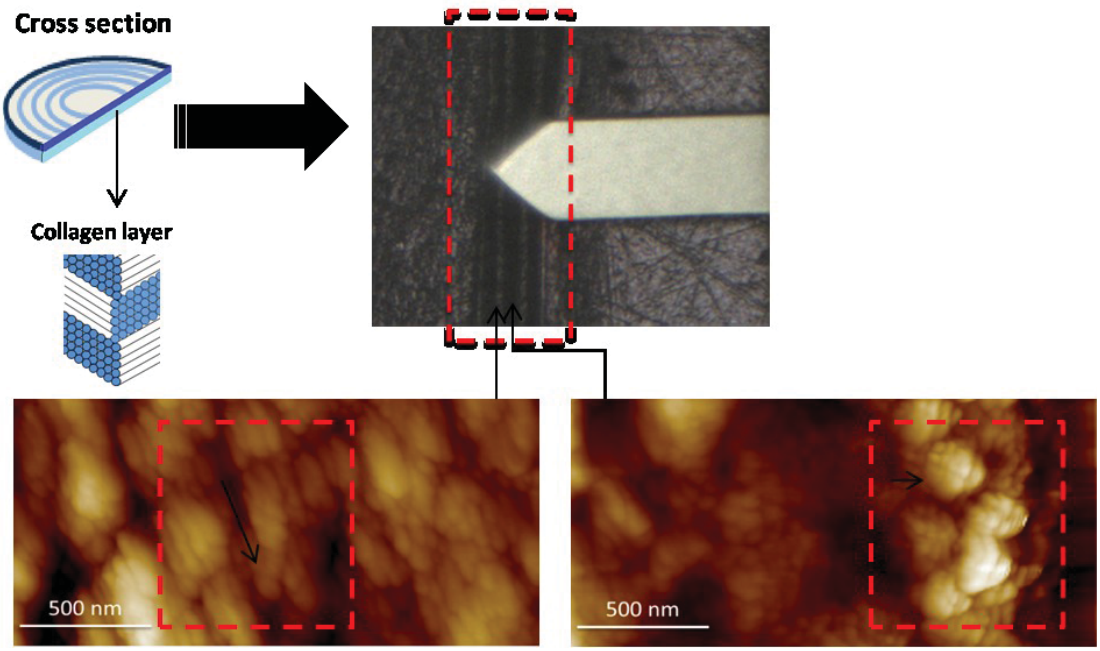


Figure 6.3 Cross-section of FS-W showing the different layers of collagen

## 6.3.2 Selectively degraded scales: FS-H, FS-OH and FS-C

### 5.3.2.1 Changes in composition and structure by FTIR

Before we could understand how our modifications were changing the two main domains of the scales we first needed to characterize the two main domains of the unmodified FS and FS-W scales. Because we wished to see if our modifications were preferential to the

biomineral or collagen layers of the scales, so that we might "build" on the existing hierarchical design of the scales, we analyzed the top and bottom surfaces of the scales separately rather than simply grinding up the scales for analysis as is typically done. Figure 6.4 shows the FT-IR spectra of the intact scale's upper biomineral layer and lower collagen layer for the FS (Figure 6.4a) and FS-W (Figure 6.4b) scales. We next studied the effects of a mild acidic (Figure 6.5a), basic (Figure 6.5b), and oxidative soak (Figure 6.5c), on each surface.

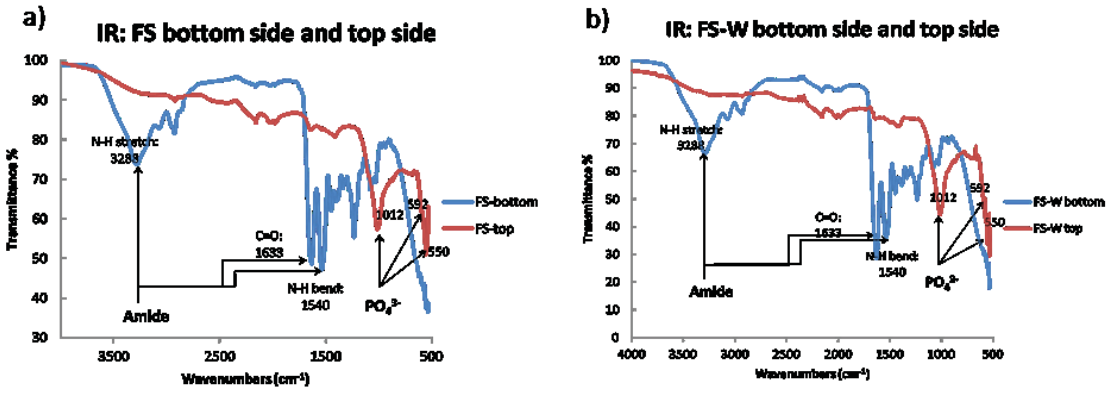


Figure 6.4 FTIR of FS (a) and FS-W (b)

The FTIR spectra of the top and bottom surfaces of FS are shown in Figure 6.4a, where all the protein bands of the collagen side are observed: i.e. the N-H stretching band (3288 $cm^{-1}$), the C=O stretch band (1633 $cm^{-1}$) and the N-H bending band (1540 $cm^{-1}$). The biomineral surface shows the expected hydroxyapatite $PO_4^{3-}$ bands at 1012 $cm^{-1}$, 592 $cm^{-1}$, and 550 $cm^{-1}$.

The FTIR spectra of the top and bottom layer of the FS-W scales, which were subjected to a low energy ultrasonic wash, are also seen in Figure 6.4b. There is little obvious difference in the two spectra, although the relative size of the amide N-H bending band

(1540 $cm^{-1}$) compared to the amide C=O stretching band (1633 $cm^{-1}$), and a small reduction in one of the alkyl C-H bands near 3000 $cm^{-1}$ may have occurred on the bottom (collagen) surface. However, as stated previously, we expected the ultrasonic washing to remove residual mucous layer components from FS, yet the bands in the biomineral layer do not appear to have changed except for loss of a very small band near 3000 $cm^{-1}$. As these components are a small part of the composition and are expected to be predominantly proteins and glycoproteins, they probably make little distinctive contribution to the FT-IR spectra.

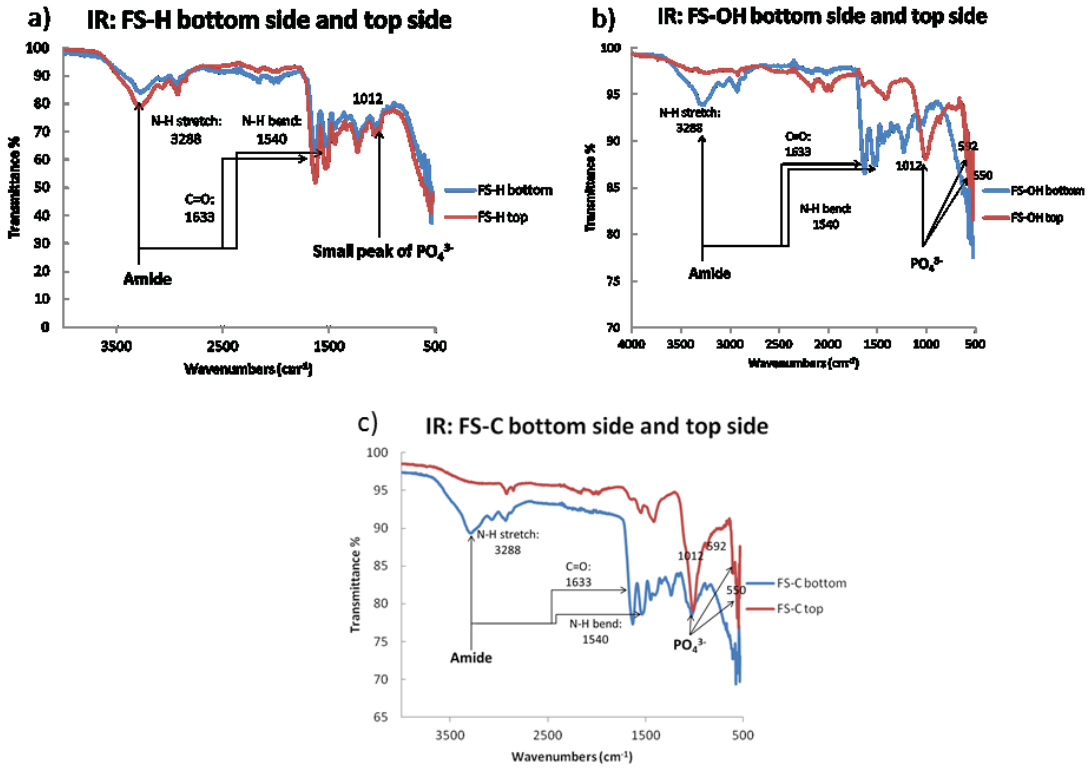


Figure 6.5 IR for soaked samples: FS-H (a), FS-OH (b) and FS-C (c)

Figure 6.5a and 5.5b compare the spectra of acid-treated (FS-H) and base-treated scales (FS-OH). Acidic solutions degrade or destroy the biomineral layer, leaving the collagen

layer behind[13d]. In contrast, basic solutions degrade or decompose collagen, leaving the biomineral layer behind.[13b]

The top surface of FS and FS-W show strong absorptions from $PO_4^{3-}$, but these bands are significantly reduced in FS-H scales, with the top surface showing only a very small band at 1012 $cm^{-1}$. The spectra of both the top and bottom surfaces of the FS-H include obvious bands from amide bonds of collagen. These bands are barely evident in the top surface of FS and FS-W. Therefore, the mild wash removed a significant portion of the biomineral layer, but not all of it, and it appears to have left the collagen layer intact. Because some of the biomineral layer is left, the extent of the biomineral layer that is removed might be adjusted by a shortened soak cycle to allow properties of the collagen layer relative to the biomineral layer to be modulated.

Similarly, the use of NaOH is an established technique to remove the collagen layer to recover hydroxyapatite[13b] since it decomposes collagen faster than the biomineral layer. After soaking the scales in NaOH(aq) under mild conditions the FTIR spectra of the top and bottom surfaces of FS-OH retained the absorption bands observed in FS and FS-W, so each layer retained significant character of the original surfaces. However, by comparing the relative areas of key amide bands it is clear that the collagen layer has been significantly reduced. Again, the relative degree of degradation of the collagen layer relative to the biomineral layer can be adjusted by the soaking conditions (time, temperature, concentration), and because base degrades the collagen layers more slowly than acid degrades the biomineral layer, its removal is likely to be more easily adjusted than that of the biomineral layer.

The FTIR of FS-C was also observed. Both bottom and top surfaces were similar to the FS and FS-W. However, relative to the collagen peak, the hydroxyapatite peaks ($PO_4^{3-}$) had strengthened. At the same time, the fish scale was visibly thinner and more brittle. The observations show that even a mild Clorox® oxidation was highly destructive to both layers, though the collagen layer appeared to be more effected than the biomineral layer.

#### 6.3.2.2 Changes in Equilibrium Moisture Content (EMC)

The EMC of the scales was significantly increased by modifications that selectively degraded either the biomineral or the collagen layer (Table 6.2, and Figure 6.6), with FS-H and FS-OH possessing EMCs of 15.5 and 12.0% respectively. This is a significant increase in EMC when compared to that of FS scales at just 6.2%. Interestingly FS-C scales, where both layers were degraded, had nearly the same EMC uptake as the FS, at 6.9%. Equally surprising is that the FS-W scales also showed a significant increase in EMC compared to FS, and rose to 11.8%. We expected that the ultrasonication would remove any residual mucus layer on the scales, but so too should the Clorox® soaking, and the FS-C scales absorbed only 6.9% moisture. These data show that the ultrasonication step altered the structure of one or both layers, resulting in nearly doubling of the moisture uptake. We saw that the cell-like features of FS were not present in those of FS-W, which suggests that the change in the scales accounting for the increased EMC was associated with the biomineral layer. But, those features were not observed on the FS-C scales either. It is possible that the ultrasonication affected the collagen layer, perhaps denaturing the collagen rods, but without additional data we cannot identify the reason for the significant difference in EMC. At this point the only

clear structural difference we have observed between a low and a high EMC scale is associated with a change in the biomineral layer.

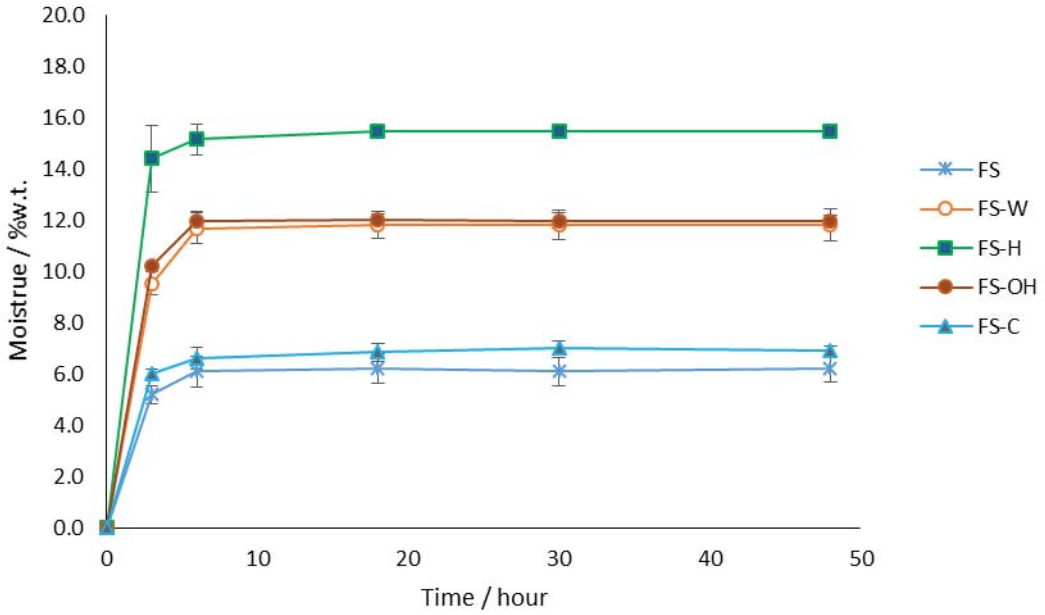


Figure 6.6 EMC of modified fish scale (Soaked with different solution)

Table 6.2 EMC of modified samples at 48 hours (80% relative humidity)

| | Modified Fish Scale (w.t.%) |
|---|---|
| FS | 6.2±0.5 |
| FS-W | 11.8±0.6 |
| FS-H | 15.5±0.2 |
| FS-OH | 12.0±0.2 |
| FS-C | 6.9±0.2 |

### 6.3.3 Polymer-modified scales

#### 6.3.3.1 Changes in composition by FTIR

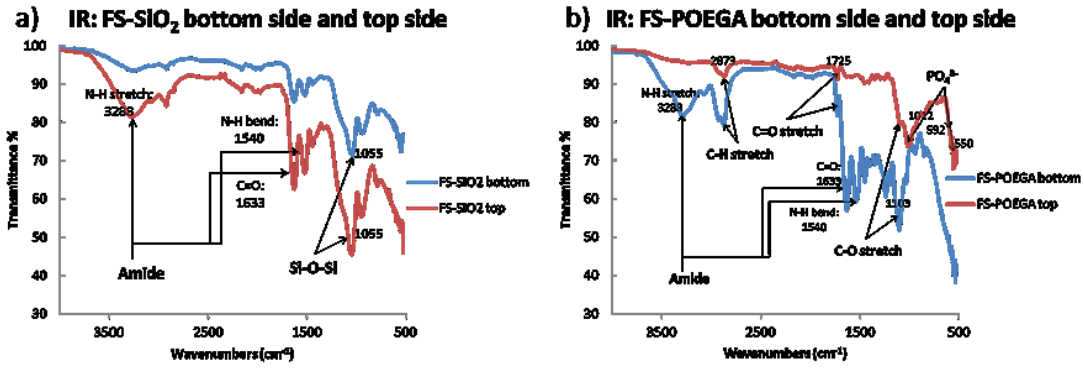


Figure 6.7 IR for polymer-modified fish scale: FS-$SiO_2$ (a) and FS-POEGA (b)

Four different modifications of the scales employed chemical changes that added polymer material to one or both scale layers. The first scale modification resulted from soaking the scales in an acidic solution of TEOS followed by heating the scales to produce $SiO_2$ in situ. This modification was non-selective, but significantly favored the biomineral layer over the collagen layer. The fact that both layers were modified (Figure 6.7a) was demonstrated by the appearance of a Si–O–Si at 1055 $cm^{-1}$ in the spectra of both the biomineral and collagen surfaces of the FS-$SiO_2$ scales. But the modification was more extensive at the biomineral surface because the $PO_4^{3-}$ bands of the biomineral surface were completely obscured while the amide bands of the collagen layer remained significant.

In contrast to this, when scales were modified by the radical polymerization of the hydrophilic OEGA monomer, a significant preference for modification of the collagen layer was seen. The FTIR of the top and bottom surfaces (Figure 6.7b) show a significant increase in the C–H stretch at 2873 cm-1 in the collagen layer, but just a small C–H

stretch is seen in the spectrum of the biomineral layer. The C=O stretching band at 1725 $cm^{-1}$ and the C-O stretching band at 1103 $cm^{-1}$ were also strong in the collagen surface's spectrum and negligible in the biomineral surface's spectrum.

Scales modified by the radical polymerization of the hydrophobic monomers, MMA or MA, yielded spectra that showed no obvious difference when compared to FS and FS-W. This could be because the hydrophobic MMA and MA monomers failed to effectively wet or penetrate into the collagen, while the more hydrophilic OEGA was able to form a membrane on the surface of the collagen layer. However, if the more hydrophobic monomers penetrated into the fish scale without significantly altering the FT-IR spectra we should still see changes in other properties.

It should be emphasized though that the scales were only soaked in monomer at room temperature, and then removed for heating to favor surface modification over extensive modification of the hierarchical scale structure. More extensive modification would be expected if the scales were immersed in heated monomer, and/or a solvent was added, but this research sought to maintain the hierarchical structure of the scale, so solvents and high heat were both avoided here. These results show that modification by metal alkoxides and by hydrophilic monomers is a facile modification while the FTIR suggest that significant modification of either scale surface is modest.

### 6.3.3.2 Changes in Equilibrium Moisture Content (EMC) of polymer-modified fish scale

Table 6.3 EMC of polymer-modified samples at 48 hours (80% relative humidity)

| Polymer-Modified Fish Scale | (w.t.%) |
|---|---|
| FS-$SiO_2$ | 10.5±0.2 |
| FS-PMMA | 11.2±0.2 |
| FS-POEGA | 9.5±0.3 |
| FS-PMA | 10.4±0.2 |

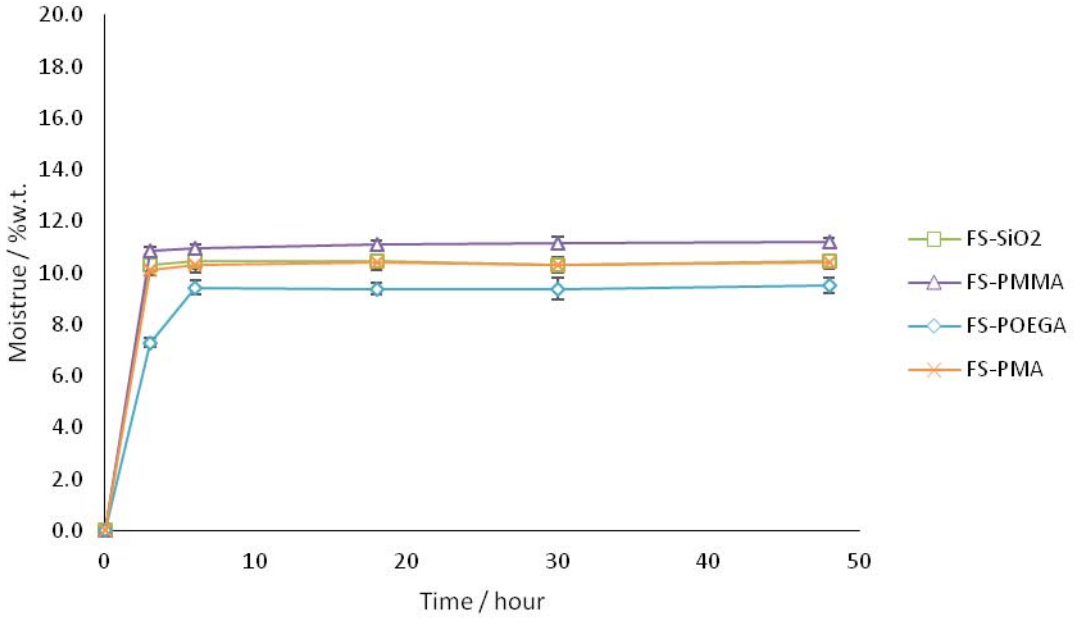


Figure 6.8 EMC of Polymer-modified fish scales

The EMC of polymer-modified samples data had been shown in Table 6.3 and Figure 6.8. Because we expected one application for an organic polymer modified fish scales might be as an additive in some packaging materials, we looked at the EMC of the polymer-modified scales. In comparison to the EMC of the FS-W scales (11.8±0.3 w.t.%) all the

polymer-modified fish scales gave some reduction in EMC, but the greatest reduction came from the most hydrophilic modification, FS-POEGA at 9.5±0.3%. The most hydrophobic organic polymer modification (FS-PMMA) gave the highest EMC at 11.2±0.2 w.t%. The fact that the scales modified with hydrophobic monomers (FS-PMMA and FS-PMA) did not give significant reductions in EMC could be because these monomers failed to significantly alter the surfaces of the scales, as suggested by the FTIR spectra. But the FTIR of FS-POEGA and FS-$SiO_2$ proved significant modification of the scales, and they also showed little significant change in the EMC compared to FS-W scales. This suggests that both the collagen and biomineral layer would need to be modified to significantly alter the EMC. But, it does still not explain exactly what change occurred during the ultrasonic treatment that resulted in such a significant rise in the EMC.

### 6.3.4 Nanomechanical properties

Another likely application for fish scales is as composite reinforcement. We tested the effects of our modifications on the nanomechanical properties of the modified, but otherwise intact, scales. We tested the surface of the biomineral layer, and tested the collagen layer in cross-section, from the middle and closer to the edge of the collagen layer.

#### 6.3.4.1 Biomineral surfaces

Table 6.4 lists the DMT modulus measured for the biomineral surface of all the scales studied here. The DMT modulus, was obtained using the peak-force tapping mode in the AFM, as described elsewhere.[25] The modulus of the as-received FS was only 3.963 GPa,

and rose slightly to 4.219 GPa for the FS-W. The slight rise in the modulus of FS-W supports the removal of some residual soft layer from the surface of FS.

The modulus of the FS-H scales should be dominated by the modulus of the collagen layer if the biomineral layer were removed, since the acid soak is intended to degrade the biomineral layer. Soaking in base was intended to degrade the collagen layer, leaving the modulus of the scale to be dominated by the biomineral layer since. However, the modulus of FS-H and FS-OH scales is quite low, at 1.767 GPa and 2.162 GPa respectively, compared to 3.963 GPa for FS. The FTIR spectra of the FS-H and FS-OH scales showed bands from collagen and the biomineral components indicating that acid and base did not degrade either layer completely but damaged both layers sufficiently to compromise the mechanical properties of the scales.

Treatment with acid destroys the hydroxyapatite directly, so loss of mechanical properties from the biomineral surface is expected. The loss of properties in the FS-OH scales may be due to the fact that hydroxyapatite is not the only component of the biomineral layer. There are other organic components that give order to the inorganic domains, so the base solution could have degraded both the collagen and the organic components in the biomineral layer, damaging the inherent structure leading to loss of properties. Further treatment of the biomineral layer with base would ultimately lead to removal of all the organic components from this layer, only leaving hydroxyapatite powder.

The most interesting result from the non-polymer modifications of scales is from the FS-C. The modulus of the FS-C scales was 4.687 GPa, which is somewhat greater than that of the FS or FS-W scales. The FTIR of the oxidized biomineral surface showed decreases

in peaks at 1540 and 1633 $cm^{-1}$ (protein) relative to the peak at 1012 $cm^{-1}$ ($PO_4^{3-}$). And, compared to the FS spectra changes in the relative ratio of the peak areas occurred in the IR spectrum of both sides of the scale, so the rise in modulus might be due to some changes in the proteins in the biomineral layer but the exact changes are not clear.

The most substantial change that resulted from one of the supplemental polymerization modifications came from the in situ hydrothermal conversion of TEOS to $SiO_2$ nanoparticles. This modification was expected to increase the modulus of the scales and to reduce the moisture uptake. Figure 6.9 shows optical and AFM images of the biomineral surface of FS, FS-$SiO_2$-C and FS-$SiO_2$. As seen from Table 6.4, the modulus of the as-received FS was only 3.963 GPa, but more than doubled to 8.572 GPa for FS-$SiO_2$-C, and rose to 22.839 GPa for FS-$SiO_2$. The structure of the biomineral surface was also visibly changed from FS (Figure 6.9a), where ridge features were clearly visible. With a 30 min immersion in acidified TEOS followed by thermal treatment the depressions begin to fill in with $SiO_2$ nanoparticles (Figure 6.9b), and the ridge features start to become obscured. After a 60 min immersion followed by the same thermal treatment the surface is nearly featureless (Figure 6.9c).

Table 6.4 Modulus (GPa) of the biomineral surface of fish scales

| Modified Fish Scale | | Polymer-Modified Fish Scale | |
|---|---|---|---|
| FS | 3.963 | FS-$SiO_2$-C | 8.572 |
| FS-W | 4.219 | FS-$SiO_2$ | 22.839 |
| FS-H | 1.767 | FS-PMMA | 4.904 |
| FS-OH | 2.162 | FS-POEGA | 1.201 |
| FS-C | 4.687 | FS-PMA | 3.821 |

All the organic polymer-modified fish scales gave small changes in modulus, but it is not obvious how much the biomineral surface of the scales was modified. The hydrophobic polymers PMMA and PMA gave small or negligible effects on the modulus (4.904 and 3.821 GPa respectively) compared to unmodified FS. Because hydrophobic materials do not readily wet hydrophilic surfaces these hydrophobic monomers and polymers may simply have failed to modify the scales to a significant extent. However, the hydrophilic OEGA monomer gave POEGA-modified scales with significantly reduced modulus (1.201 GPa). This indicates that the hydrophilic OEGA monomer altered the surface more effectively than the hydrophobic monomers, leading to a soft POEGA membrane on the surface. Modification of the biomineral surface appears to be by adsorption to the surface, rather than grafting from the surface.

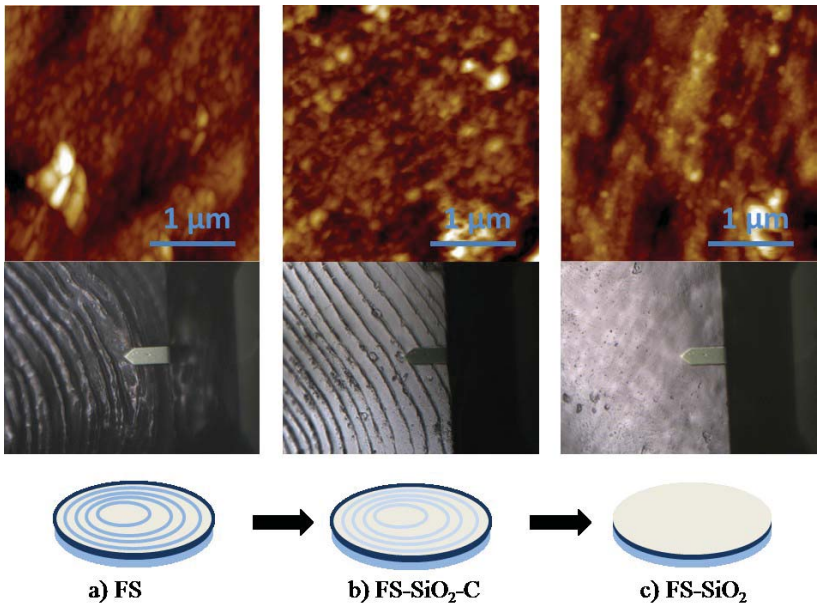


Figure 6.9 Optical and AFM images showing changes in surface features of (a) FS, (b) FS-$SIO_2$-C and (c) FS-$SiO_2$.

### 6.3.4.2 Cross section of the samples

To determine if the monomer reactants penetrated into the collagen layer we tested the mechanical properties of scale cross-sections. The modulus of the collagen was measured near the biomineral interface (labeled as "top side") and more deeply into the collagen layer (labeled as "back side") as illustrated in Figure 6.10A.

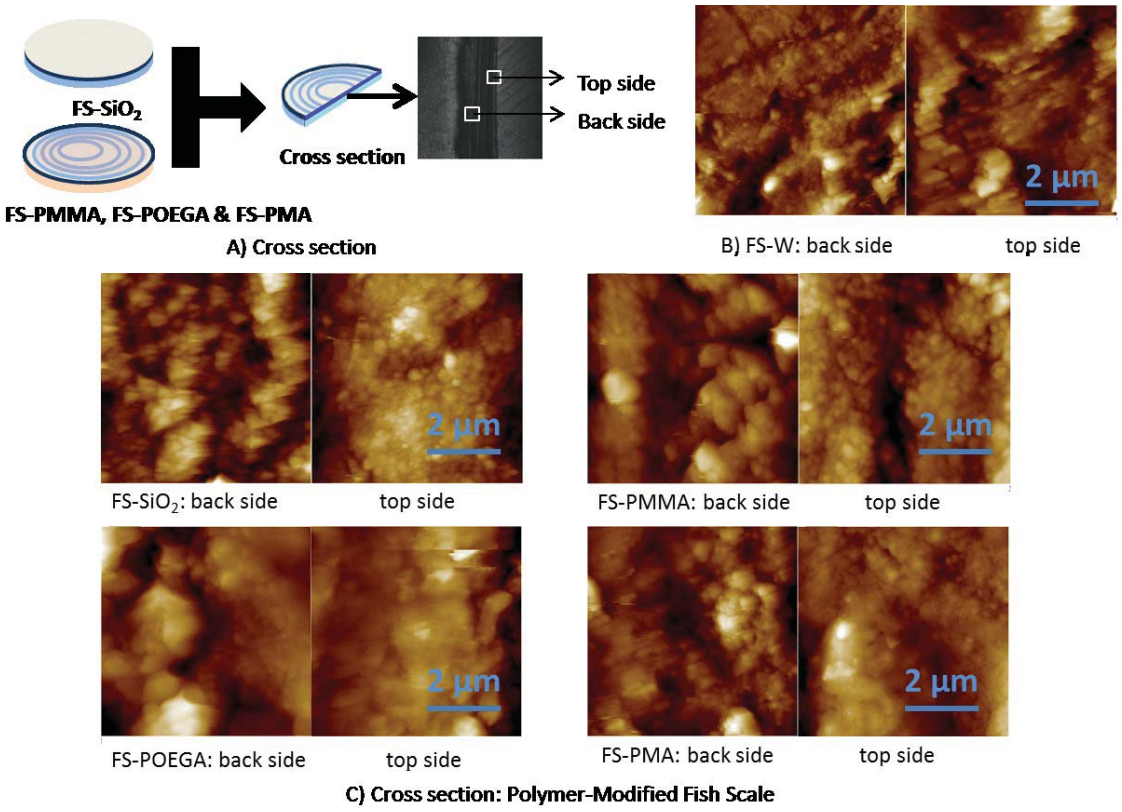


Figure 6.10 Cross section AFM test (6µm X 6µm)

The modulus of the back and top edges of the FS control was measured at 2.21 GPa and 5.24 GPa respectively (Table 6.5). In the AFM images for these sections (Figure 6.10B left and right respectively) the collagen rods are clearly visible. The higher modulus from the top side collagen rods is attributed to the reinforcing effect of the intact biomineral layer.

When the scales were modified by TEOS, the AFM image (Figure 6.10C, top left) clearly shows the presence of $SiO_2$ nanoparticles. In the topside image the nanoparticles completely obscure the appearance of the bundles of collagen rods, while in the backside images the bundles are still visible. The size of individual SiO2 nanoparticles is not clear, but most of the aggregates appear to be ~ 100 nm. The presence of these nanoparticles within the collagen layer verifies confirms the FTIR results that showed $SiO_2$ in both the biomineral and collagen layers. The reinforcing effect of the $SiO_2$ on the collagen phase is confirmed by the significant rise in modulus both near the biomineral surface and deep within the collagen layer too (12.67 GPa and 10.21 GPa respectively).

Table 6.5 Modulus of cross-sectional layers of scales (GPa)

| Modulus | FS-W | FS-$SiO_2$ | FS-PMMA | FS-PMA | FS-POEGA |
|---|---|---|---|---|---|
| Near Top Edge | 5.24 | 12.67 | 4.30 | 3.31 | 6.89 |
| Near Back Edge | 2.21 | 10.21 | 3.64 | 2.23 | 2.08 |

When the scales were modified with hydrophobic monomers, MMA and MA, the modulus near the biomineral layer of FS-PMMA and FS-PMA was reduced, compared to FS-W. Interestingly, the modulus of FS-PMMA within the collagen layer was increased relative to FS-W, while that of FS-PMA was unaffected. These effects may be due to some small degree of modification by polymers with relatively high (PMMA) and low (PMA) $T_g$s. FTIR did not show evidence that either surface of the scales was modified by MMA or MA, but the change in the modulus suggests there might have been some degree

of modification. However, as these changes are relatively small and the reasons for them need to be better understood.

When the scales were modified with OEGA there was a very small change in the modulus of the collagen layer but the modulus near the biomineral surface rose was 6.89 GPa compared to the FS-W control at 5.24 GPa. The modulus near the bottom edge was slightly smaller than the control (2.08 GPa compared to 2.21 GPa). In this case though the FTIR was able to confirm chemical modification by the hydrophilic OEGA monomer. The softening of the collagen layer could be attributed to the ability of the ethylene glycol units to interact with the collagen protein and to hydrogen bond with it, but the higher modulus near the biomineral layer is less clear. Also, the bundles of collagen rods are less distinct than in the other images, suggesting the possibility that the OEGA disrupted the collagen arrays. However, all these modifications need to be studied further.

## 6.4 Conclusions

This work sought to explore the possibility of expanding the use of fish scales as a waste resource, from beyond that of simply harvesting their major components, and to see if beneficial properties could be obtained by using their inherent hierarchical design. Because this hierarchical structure uses alternating layers of collagen rods and an upper biomineral layer, scales possess excellent toughness and the design has some similarities to structures that have useful gas barrier properties. Fish scale structures may find potential applications for use in biodegradable composites, packaging, or gas barrier materials. Because all these potential applications will require good interfacial adhesion between the scale and the matrix this research focused on investigating how different

chemical modifications affected chemical functionality, moisture uptake, and nanomehcnaical properties. This is the first research to investigate chemical modifications of fish scales and their effects on functionality and nanomechanical properties of modified fish scales. We also investigated the individual effects of modification on the biomineral and the collagen layer of the scale. The key positive findings are that while modifications can be targeted to the biomineral or the collagen layer, all the modifications had some effect on both layers. Gentle acid treatment partially removes the biomineral layer while gentle base treatment partially removes the collagen layer, but both treatments affected both layers. The less selective modification was base treatment, presumably because organic domains within the biomineral layer were also hydrolyzed by this treatment. A partial degradation of the collagen layer increased the nanomechanical modulus of the scale, presumably at the expense of the toughness, which is an attribute of the tiered collagen rods. Chemical modifications made by soaking in hydrophilic or hydrophobic monomers, followed by polymerizing the monomer in situ, showed that hydrophobic monomers were less successful in modifying the scales than hydrophilic ones, based on little change in FTIR spectra, but significant changes in the nanomechanical properties at both surfaces showed that modification occurred. Changes at the biomineral surface are attributed to adsorbed polymer that is not removed by washing with water. Both hydrophobic and hydrophilic modifications resulted in increasing the EMC of the scales compared to unmodified scales, which suggests that unidentified structural changes occurring to the scales that permitted the additional moisture uptake. Modification of the scales by TEOS resulted in substantial increases in the modulus of both the biomineral and collagen layers, arising from the formation of

$SiO_2$ nanoparticles. The overall significance of these results is that the two different scale surfaces can be preferentially modified even if not independently modified, and that the wide range of modifications may allow these scales to be used in other applications while enhancing selected properties and altering interfaces for interaction with desired matrices. This work showed that a wide range of modifications is possible to adjust the modulus and polarity of a scale interface, though one issue that will need to be addressed before scales can find wider use is designing efficient scale size reduction tools, particularly one based on cutting rather than grinding, to enhance blending of scales into polymer matrices.

# References

## Chapter 2 references


1. Moad, G.; Rizzardo, E.; Thang, S. H., Radical addition-fragmentation chemistry in polymer synthesis. *Polymer* **2008,** *49* (5), 1079-1131.

2. Chiefari, J.; Chong, Y. K.; Ercole, F.; Krstina, J.; Jeffery, J.; Le, T. P. T.; Mayadunne, R. T. A.; Meijs, G. F.; Moad, C. L.; Moad, G.; Rizzardo, E.; Thang, S. H., Living free-radical polymerization by reversible addition-fragmentation chain transfer: The RAFT process. *Macromolecules* **1998,** *31* (16), 5559-5562.

3. Moad, G.; Chong, Y. K.; Postma, A.; Rizzardo, E.; Thang, S. H., Advances in RAFT polymerization: the synthesis of polymers with defined end-groups. *Polymer* **2005,** *46* (19), 8458-8468.

4. Willcock, H.; O'Reilly, R. K., End group removal and modification of RAFT polymers. *Polym Chem-Uk* **2010,** *1* (2), 149-157.

5. Thomas, D. B.; Convertine, A. J.; Myrick, L. J.; Scales, C. W.; Smith, A. E.; Lowe, A. B.; Vasilieva, Y. A.; Ayres, N.; McCormick, C. L., Kinetics and molecular weight control of the polymerization of acrylamide via RAFT. *Macromolecules* **2004,** *37* (24), 8941-8950.

6. Inoue, Y.; Watanabe, J.; Takai, M.; Yusa, S.; Ishihara, K., Synthesis of sequence-controlled copolymers from extremely polar and apolar monomers by living radical polymerization and their phase-separated structures. *J Polym Sci Pol Chem* **2005,** *43* (23), 6073-6083.

7. Semsarilar, M.; Perrier, S., 'Green' reversible addition-fragmentation chain-transfer (RAFT) polymerization. *Nat Chem* **2010,** *2* (10), 811-820.

8. McCormack, C. L.; Lowe, A. B., Aqueous RAFT polymerization: Recent developments in synthesis of functional water-soluble (Co)polymers with controlled structures. *Accounts Chem Res* **2004,** *37* (5), 312-325.

9. (a) Moad, G.; Rizzardo, E.; Thang, S. H., End-functional polymers, thiocarbonylthio group removal/transformation and reversible addition-fragmentation-chain transfer (RAFT) polymerization. *Polym Int* **2011,** *60* (1), 9-25; (b) Boyer, C.; Liu, J. Q.; Bulmus, V.; Davis, T. P., RAFT Polymer End-Group Modification and Chain Coupling/Conjugation Via Disulfide Bonds. *Aust J Chem* **2009,** *62* (8), 830-847.

10. (a) Chiefari, J.; Mayadunne, R. T. A.; Moad, C. L.; Moad, G.; Rizzardo, E.; Postma, A.; Skidmore, M. A.; Thang, S. H., Thiocarbonylthio compounds (S=C(Z)S-R) in free radical polymerization with reversible addition-fragmentation chain transfer (RAFT polymerization). Effect of the activating group Z. *Macromolecules* **2003,** *36* (7), 2273-2283; (b) Chong, Y. K.; Krstina, J.; Le, T. P. T.; Moad, G.; Postma, A.; Rizzardo, E.; Thang, S. H., Thiocarbonylthio compounds [S=C(Ph)S-R] in free radical polymerization with reversible addition-fragmentation chain transfer (RAFT polymerization). Role of the free-radical leaving group (R). *Macromolecules* **2003,** *36* (7), 2256-2272.

11. Perrier, S.; Takolpuckdee, P., Macromolecular design via reversible addition-fragmentation chain transfer (RAFT)/Xanthates (MADIX) polymerization. *J Polym Sci Pol Chem* **2005,** *43* (22), 5347-5393.

12. Dureault, A.; Gnanou, Y.; Taton, D.; Destarac, M.; Leising, F., Reaction of cyclic tetrathiophosphates with carboxylic acids as a means to generate dithioesters and control

radical polymerization by RAFT. *Angew Chem Int Edit* **2003,** *42* (25), 2869-2872.

13. Dureault, A.; Taton, D.; Destarac, M.; Leising, F.; Gnanou, Y., Synthesis of multifunctional dithioesters using tetraphosphorus decasulfide and their behavior as RAFT agents. *Macromolecules* **2004,** *37* (15), 5513-5519.

14. Sudalai, A.; Kanagasabapathy, S.; Benicewicz, B. C., Phosphorus pentasulfide: A mild and versatile catalyst-reagent for the preparation of dithiocarboxylic esters. *Org Lett* **2000,** *2* (20), 3213-3216.

15. Bouhadir, G.; Legrand, N.; Quiclet-Sire, B.; Zard, S. Z., A new practical synthesis of tertiary S-alkyl dithiocarbonates and related derivatives. *Tetrahedron Lett* **1999,** *40* (2), 277-280.

16. Quiclet-Sire, B.; Zard, S. Z., Powerful carbon-carbon bond forming reactions based on a novel radical exchange process. *Chem-Eur J* **2006,** *12* (23), 6002-6016.

17. Skey, J.; O'Reilly, R. K., Facile one pot synthesis of a range of reversible addition-fragmentation chain transfer (RAFT) agents. *Chem Commun* **2008,** (35), 4183-4185.

18. (a) Wang, L.; Zeng, K.; Zheng, S. X., Hepta(3,3,3-trifluoropropyl) Polyhedral Oligomeric Silsesquioxane-capped Poly(N-isopropylacrylamide) Telechelics: Synthesis and Behavior of Physical Hydrogels. *Acs Appl Mater Inter* **2011,** *3* (3), 898-909; (b) Lai, J. T.; Filla, D.; Shea, R., Functional polymers from novel carboxyl-terminated trithiocarbonates as highly efficient RAFT agents. *Macromolecules* **2002,** *35* (18), 6754-6756.

19. Strube, O. I.; Nothdurft, L.; Drache, M.; Schmidt-Naake, G., A Novel Bifunctional Trithiocarbonate for Styrene and Methacrylate RAFT Polymerization. *Macromol Chem Phys* **2011,** *212* (6), 574-582.

20. Bivigou-Koumba, A. M.; Kristen, J.; Laschewsky, A.; Muller-Buschbaum, P.; Papadakis, C. M., Synthesis of Symmetrical Triblock Copolymers of Styrene and N-isopropylacrylamide Using Bifunctional Bis(trithiocarbonate)s as RAFT Agents. *Macromol Chem Phys* **2009,** *210* (7), 565-578.

21. Li, D. X.; He, Q. A.; Li, J. B., Smart core/shell nanocomposites: Intelligent polymers modified gold nanoparticles. *Adv Colloid Interfac* **2009,** *149* (1-2), 28-38.

22. Yang, Y. F.; Song, X. H.; Yuan, L.; Li, M.; Liu, J. C.; Ji, R. Q.; Zhao, H. Y., Synthesis of PNIPAM Polymer Brushes on Reduced Graphene Oxide Based on Click Chemistry and RAFT Polymerization. *J Polym Sci Pol Chem* **2012,** *50* (2), 329-337.

23. Takolpuckdee, P.; Mars, C. A.; Perrier, S., Merrifield resin-supported chain transfer agents, precursors for RAFT polymerization. *Org Lett* **2005,** *7* (16), 3449-3452.

24. Wiss, K. T.; Kessler, D.; Wendorff, T. J.; Theato, P., Versatile Responsive Surfaces via Hybrid Polymers Containing Acetal Side Groups. *Macromol Chem Phys* **2009,** *210* (15), 1201-1209.

25. Postma, A.; Davis, T. P.; Moad, G.; O'Shea, M. S., Thermolysis of RAFT-synthesized polymers. A convenient method for trithiocarbonate group elimination. *Macromolecules* **2005,** *38* (13), 5371-5374.

26. Chong, B.; Moad, G.; Rizzardo, E.; Skidmore, M.; Thang, S. H., Thermolysis of RAFT-synthesized poly(methyl methacrylate). *Aust J Chem* **2006,** *59* (10), 755-762.

27. Lowe, A. B.; Sumerlin, B. S.; Donovan, M. S.; McCormick, C. L., Facile preparation of transition metal nanoparticles stabilized by well-defined (Co)polymers synthesized via aqueous reversible addition-fragmentation chain transfer polymerization. *J Am Chem Soc* **2002,** *124* (39), 11562-11563.

28. Inglis, A. J.; Stenzel, M. H.; Barner-Kowollik, C., Ultra-Fast RAFT-HDA Click Conjugation: An Efficient Route to High Molecular Weight Block Copolymers. *Macromol Rapid Comm* **2009,** *30* (21), 1792-1798.

## Chapter 3 references


1. Jeong, B.; Gutowska, A., Lessons from nature: stimuli-responsive polymers and their biomedical applications. *Trends Biotechnol* **2002,** *20* (7), 305-311.

2. (a) Ward, M. A.; Georgiou, T. K., Thermoresponsive Polymers for Biomedical Applications. *Polymers-Basel* **2011,** *3* (3), 1215-1242; (b) Skrabania, K.; Kristen, J.; Laschewsky, A.; Akdemir, O.; Hoth, A.; Lutz, J. F., Design, synthesis, and aqueous aggregation behavior of nonionic single and multiple thermoresponsive polymers. *Langmuir* **2007,** *23* (1), 84-93; (c) Georgiou, T. K.; Vamvakaki, M.; Patrickios, C. S.; Yamasaki, E. N.; Phylactou, L. A., Nanoscopic cationic methacrylate star homopolymers: Synthesis by group transfer polymerization, characterization and evaluation as transfection reagents. *Biomacromolecules* **2004,** *5* (6), 2221-2229.

3. Schmaljohann, D., Thermo- and pH-responsive polymers in drug delivery. *Adv Drug Deliver Rev* **2006,** *58* (15), 1655-1670.

4. Schafer, C. G.; Gallei, M.; Zahn, J. T.; Engelhardt, J.; Hellmann, G. P.; Rehahn, M., Reversible Light-, Thermo-, and Mechano-Responsive Elastomeric Polymer Opal Films. *Chem Mater* **2013,** *25* (11), 2309-2318.

5. Willett, J. L., Humidity-responsive starch-poly(methyl acrylate) films. *Macromol Chem Physic* **2008,** *209* (7), 764-772.

6. (a) Hoffman, A. S., Stimuli-responsive polymers: Biomedical applications and challenges for clinical translation. *Adv Drug Deliver Rev* **2013,** *65* (1), 10-16; (b) Krasia-Christoforou, T.; Georgiou, T. K., Polymeric theranostics: using polymer-based systems for simultaneous imaging and therapy. *J Mater Chem B* **2013,** *1* (24), 3002-3025.

7. (a) Vancoillie, G.; Frank, D.; Hoogenboom, R., Thermoresponsive poly(oligo

ethylene glycol acrylates). *Prog Polym Sci* **2014,** *39* (6), 1074-1095; (b) Lutz, J. F., Polymerization of oligo(ethylene glycol) (meth)acrylates: Toward new generations of smart biocompatible materials. *J Polym Sci Pol Chem* **2008,** *46* (11), 3459-3470; (c) Lutz, J. F.; Weichenhan, K.; Akdemir, O.; Hoth, A., About the phase transitions in aqueous solutions of thermoresponsive copolymers and hydrogels based on 2-(2-methoxyethoxy)ethyl methacrylate and oligo(ethylene glycol) methacrylate. *Macromolecules* **2007,** *40* (7), 2503-2508.

8. (a) Ward, M. A.; Georgiou, T. K., Multicompartment thermoresponsive gels: does the length of the hydrophobic side group matter? *Polym Chem-Uk* **2013,** *4* (6), 1893-1902; (b) Ward, M. A.; Georgiou, T. K., Thermoresponsive triblock copolymers based on methacrylate monomers: effect of molecular weight and composition. *Soft Matter* **2012,** *8* (9), 2737-2745; (c) Kurzbach, D.; Schomer, M.; Wilms, V. S.; Frey, H.; Hinderberger, D., How Structure-Related Collapse Mechanisms Determine Nanoscale Inhomogeneities in Thermoresponsive Polymers. *Macromolecules* **2012,** *45* (18), 7535-7548; (d) Aseyev, V.; Tenhu, H.; Winnik, F. M., Non-ionic Thermoresponsive Polymers in Water. *Adv Polym Sci* **2011,** *242*, 29-89; (e) Kim, M. S.; Hyun, H.; Seo, K. S.; Cho, Y. H.; Lee, J. W.; Lee, C. R.; Khang, G.; Lee, H. B., Preparation and characterization of MPEG-PCL diblock copolymers with thermo-responsive sol-gel-sol phase transition. *J Polym Sci Pol Chem* **2006,** *44* (18), 5413-5423; (f) Ward, M. A.; Georgiou, T. K., Thermoresponsive Terpolymers Based on Methacrylate Monomers: Effect of Architecture and Composition. *J Polym Sci Pol Chem* **2010,** *48* (4), 775-783.

9. Furyk, S.; Zhang, Y. J.; Ortiz-Acosta, D.; Cremer, P. S.; Bergbreiter, D. E., Effects of end group polarity and molecular weight on the lower critical solution temperature of

poly(N-isopropylacrylamide). *J Polym Sci Pol Chem* **2006,** *44* (4), 1492-1501.

10. Huber, S.; Hutter, N.; Jordan, R., Effect of end group polarity upon the lower critical solution temperature of poly(2-isopropyl-2-oxazoline). *Colloid Polym Sci* **2008,** *286* (14-15), 1653-1661.

11. Carter, S.; Hunt, B.; Rimmer, S., Highly branched poly(N-isopropylacrylamide)s with imidazole end groups prepared by radical polymerization in the presence of a styryl monomer containing a dithioester group. *Macromolecules* **2005,** *38* (11), 4595-4603.

12. Chen, N.; Xiang, X.; Tiwari, A.; Heiden, P. A., Tuning thermoresponsive behavior of diblock copolymers and their gold core hybrids Part 1. Importance of placement of amphiphilic end groups on the diblock copolymers. *J Colloid Interf Sci* **2013,** *391*, 60-69.

13. Zhang, Y.; Furyk, S.; Sagle, L. B.; Cho, Y.; Bergbreiter, D. E.; Cremer, P. S., Effects of Hofmeister anions on the LCST of PNIPAM as a function of molecular weight. *J Phys Chem C* **2007,** *111* (25), 8916-8924.

14. Lai, J. T.; Filla, D.; Shea, R., Functional polymers from novel carboxyl-terminated trithiocarbonates as highly efficient RAFT agents. *Macromolecules* **2002,** *35* (18), 6754-6756.

15. Aoyagi, N.; Endo, T., Functional RAFT Agents for Radical-Controlled Polymerization: Quantitative Synthesis of Trithiocarbonates Containing Functional Groups as RAFT Agents Using Equivalent Amount of CS2. *J Polym Sci Pol Chem* **2009,** *47* (14), 3702-3709.

16. Dureault, A.; Taton, D.; Destarac, M.; Leising, F.; Gnanou, Y., Synthesis of multifunctional dithioesters using tetraphosphorus decasulfide and their behavior as RAFT agents. *Macromolecules* **2004,** *37* (15), 5513-5519.

17. Lessard, D. G.; Ousalem, M.; Zhu, X. X., Effect of the molecular weight on the lower critical solution temperature of poly(N,N-diethylacrylamide) in aqueous solutions. *Can J Chem* **2001,** *79* (12), 1870-1874.

18. Lutz, J. F.; Andrieu, J.; Uzgun, S.; Rudolph, C.; Agarwal, S., Biocompatible, thermoresponsive, and biodegradable: Simple preparation of "all-in-one" biorelevant polymers. *Macromolecules* **2007,** *40* (24), 8540-8543.

## Chapter 4 references

1. (a) Ward, M. A.; Georgiou, T. K., Thermoresponsive Polymers for Biomedical Applications. *Polymers-Basel* **2011,** *3* (3), 1215-1242; (b) Chaterji, S.; Kwon, I. K.; Park, K., Smart polymeric gels: Redefining the limits of biomedical devices. *Prog Polym Sci* **2007,** *32* (8-9), 1083-1122; (c) Bag, D. S.; Rao, K. U. B., Smart polymers and their applications. *J Polym Mater* **2006,** *23* (3), 225-248.

2. (a) Aseyev, V.; Tenhu, H.; Winnik, F. M., Non-ionic Thermoresponsive Polymers in Water. *Adv Polym Sci* **2011,** *242*, 29-89; (b) Aseyev, V.; Hietala, S.; Laukkanen, A.; Nuopponen, M.; Confortini, O.; Du Prez, F. E.; Tenhu, H., Mesoglobules of thermoresponsive polymers in dilute aqueous solutions above the LCST. *Polymer* **2005,** *46* (18), 7118-7131; (c) Luzon, M.; Boyer, C.; Peinado, C.; Corrales, T.; Whittaker, M.; Tao, L.; Davis, T. P., Water-Soluble, Thermoresponsive, Hyperbranched Copolymers Based on PEG-Methacrylates: Synthesis, Characterization, and LCST Behavior. *J Polym Sci Pol Chem* **2010,** *48* (13), 2783-2792.

3. Shah, S. S.; Wertheim, J.; Wang, C. T.; Pitt, C. G., Polymer-drug conjugates: Manipulating drug delivery kinetics using model LCST systems. *J Control Release* **1997,** *45* (1), 95-101.

4. (a) Bae, Y. H.; Park, K., Targeted drug delivery to tumors: Myths, reality and possibility. *J Control Release* **2011,** *153* (3), 198-205; (b) Singh, R.; Lillard, J. W., Nanoparticle-based targeted drug delivery. *Exp Mol Pathol* **2009,** *86* (3), 215-223; (c) Fahmy, T. M.; Fong, P. M.; Goyal, A.; Saltzman, W. M., Targeted for drug delivery. *Mater Today* **2005,** *8* (8), 18-26.

5. (a) Zhang, Y.; Hong, H.; Cai, W., Tumor-Targeted Drug Delivery with Aptamers.

*Curr Med Chem* **2011,** *18* (27), 4185-4194; (b) Zhu, J.; Huang, H.; Dong, S. W.; Ge, L.; Zhang, Y., Progress in Aptamer-Mediated Drug Delivery Vehicles for Cancer Targeting and Its Implications in Addressing Chemotherapeutic Challenges. *Theranostics* **2014,** *4* (9), 931-944; (c) Tan, W. H.; Wang, H.; Chen, Y.; Zhang, X. B.; Zhu, H. Z.; Yang, C. Y.; Yang, R. H.; Liu, C., Molecular aptamers for drug delivery. *Trends Biotechnol* **2011,** *29* (12), 634-640.

6. (a) Palorini, R.; Cammarata, F. P.; Balestrieri, C.; Monestiroli, A.; Vasso, M.; Gelfi, C.; Alberghina, L.; Chiaradonna, F., Glucose starvation induces cell death in K-ras-transformed cells by interfering with the hexosamine biosynthesis pathway and activating the unfolded protein response (vol 4, e732, 2013). *Cell Death Dis* **2013,** *4*; (b) Davis, B. G.; Robinson, M. A., Drug delivery systems based on sugar-macromolecule conjugates. *Curr Opin Drug Di De* **2002,** *5* (2), 279-288.

7. Wong, A.; Toth, I., Lipid, sugar and liposaccharide based delivery systems. *Curr Med Chem* **2001,** *8* (9), 1123-1136.

8. (a) McBain, S. C.; Yiu, H. H. P.; Dobson, J., Magnetic nanoparticles for gene and drug delivery. *Int J Nanomed* **2008,** *3* (2), 169-180; (b) Dobson, J., Magnetic nanoparticles for drug delivery. *Drug Develop Res* **2006,** *67* (1), 55-60; (c) Verma, N. K.; Crosbie-Staunton, K.; Satti, A.; Gallagher, S.; Ryan, K. B.; Doody, T.; McAtamney, C.; MacLoughlin, R.; Galvin, P.; Burke, C. S.; Volkov, Y.; Gun'ko, Y. K., Magnetic core-shell nanoparticles for drug delivery by nebulization. *J Nanobiotechnol* **2013,** *11*.

9. Liu, J.; Huang, Y. R.; Kumar, A.; Tan, A.; Jin, S. B.; Mozhi, A.; Liang, X. J., pH-Sensitive nano-systems for drug delivery in cancer therapy. *Biotechnol Adv* **2014,** *32* (4), 693-710.

10. Liu, T. Y.; Hu, S. H.; Liu, K. H.; Shaiu, R. S.; Liu, D. M.; Chen, S. Y., Instantaneous Drug Delivery of Magnetic/Thermally Sensitive Nanospheres by a High-Frequency Magnetic Field. *Langmuir* **2008,** *24* (23), 13306-13311.

11. Liechty, W. B.; Kryscio, D. R.; Slaughter, B. V.; Peppas, N. A., Polymers for Drug Delivery Systems. *Annu Rev Chem Biomol* **2010,** *1*, 149-173.

12. De Koker, S.; Hoogenboom, R.; De Geest, B. G., Polymeric multilayer capsules for drug delivery. *Chem Soc Rev* **2012,** *41* (7), 2867-2884.

13. Yang, X. Y.; Zhang, X. Y.; Liu, Z. F.; Ma, Y. F.; Huang, Y.; Chen, Y., High-Efficiency Loading and Controlled Release of Doxorubicin Hydrochloride on Graphene Oxide. *J Phys Chem C* **2008,** *112* (45), 17554-17558.

14. He, Q. J.; Shi, J. L., Mesoporous silica nanoparticle based nano drug delivery systems: synthesis, controlled drug release and delivery, pharmacokinetics and biocompatibility. *J Mater Chem* **2011,** *21* (16), 5845-5855.

15. (a) Soppimath, K. S.; Aminabhavi, T. M.; Kulkarni, A. R.; Rudzinski, W. E., Biodegradable polymeric nanoparticles as drug delivery devices. *J Control Release* **2001,** *70* (1-2), 1-20; (b) Shi, Y.; van Steenbergen, M. J.; Teunissen, E. A.; Novo, L.; Gradmann, S.; Baldus, M.; van Nostrum, C. F.; Hennink, W. E., Pi-Pi Stacking Increases the Stability and Loading Capacity of Thermosensitive Polymeric Micelles for Chemotherapeutic Drugs. *Biomacromolecules* **2013,** *14* (6), 1826-1837.

16. Sachdev, D.; Yee, D., Disrupting insulin-like growth factor signaling as a potential cancer therapy. *Mol Cancer Ther* **2007,** *6* (1), 1-12.

17. Albrecht, M. A.; Evans, C. W.; Raston, C. L., Green chemistry and the health implications of nanoparticles. *Green Chem* **2006,** *8* (5), 417-432.

18. Jordan, A.; Scholz, R.; Wust, P.; Fahling, H.; Felix, R., Magnetic fluid hyperthermia (MFH): Cancer treatment with AC magnetic field induced excitation of biocompatible superparamagnetic nanoparticles. *J Magn Magn Mater* **1999,** *201*, 413-419.

19. Honda, M.; Saito, Y.; Smith, N. I.; Fujita, K.; Kawata, S., Nanoscale heating of laser irradiated single gold nanoparticles in liquid. *Opt Express* **2011,** *19* (13), 12375-12383.

20. (a) Xiong, X. Y.; Tam, K. C.; Gan, L. H., Release kinetics of hydrophobic and hydrophilic model drugs from pluronic F127/poly(lactic acid) nanoparticles. *J Control Release* **2005,** *103* (1), 73-82; (b) Song, B. T.; Wu, C. T.; Chang, J., Controllable delivery of hydrophilic and hydrophobic drugs from electrospun poly(lactic-co-glycolic acid)/mesoporous silica nanoparticles composite mats. *J Biomed Mater Res B* **2012,** *100B* (8), 2178-2186.

21. Aqil, A.; Qiu, H. J.; Greisch, J. F.; Jerome, R.; De Pauw, E.; Jerome, C., Coating of gold nanoparticles by thermosensitive poly(N-isopropylacrylamide) end-capped by biotin. *Polymer* **2008,** *49* (5), 1145-1153.

22. Whittaker, M. R.; Goh, Y. K.; Gemici, H.; Legge, T. M.; Perrier, S.; Monteiro, M. J., Synthesis of monocyclic and linear polystyrene using the reversible coupling/cleavage of thiol/disulfide groups. *Macromolecules* **2006,** *39* (26), 9028-9034.

23. Chen, N.; Xiang, X.; Heiden, P. A., Tuning thermoresponsive behavior of diblock copolymers and their gold core hybrids. Part 2. How properties change depending on block attachment to gold nanoparticles. *J Colloid Interf Sci* **2013,** *396*, 39-46.

24. Chen, N.; Xiang, X.; Tiwari, A.; Heiden, P. A., Tuning thermoresponsive behavior of diblock copolymers and their gold core hybrids Part 1. Importance of placement of

amphiphilic end groups on the diblock copolymers. *J Colloid Interf Sci* **2013,** *391*, 60-69.

25. Dash, S.; Murthy, P. N.; Nath, L.; Chowdhury, P., Kinetic Modeling on Drug Release from Controlled Drug Delivery Systems. *Acta Pol Pharm* **2010,** *67* (3), 217-223.

## Chapter 5 references

1. Chen, R. R.; Mooney, D. J., Polymeric growth factor delivery strategies for tissue engineering. *Pharmaceut Res* **2003,** *20* (8), 1103-1112.

2. (a) Whitaker, M. J.; Quirk, R. A.; Howdle, S. M.; Shakesheff, K. M., Growth factor release from tissue engineering scaffolds. *J Pharm Pharmacol* **2001,** *53* (11), 1427-1437; (b) Schneider, A.; Garlick, J. A.; Egles, C., Self-Assembling Peptide Nanofiber Scaffolds Accelerate Wound Healing. *Plos One* **2008,** *3* (1).

3. (a) Burdick, J. A.; Mason, M. N.; Hinman, A. D.; Thorne, K.; Anseth, K. S., Delivery of osteoinductive growth factors from degradable PEG hydrogels influences osteoblast differentiation and mineralization. *J Control Release* **2002,** *83* (1), 53-63; (b) Chen, N. C.; Zhang, Z. Y.; Soontornworajit, B.; Zhou, J.; Wang, Y., Cell adhesion on an artificial extracellular matrix using aptamer-functionalized PEG hydrogels. *Biomaterials* **2012,** *33* (5), 1353-1362; (c) Schwall, C. T.; Banerjee, I. A., Micro- and Nanoscale Hydrogel Systems for Drug Delivery and Tissue Engineering. *Materials* **2009,** *2* (2), 577-612; (d) Gong, Y. H.; He, L. J.; Li, J.; Zhou, Q. L.; Ma, Z. W.; Gao, C. Y.; Shen, J. C., Hydrogel-filled polylactide porous scaffolds for cartilage tissue engineering. *J Biomed Mater Res B* **2007,** *82B* (1), 192-204; (e) Roh, J. D.; Sawh-Martinez, R.; Brennan, M. P.; Jay, S. M.; Devine, L.; Rao, D. A.; Yi, T.; Mirensky, T. L.; Nalbandian, A.; Udelsman, B.; Hibino, N.; Shinoka, T.; Saltzman, W. M.; Snyder, E.; Kyriakides, T. R.; Pober, J. S.; Breuer, C. K., Tissue-engineered vascular grafts transform into mature blood vessels via an inflammation-mediated process of vascular remodeling. *P Natl Acad Sci USA* **2010,** *107* (10), 4669-4674; (f) Shapiro, J. M.; Oyen, M. L., Hydrogel Composite Materials for Tissue Engineering Scaffolds. *Jom-Us* **2013,** *65* (4), 505-516; (g) Zustiak, S. P.; Wei, Y.

Q.; Leach, J. B., Protein-Hydrogel Interactions in Tissue Engineering: Mechanisms and Applications. *Tissue Eng Part B-Re* **2013,** *19* (2), 160-171; (h) Li, X. R.; Xiao, Z. F.; Han, J.; Chen, L.; Xiao, H. S.; Ma, F. K.; Hou, X. L.; Li, X.; Sun, J.; Ding, W. Y.; Zhao, Y. N.; Chen, B.; Dai, J. W., Promotion of neuronal differentiation of neural progenitor cells by using EGFR antibody functionalized collagen scaffolds for spinal cord injury repair. *Biomaterials* **2013,** *34* (21), 5107-5116; (i) Nandi, S. K.; Kundu, B.; Basu, D., Protein growth factors loaded highly porous chitosan scaffold: A comparison of bone healing properties. *Mat Sci Eng C-Mater* **2013,** *33* (3), 1267-1275; (j) Michalska, M.; Kaplinska, K.; Mirowski, M.; Bodek, A.; Bodek, K. H., Evaluation of the use of fibrin and microcrystalline chitosan membranes as carriers for transforming growth factor beta-1. *J Appl Polym Sci* **2013,** *127* (5), 3506-3513; (k) Ito, R.; Morimoto, N.; Pham, L. H.; Taira, T.; Kawai, K.; Suzuki, S., Efficacy of the Controlled Release of Concentrated Platelet Lysate from a Collagen/Gelatin Scaffold for Dermis-Like Tissue Regeneration. *Tissue Eng Pt A* **2013,** *19* (11-12), 1398-1405; (l) Gelain, F.; Bottai, D.; Vescovi, A.; Zhang, S. G., Designer Self-Assembling Peptide Nanofiber Scaffolds for Adult Mouse Neural Stem Cell 3-Dimensional Cultures. *Plos One* **2006,** *1* (2); (m) Akiyama, N.; Yamamoto-Fukuda, T.; Takahashi, H.; Koji, T., In situ tissue engineering with synthetic self-assembling peptide nanofiber scaffolds, PuraMatrix, for mucosal regeneration in the rat middle-ear. *Int J Nanomed* **2013,** *8*, 2629-2640.

4. Zhang, S. G.; Holmes, T.; Lockshin, C.; Rich, A., Spontaneous Assembly of a Self-Complementary Oligopeptide to Form a Stable Macroscopic Membrane. *P Natl Acad Sci USA* **1993,** *90* (8), 3334-3338.

5. (a) Zhang, S. G.; Gelain, F.; Zhao, X. J., Designer self-assembling peptide

nanofiber scaffolds for 3D tissue cell cultures. *Semin Cancer Biol* **2005,** *15* (5), 413-420; (b) Zhang, S. G.; Lockshin, C.; Cook, R.; Rich, A., Unusually Stable Beta-Sheet Formation in an Ionic Self-Complementary Oligopeptide. *Biopolymers* **1994,** *34* (5), 663-672.

6. Ramachandran, S.; Tseng, Y.; Yu, Y. B., Repeated rapid shear-responsiveness of peptide hydrogels with tunable shear modulus. *Biomacromolecules* **2005,** *6* (3), 1316-1321.

7. Nagai, Y.; Unsworth, L. D.; Koutsopoulos, S.; Zhang, S. G., Slow release of molecules in self-assembling peptide nanofiber scaffold. *J Control Release* **2006,** *115* (1), 18-25.

8. Koutsopoulos, S.; Unsworth, L. D.; Nagai, Y.; Zhang, S. G., Controlled release of functional proteins through designer self-assembling peptide nanofiber hydrogel scaffold. *P Natl Acad Sci USA* **2009,** *106* (12), 4623-4628.

9. Horii, A.; Wang, X. M.; Gelain, F.; Zhang, S. G., Biological Designer Self-Assembling Peptide Nanofiber Scaffolds Significantly Enhance Osteoblast Proliferation, Differentiation and 3-D Migration. *Plos One* **2007,** *2* (2).

10. (a) Gelain, F.; Unsworth, L. D.; Zhang, S. G., Slow and sustained release of active cytokines from self-assembling peptide scaffolds. *J Control Release* **2010,** *145* (3), 231-239; (b) Galler, K. M.; Aulisa, L.; Regan, K. R.; D'Souza, R. N.; Hartgerink, J. D., Self-Assembling Multidomain Peptide Hydrogels: Designed Susceptibility to Enzymatic Cleavage Allows Enhanced Cell Migration and Spreading. *J Am Chem Soc* **2010,** *132* (9), 3217-3223.

11. Ding, X. C.; Janjanam, J.; Tiwari, A.; Thompson, M.; Heiden, P. A., Peptide-

Directed Self-Assembly of Functionalized Polymeric Nanoparticles Part I: Design and Self-Assembly of Peptide-Copolymer Conjugates into Nanoparticle Fibers and 3D Scaffolds. *Macromol Biosci* **2014,** *14* (6), 853-871.

12. Nagy, J.; Folhoffer, A.; Horvath, A.; Csak, T.; Taba, G.; Szentmihalyi, K.; Szalay, F.; Zelko, R., Kinetic study of zinc sulphate release from lipophilic matrices prepared for the therapy of Wilson's disease. *Pharmazie* **2005,** *60* (7), 524-526.

## Chapter 6 references

1. (a) Liu, Y. Y.; Choi, C. H., Condensation-induced wetting state and contact angle hysteresis on superhydrophobic lotus leaves. *Colloid Polym Sci* **2013,** *291* (2), 437-445; (b) Wood, J., Superhydrophobic polymers cast from lotus leaves FABRICATION & PROCESSING. *Mater Today* **2005,** *8* (10), 15-15.

2. (a) Munch, E.; Launey, M. E.; Alsem, D. H.; Saiz, E.; Tomsia, A. P.; Ritchie, R. O., Tough, Bio-Inspired Hybrid Materials. *Science* **2008,** *322* (5907), 1516-1520; (b) Launey, M. E.; Munch, E.; Alsem, D. H.; Barth, H. B.; Saiz, E.; Tomsia, A. P.; Ritchie, R. O., Designing highly toughened hybrid composites through nature-inspired hierarchical complexity. *Acta Mater* **2009,** *57* (10), 2919-2932.

3. Yang, W.; Sherman, V. R.; Gludovatz, B.; Mackey, M.; Zimmermann, E. A.; Chang, E. H.; Schaible, E.; Qin, Z.; Buehler, M. J.; Ritchie, R. O.; Meyers, M. A., Protective role of Arapaima gigas fish scales: Structure and mechanical behavior. *Acta Biomater* **2014,** *10* (8), 3599-3614.

4. Yang, W.; Gludovatz, B.; Zimmermann, E. A.; Bale, H. A.; Ritchie, R. O.; Meyers, M. A., Structure and fracture resistance of alligator gar (Atractosteus spatula) armored fish scales. *Acta Biomater* **2013,** *9* (4), 5876-5889.

5. Yang, W.; Chen, I. H.; Mckittrick, J.; Meyers, M. A., Flexible Dermal Armor in Nature. *Jom-Us* **2012,** *64* (4), 475-485.

6. (a) Allison, P. G.; Chandler, M. Q.; Rodriguez, R. I.; Williams, B. A.; Moser, R. D.; Weiss, C. A.; Poda, A. R.; Lafferty, B. J.; Kennedy, A. J.; Seiter, J. M.; Hodo, W. D.; Cook, R. F., Mechanical properties and structure of the biological multilayered material system, Atractosteus spatula scales. *Acta Biomater* **2013,** *9* (2), 5289-5296; (b) Sun, C. Y.;

Chen, P. Y., Structural design and mechanical behavior of alligator (Alligator mississippiensis) osteoderms. *Acta Biomater* **2013,** *9* (11), 9049-9064; (c) Chakraborty, R.; Bepari, S.; Banerjee, A., Application of calcined waste fish (Labeo rohita) scale as low-cost heterogeneous catalyst for biodiesel synthesis. *Bioresource Technol* **2011,** *102* (3), 3610-3618.

7. (a) Liu, H. J.; Cao, Y. L.; Wang, F.; Huang, Y. Q., Nitrogen-Doped Hierarchical Lamellar Porous Carbon Synthesized from the Fish Scale As Support Material for Platinum Nanoparticle Electrocatalyst toward the Oxygen Reduction Reaction. *Acs Appl Mater Inter* **2014,** *6* (2), 819-825; (b) Waghmare, P. R.; Gunda, N. S. K.; Mitra, S. K., Under-water superoleophobicity of fish scales. *Sci Rep-Uk* **2014,** *4*.

8. (a) Ikoma, T.; Kobayashi, H.; Tanaka, J.; Walsh, D.; Mann, S., Microstructure, mechanical, and biomimetic properties of fish scales from Pagrus major. *J Struct Biol* **2003,** *142* (3), 327-333; (b) Zhu, D. J.; Ortega, C. F.; Motamedi, R.; Szewciw, L.; Vernerey, F.; Barthelat, F., Structure and Mechanical Performance of a "Modern" Fish Scale. *Adv Eng Mater* **2012,** *14* (4), B185-B194.

9. Vernerey, F. J.; Barthelat, F., On the mechanics of fishscale structures. *Int J Solids Struct* **2010,** *47* (17), 2268-2275.

10. Tuan, W. H.; Yu, Y. J.; Chin, Y. L., From Biomimetic Concept to Engineering Reality - A Case Study on the Design of Ceramic Reinforcement. *Adv Eng Mater* **2011,** *13* (4), 351-355.

11. Meyers, M. A.; Lin, Y. S.; Olevsky, E. A.; Chen, P. Y., Battle in the Amazon: Arapaima versus Piranha. *Adv Eng Mater* **2012,** *14* (5), B279-B288.

12. Pati, F.; Adhikari, B.; Dhara, S., Isolation and characterization of fish scale

collagen of higher thermal stability. *Bioresource Technol* **2010,** *101* (10), 3737-3742.

13. (a) Liu, W. T.; Zhang, Y.; Li, G. Y.; Miao, Y. Q.; Wu, X. H., Structure and composition of teleost scales from snakehead Channa argus (Cantor) (Perciformes : Channidae). *J Fish Biol* **2008,** *72* (4), 1055-1067; (b) Kongsri, S.; Janpradit, K.; Buapa, K.; Techawongstien, S.; Chanthai, S., Nanocrystalline hydroxyapatite from fish scale waste: Preparation, characterization and application for selenium adsorption in aqueous solution. *Chem Eng J* **2013,** *215*, 522-532; (c) Burg, K. J. L.; Porter, S.; Kellam, J. F., Biomaterial developments for bone tissue engineering. *Biomaterials* **2000,** *21* (23), 2347-2359; (d) Chen, S.; Hirota, N.; Okuda, M.; Takeguchi, M.; Kobayashi, H.; Hanagata, N.; Ikoma, T., Microstructures and rheological properties of tilapia fish-scale collagen hydrogels with aligned fibrils fabricated under magnetic fields. *Acta Biomater* **2011,** *7* (2), 644-652.

14. (a) Agbor, V. B.; Cicek, N.; Sparling, R.; Berlin, A.; Levin, D. B., Biomass pretreatment: Fundamentals toward application. *Biotechnol Adv* **2011,** *29* (6), 675-685; (b) Luo, L.; van der Voet, E.; Huppes, G., Biorefining of lignocellulosic feedstock - Technical, economic and environmental considerations. *Bioresource Technol* **2010,** *101* (13), 5023-5032; (c) Palumbo, A. J.; Daughney, C. J.; Slade, A. H.; Glover, C. N., Influence of pH and natural organic matter on zinc biosorption in a model lignocellulosic biofuel biorefinery effluent. *Bioresource Technol* **2013,** *146*, 169-175.

15. (a) Baltazar-Y-Jimenez, A.; Bismarck, A., Surface modification of lignocellulosic fibres in atmospheric air pressure plasma. *Green Chem* **2007,** *9* (10), 1057-1066; (b) Gadhe, J. B.; Gupta, R. B.; Elder, T., Surface modification of lignocellulosic fibers using high-frequency ultrasound. *Cellulose* **2006,** *13* (1), 9-22.

16. (a) Duran, N.; Lemes, A. P.; Duran, M.; Freer, J.; Baeza, J., A Minireview of Cellulose Nanocrystals and Its Potential Integration as Co-Product in Bioethanol Production. *J Chil Chem Soc* **2011,** *56* (2), 672-677; (b) Sacui, I. A.; Nieuwendaal, R. C.; Burnett, D. J.; Stranick, S. J.; Jorfi, M.; Weder, C.; Foster, E. J.; Olsson, R. T.; Gilman, J. W., Comparison of the Properties of Cellulose Nanocrystals and Cellulose Nanofibrils Isolated from Bacteria, Tunicate, and Wood Processed Using Acid, Enzymatic, Mechanical, and Oxidative Methods. *Acs Appl Mater Inter* **2014,** *6* (9), 6127-6138.

17. (a) Kaushik, A.; Singh, M., Isolation and characterization of cellulose nanofibrils from wheat straw using steam explosion coupled with high shear homogenization. *Carbohyd Res* **2011,** *346* (1), 76-85; (b) Qing, Y.; Sabo, R.; Zhu, J. Y.; Agarwal, U.; Cai, Z. Y.; Wu, Y. Q., A comparative study of cellulose nanofibrils disintegrated via multiple processing approaches. *Carbohyd Polym* **2013,** *97* (1), 226-234.

18. Youn, H. S.; Shin, T. J., Supramolecular assembly of collagen fibrils into collagen fiber in fish scales of red seabream, Pagrus major. *J Struct Biol* **2009,** *168* (2), 332-336.

19. Ho, L. N.; Ong, S. A.; Osman, H.; Chong, F. M., Enhanced photocatalytic activity of fish scale loaded TiO2 composites under solar light irradiation. *J Environ Sci-China* **2012,** *24* (6), 1142-1148.

20. Atefi, R.; Razmavar, A.; Teimoori, F.; Teimoori, F., Mechanical Characterization, Fabrication and FTIR Spectroscopic Analysis of Fish Scale Reinforced Epoxy Composites. *Life Sci J* **2012,** *9* (2), 1080-1082.

21. Shokuhfar, T.; Gao, Q.; Ashtana, A.; Walzack, K.; Heiden, P.; Friedrich, C., Structural instabilities in TiO2 nanotubes. *J Appl Phys* **2010,** *108* (10).

22. Sader, J. E.; Sanelli, J. A.; Adamson, B. D.; Monty, J. P.; Wei, X. Z.; Crawford, S.

A.; Friend, J. R.; Marusic, I.; Mulvaney, P.; Bieske, E. J., Spring constant calibration of atomic force microscope cantilevers of arbitrary shape. *Rev Sci Instrum* **2012,** *83* (10).

23. Yang, W.; Chen, I. H.; Gludovatz, B.; Zimmermann, E. A.; Ritchie, R. O.; Meyers, M. A., Natural Flexible Dermal Armor. *Adv Mater* **2013,** *25* (1), 31-48.

24. Varsamos, S.; Nebel, C.; Charmantier, G., Ontogeny of osmoregulation in postembryonic fish: A review. *Comp Biochem Phys A* **2005,** *141* (4), 401-429.

25. Morsi, S. M.; Pakzad, A.; Amin, A.; Yassar, R. S.; Heiden, P. A., Chemical and nanomechanical analysis of rice husk modified by ATRP-grafted oligomer. *J Colloid Interf Sci* **2011,** *360* (2), 377-385.

# Appendix A: Supporting information for Chapter 3

**The NMR data:**

We synthesized three chain transfer agents (CTA): TC1, TC2 and TDT using methods reported in the literature. Figure S1 shows the $^{1}$H NMR(a) spectrum and $^{13}$C NMR (b) spectrum for S, S'-bis(α,α′-dimethylacetic acid) trithiocarbonate (BDAT / TC1) synthesized following the procedures of J. T. Lai, D. Filla, R. Shea. *Macromolecules* 2002, 35, 6754-6756). Figure S2 shows the $^{1}$H NMR spectrum for Dibenzyl trithiocarbonate (TC2) synthesized using the procedures of N. Aoyagi, T. Endo. *J Poly Sci Poly Chem* 2009, 47, 3702-3709). Figure S3 shows the $^{1}$H NMR spectrum of 1,3,5-Benzenetricarbodithioic acid (TDT), synthesized following the procedures of A. Dureault, D. Taton, M. Destarac, F. Leising, Y. Gnanou. *Macromolecules* 2004, 37, 5513- 5519.

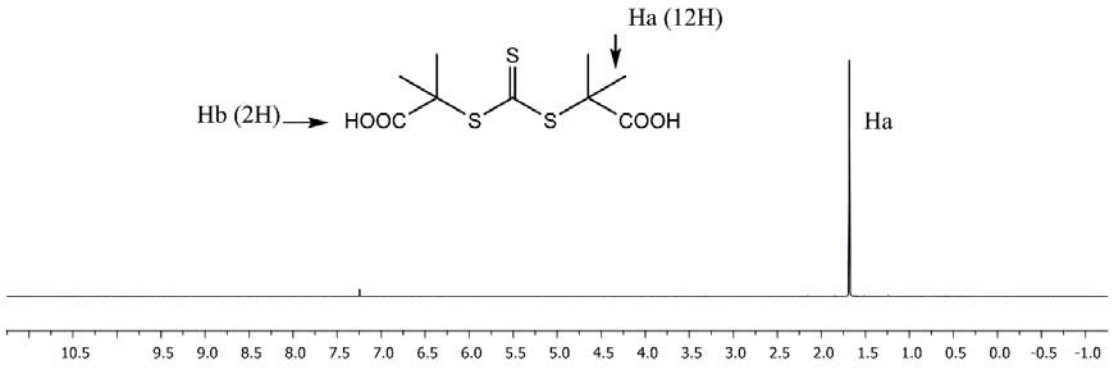


(a) TC1: $^{1}$H NMR: 1.68 (s, -CH3, 12H), the COOH should out of range

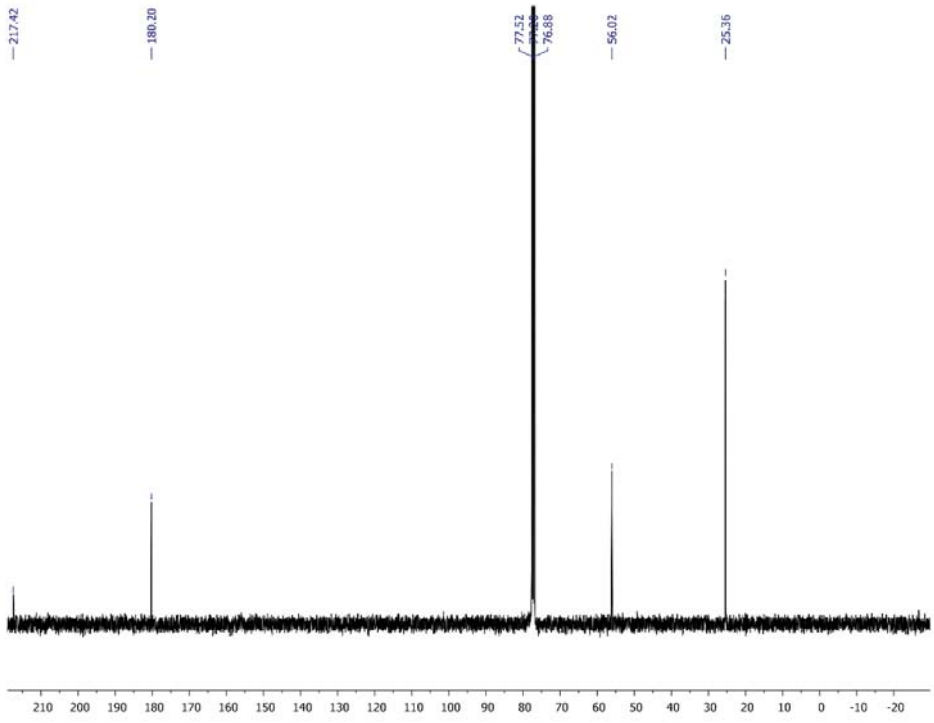


(b) TC1: $^{13}$C NMR, 25.36, 56.02, 180.20, 217.42

Figure A1 TC1 (a) $^{1}$H NMR spectrum and (b) $^{13}$C NMR spectrum

Dibenzyl trithiocarbonate (TC2)

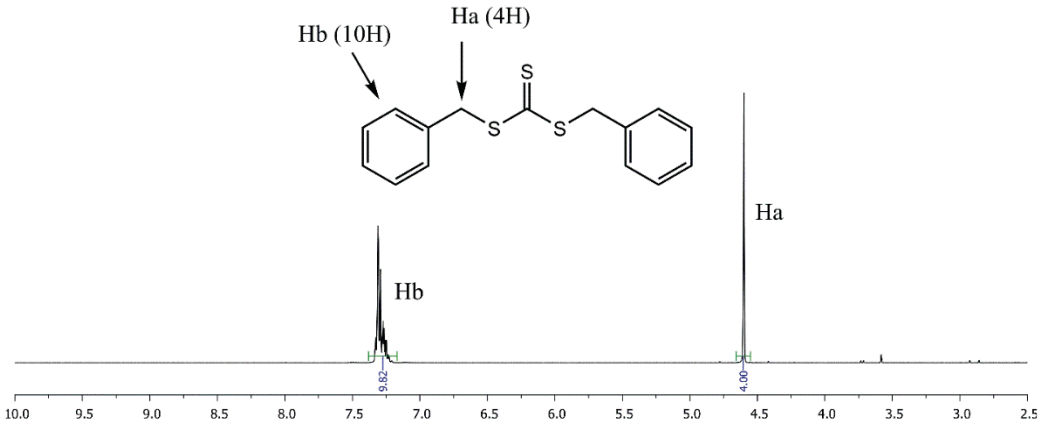


TC2: $^{1}$H NMR 4.60 (s, Ar-CH2- 4H), 7.21-7.35 (m, Ar-H, 10H).

Figure A2 TC2 $^{1}$H NMR spectrum

1,3,5-Benzenetricarbodithioic acid (TDT)

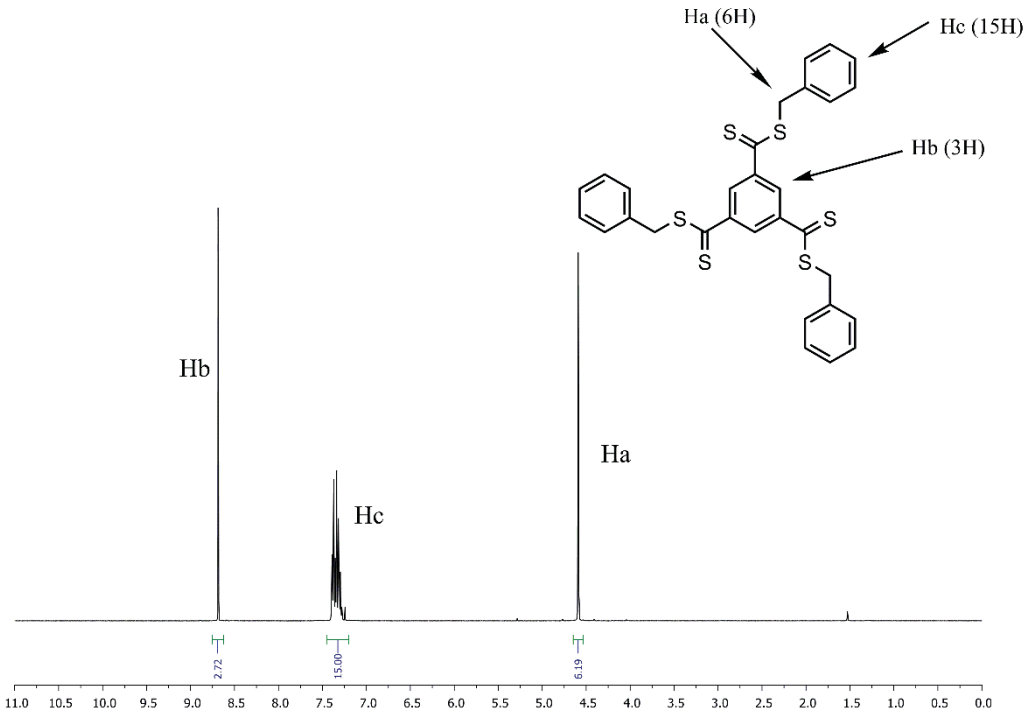


TDT: $^{1}$H NMR 4.58 (s, -S-$CH_2$-, 6H), 7.23-7.58 (m, $CH_2$-ArH, 15H), 8.68 (s, ArH, 3H)

Figure A3 TDT $^{1}$H NMR spectrum

**The Gel Permeation Chromatography (GPC) data**

Table A1 Molecular weights and PDI of PEG standard polymers.

| Standard | Mn, Da | Mw, Da | PDI |
|---|---|---|---|
| 1 | 895 | 1020 | 1.14 |
| 2 | 10600 | 12200 | 1.15 |
| 3 | 22100 | 25800 | 1.17 |
| 4 | 31700 | 41300 | 1.30 |
| 5 | 81900 | 94600 | 1.16 |

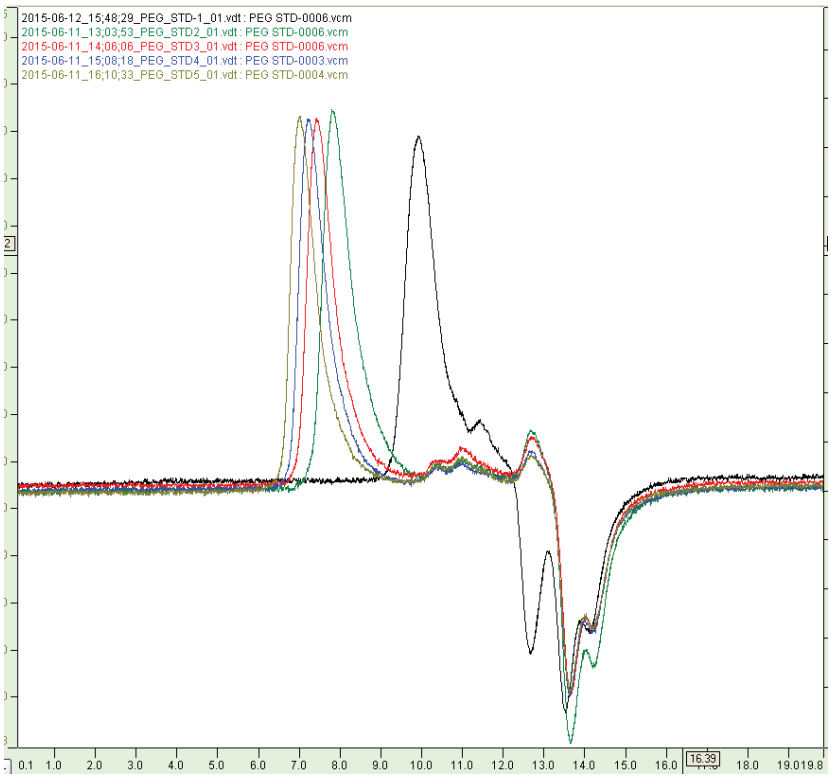


Figure A4 GPC spectra of PEG standard polymers. (RI Intensity vs PEG Retention Time (min).

Table A2 Molecular weight and Polydispersity by GPC

| Specimen | Mw | PDI |
|---|---|---|
| DT1/ S-$D_{50}O_{50}$-C1 | 44000 | 3.49 |
| DT1/ S-$O_{50}D_{50}$-C1 | 27900 | 2.46 |
| DT2/S-$D_{50}O_{50}$-C2 | 38800 | 3.08 |
| DT2/ S-$O_{50}D_{50}$-C2 | 29200 | 2.56 |
| DT3/S-$D_{50}O_{50}$-C3 | 30900 | 4.71 |
| DT3/ S-$O_{50}D_{50}$-C3 | 21300 | 2.47 |

| | | |
|---|---|---|
| TC1/ C-$O_{25}D_{50}O_{25}$-C | 37800 | 4.42 |
| TC1/ C-$D_{25}O_{50}D_{25}$-C | 22700 | 2.67 |
| TC2/ Ph-$O_{25}D_{50}O_{25}$-Ph | 30800 | 3.42 |
| TC2/ Ph-$D_{25}O_{50}D_{25}$-Ph | 33800 | 3.72 |
| TDT/ S-$(D_{50}O_{50})_3$-C6 | 77100 | 5.69 |
| TDT/ S-$(O_{50}D_{50})_3$-C6 | 81400 | 5.86 |

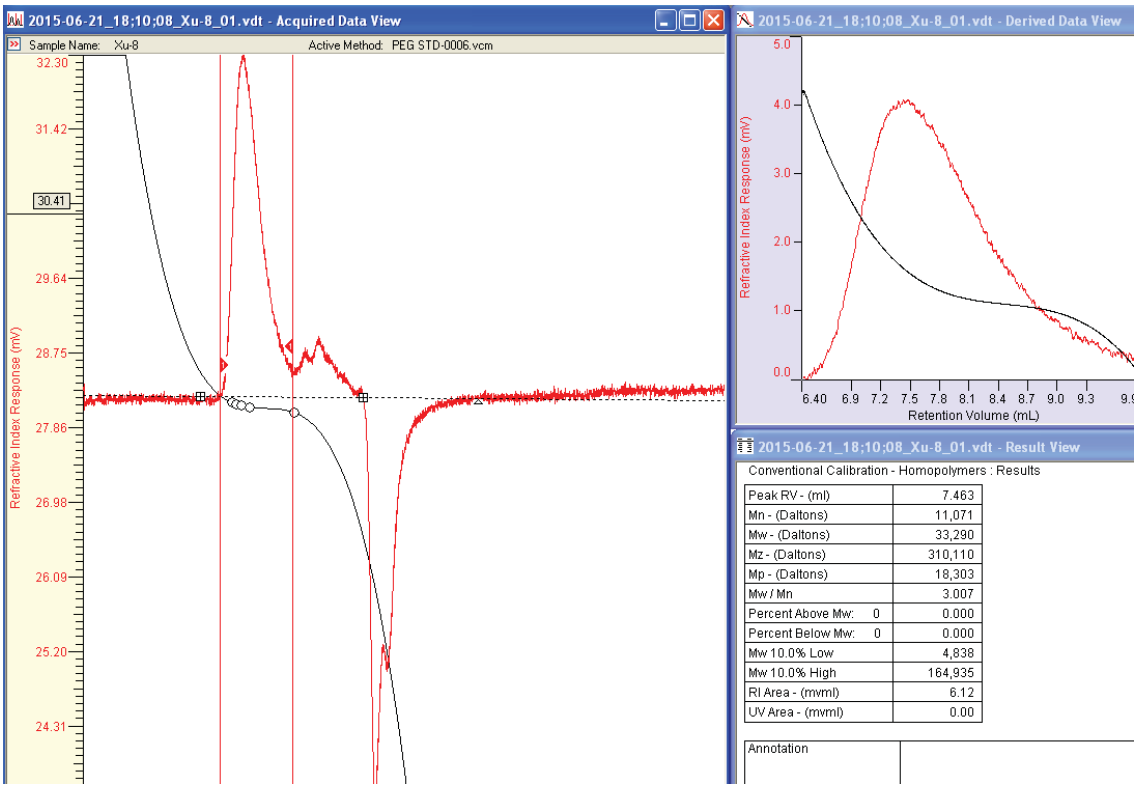


Figure A5 GPC of Specimen TC1/C-$D_{25}O_{50}D_{25}$-C

# Appendix B: Derjaguin-Muller-Toropov (DMT) modulus background (Chapter 6)

The Derjaguin-Muller-Toporov (DMT) model of modulus is based on Hertzian model. It is suitable for describing stiff contacts with low adhesion forces and small tip radii,[1] therefore it is widely used in AFM nanomechanical measurements to calculate the modulus of the sample. To understand the DMT model, we must consider the Hertzian model first.

The Hertzian model[2] begins with the following assumptions:

1) The strains are small and within the elastic limit
2) The surfaces are continuous and non-conforming (implying that the area of contact is much smaller than the characteristic dimensions of the contacting bodies).
3) Each body can be considered an elastic half-space.
4) The surface is frictionless.

Based on these assumptions, the DMT model[1, 3] then takes into consideration the attractive interactions outside the area of contact (adhesion).

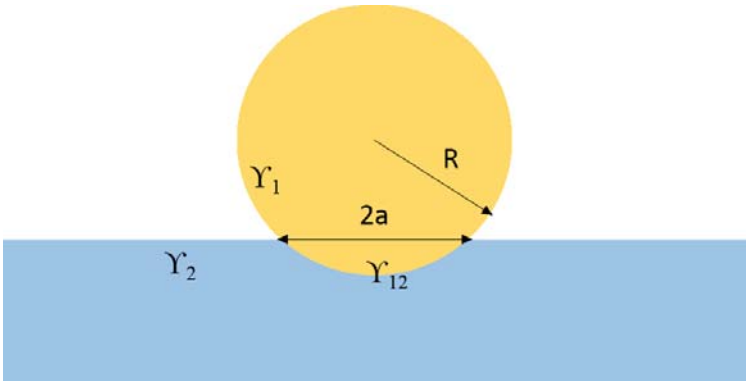


Figure B1 The basic DMT model

Figure B1 illustrates how a probe tip would contact and indent a surface (relative areas not to scale). $\Upsilon_1$ and $\Upsilon_2$ are the surface energy of each of those surfaces that will be in contact but before they actually do contact, while $\Upsilon_{12}$ is the surface energy of the contact area after contacting. *R* is the radius of the sphere and *a* is the radius of contract area. When an AFM probe tip contacts a surface it applies a force, *F*, which is the force (positive in compression). A specific probe tip will have known quantities, including a given spring constant, so that the work needed to indent a polymer surface can be calculated as long as the probe tip is first calibrated to that surface, which allows determining $\Upsilon_2$ and $\Upsilon_{12}$. Therefore, when the tip is withdrawn from the surface a $\Delta\Upsilon$ is measured, which is defined the work of adhesion: $\Delta\Upsilon = \Upsilon_1 + \Upsilon_2 - \Upsilon_{12}$. This value is extracted from Equation B1 and can also be seen in Figure B2 as the difference in energy needed to withdraw the probe from its deepest point of indentation back to the surface of the material being indented. Furthermore, because the tip is calibrated the stiffness, or modulus of a material being indented, *E* can also be extracted from Equation B1, and is taken as the slope of the linear part of the curve from when the probe tip moves forward to indent the surface of the material being tested.

$$a^3 = \frac{3R}{4E}(F + 2\Delta\gamma\pi R) \quad \rightarrow \quad E = \frac{3R}{a^3}(F + 2\Delta\gamma\pi R) \quad \text{Equation B1}$$

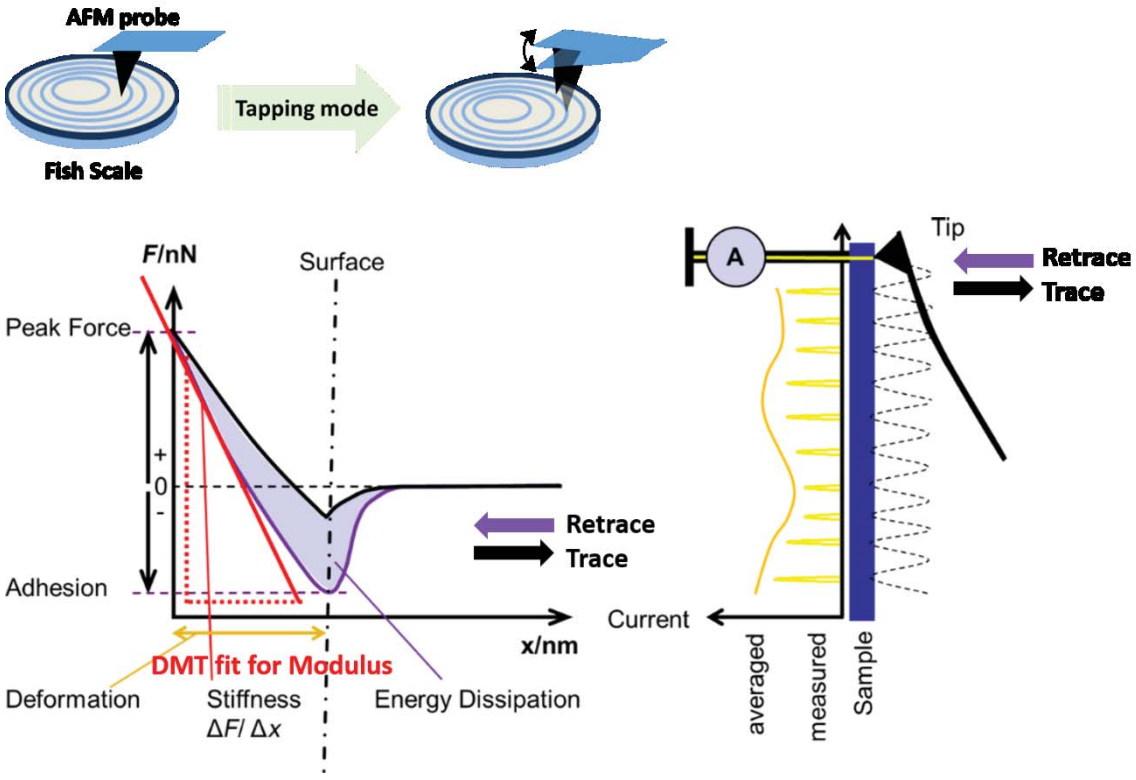


Figure B2 DMT modulus of fish scale tested by AFM (Adapted from *Beilstein J. Nanotechnol.* 2013, 4, 611–624.)

In this work, the DMT modulus of fish scale was test by AFM using a peak force tapping mode. The calibrated probe (10~15 nm) and instrument software (Nanoscope Analysis v1.4) generate nanomechnical maps of sample surfaces by generating a small indentation on the sample surface and collecting a force-separation curve[4] as illustrated in Figure B2. Using this force separation curve the adhesion and DMT modulus are calculated by fitting to the DMT model[5] and using Equation B2:

$$F = \frac{4}{3}E^*\sqrt{Rd^3} + F_{adh} \qquad \text{Equation B2}$$

Where $F$ is the force, $R$ is the tip radius, $d$ is the separation, $F_{adh}$ is the adhesion force, and $E^*$ is the reduced elastic modulus. The elastic modulus of the probe ($E_{tip}$) is much greater than sample modulus $E_s$ and the Poisson's ratio of the sample is known as $v_s$, so the young's modulus for the sample ($E_s$) can be calculated[5] (Equation B3):

$$E^* = \left(\frac{1-v_s^2}{E_s} + \frac{1-v_{tip}^2}{E_{tip}}\right)^{-1} \rightarrow \frac{1}{E^*} = \frac{1-v_t^2}{E_t} + \frac{1-v_s^2}{E_s} \approx \frac{1-v_s^2}{E_s} \qquad \text{Equation B3}$$

The deflection sensitivity of the cantilever spring constant was measured by indenting a known material: a hard sapphire surface (56.67 nm/V). Then the cantilever spring constant adjust by using thermal tuning method (K = 38.9 N/m). The quantitative nanomechanical maps were generated by force-separation curves. All the modulus data of fish scale samples were the average data from an area (~2 μm × 2 μm) in nanomechanical maps.

Reference:


1. Derjaguin, B. V.; Muller, V. M.; Toporov, Y. P., Effect of Contact Deformations on the Adhesion of Particles. *Prog Surf Sci* **1994,** *45* (1-4), 131-143.

2. Lachaise, J.; Clausse, M., Application of Model of Double Spherical Dispersion to Study with Hertzian Spectroscopy on Process of Change of State of Substance Dispersed in Emulsion - Freezing of Water. *Cr Acad Sci B Phys* **1973,** *276* (8), 287-290.

3. Muller, V. M.; Derjaguin, B. V.; Toporov, Y. P., On 2 Methods of Calculation of the Force of Sticking of an Elastic Sphere to a Rigid Plane. *Colloid Surface* **1983,** *7* (3), 251-259.

4. Hiesgen, R.; Sogel, S.; Costa, R.; Carle, L.; Galm, I.; Canas, N.; Pascucci, B.; Friedrich, K. A., AFM as an analysis tool for high-capacity sulfur cathodes for Li-S batteries. *Beilstein J Nanotech* **2013,** *4*.

5. Morsi, S. M.; Pakzad, A.; Amin, A.; Yassar, R. S.; Heiden, P. A., Chemical and nanomechanical analysis of rice husk modified by ATRP-grafted oligomer. *J Colloid Interf Sci* **2011,** *360* (2), 377-385.

# Appendix C: Permission License Number for Chapter 5

This Agreement between Xu Xiang ("You") and John Wiley and Sons ("John Wiley and Sons") consists of your license details and the terms and conditions provided by John Wiley and Sons and Copyright Clearance Center.

| | |
|---|---|
| License Number | 3657841272273 |
| License date | Jun 28, 2015 |
| Licensed Content Publisher | John Wiley and Sons |
| Licensed Content Publication | Macromolecular Bioscience |
| Licensed Content Title | Peptide-Directed Self-Assembly of Functionalized Polymeric Nanoparticles. Part II: Effects of Nanoparticle Composition on Assembly Behavior and Multiple Drug Loading Ability |
| Licensed Content Author | Xu Xiang,Xiaochu Ding,Trevor Moser,Qi Gao,Tolou Shokuhfar,Patricia A. Heiden |
| Licensed Content Date | Dec 4, 2014 |
| Pages | 15 |
| Type of use | Dissertation/Thesis |
| Requestor type | Author of this Wiley article |
| Format | Print and electronic |
| Portion | Full article |
| Will you be translating? | No |
| Title of your thesis / dissertation | Biological Materials: Part A. Temperature-responsive Polymers and Drug Delivery and Part B. Polymer Modification of Fish Scale and their Nano-mechanical Properties |
| Expected completion date | Jul 2015 |
| Expected size (number of pages) | 175 |
| Requestor Location | Xu Xiang<br>1801B<br>Woodmar Dr.<br><br>HOUGHTON, MI 49931<br>United States<br>Attn: Xu Xiang |
| Billing Type | Invoice |
| Billing Address | Xu Xiang<br>1801B<br>Woodmar Dr.<br><br>HOUGHTON, MI 49931<br>United States<br>Attn: Xu Xiang |
| Total | 0.00 USD |

# Appendix D: Permission License Number for Figures in Chapter 2

## Permission License Number for Figure 2.8

**JOHN WILEY AND SONS LICENSE TERMS AND CONDITIONS**

Jul 03, 2015

This Agreement between Xu Xiang ("You") and John Wiley and Sons ("John Wiley and Sons") consists of your license details and the terms and conditions provided by John Wiley and Sons and Copyright Clearance Center.

| | |
|---|---|
| License Number | 3661500430222 |
| License date | Jul 03, 2015 |
| Licensed Content Publisher | John Wiley and Sons |
| Licensed Content Publication | Angewandte Chemie International Edition |
| Licensed Content Title | Reaction of Cyclic Tetrathiophosphates with Carboxylic Acids as a Means to Generate Dithioesters and Control Radical Polymerization By RAFT |
| Licensed Content Author | Alex Duréault,Yves Gnanou,Daniel Taton,Mathias Destarac,Frédéric Leising |
| Licensed Content Date | Jun 24, 2003 |
| Pages | 4 |
| Type of use | Dissertation/Thesis |
| Requestor type | University/Academic |
| Format | Print and electronic |
| Portion | Figure/table |
| Number of figures/tables | 2 |
| Original Wiley figure/table number(s) | Scheme 2 |
| Will you be translating? | No |
| Title of your thesis / dissertation | Biological Materials: Part A. Temperature-responsive Polymers and Drug Delivery and Part B. Polymer Modification of Fish Scale and their Nano-mechanical Properties |
| Expected completion date | Jul 2015 |
| Expected size (number of pages) | 175 |
| Requestor Location | Xu Xiang<br>1801B<br>Woodmar Dr.<br><br>HOUGHTON, MI 49931<br>United States<br>Attn: Xu Xiang |
| Billing Type | Invoice |
| Billing Address | Xu Xiang<br>1801B<br>Woodmar Dr.<br><br>HOUGHTON, MI 49931<br>United States<br>Attn: Xu Xiang |
| Total | 0.00 USD |

# Permission License Number for Figure 2.21

**Title:** Hepta(3,3,3-trifluoropropyl) Polyhedral Oligomeric Silsesquioxane-capped Poly(N-isopropylacrylamide) Telechelics: Synthesis and Behavior of Physical Hydrogels

Logged in as:
Xu Xiang
Account #:
3000931188

LOGOUT

**Author:** Lei Wang, Ke Zeng, Sixun Zheng
**Publication:** Applied Materials
**Publisher:** American Chemical Society
**Date:** Mar 1, 2011



**PERMISSION/LICENSE IS GRANTED FOR YOUR ORDER AT NO CHARGE**

This type of permission/license, instead of the standard Terms & Conditions, is sent to you because no fee is being charged for your order. Please note the following:

- Permission is granted for your request in both print and electronic formats, and translations.
- If figures and/or tables were requested, they may be adapted or used in part.
- Please print this page for your records and send a copy of it to your publisher/graduate school.
- Appropriate credit for the requested material should be given as follows: "Reprinted (adapted) with permission from (COMPLETE REFERENCE CITATION). Copyright (YEAR) American Chemical Society." Insert appropriate information in place of the capitalized words.
- One-time permission is granted only for the use specified in your request. No additional uses are granted (such as derivative works or other editions). For any other uses, please submit a new request.

# Permission License Number for Figure 2.23

**ROYAL SOCIETY OF CHEMISTRY LICENSE TERMS AND CONDITIONS**

Jul 03, 2015

This is a License Agreement between Xu Xiang ("You") and Royal Society of Chemistry ("Royal Society of Chemistry") provided by Copyright Clearance Center ("CCC"). The license consists of your order details, the terms and conditions provided by Royal Society of Chemistry, and the payment terms and conditions.

**All payments must be made in full to CCC. For payment instructions, please see information listed at the bottom of this form.**

| | |
|---|---|
| License Number | 3661510093398 |
| License date | Jul 03, 2015 |
| Licensed content publisher | Royal Society of Chemistry |
| Licensed content publication | Polymer Chemistry |
| Licensed content title | End group removal and modification of RAFT polymers |
| Licensed content author | Helen Willcock,Rachel K. O'Reilly |
| Licensed content date | Dec 23, 2009 |
| Volume number | 1 |
| Issue number | 2 |
| Type of Use | Thesis/Dissertation |
| Requestor type | non-commercial (non-profit) |
| Portion | figures/tables/images |
| Number of figures/tables/images | 1 |
| Format | print and electronic |
| Distribution quantity | 20 |
| Will you be translating? | no |
| Order reference number | None |
| Title of the thesis/dissertation | Biological Materials: Part A. Temperature-responsive Polymers and Drug Delivery and Part B. Polymer Modification of Fish Scale and their Nano-mechanical Properties |
| Expected completion date | Jul 2015 |
| Estimated size | 175 |
| Total | 0.00 USD |

# Permission License Number for Figure 2.24 and Figure 2.26

**ROYAL SOCIETY OF CHEMISTRY LICENSE TERMS AND CONDITIONS**

Jul 03, 2015

This is a License Agreement between Xu Xiang ("You") and Royal Society of Chemistry ("Royal Society of Chemistry") provided by Copyright Clearance Center ("CCC"). The license consists of your order details, the terms and conditions provided by Royal Society of Chemistry, and the payment terms and conditions.

**All payments must be made in full to CCC. For payment instructions, please see information listed at the bottom of this form.**

| | |
|---|---|
| License Number | 3661510258866 |
| License date | Jul 03, 2015 |
| Licensed content publisher | Royal Society of Chemistry |
| Licensed content publication | Polymer Chemistry |
| Licensed content title | End group removal and modification of RAFT polymers |
| Licensed content author | Helen Willcock,Rachel K. O'Reilly |
| Licensed content date | Dec 23, 2009 |
| Volume number | 1 |
| Issue number | 2 |
| Type of Use | Thesis/Dissertation |
| Requestor type | non-commercial (non-profit) |
| Portion | figures/tables/images |
| Number of figures/tables/images | 2 |
| Format | print and electronic |
| Distribution quantity | 20 |
| Will you be translating? | no |
| Order reference number | None |
| Title of the thesis/dissertation | Biological Materials: Part A. Temperature-responsive Polymers and Drug Delivery and Part B. Polymer Modification of Fish Scale and their Nano-mechanical Properties |
| Expected completion date | Jul 2015 |
| Estimated size | 175 |
| Total | 0.00 USD |
| Terms and Conditions | |

# Permission License Number for Figure 2.27

**ELSEVIER LICENSE**
**TERMS AND CONDITIONS**

Jul 03, 2015

This is a License Agreement between Xu Xiang ("You") and Elsevier ("Elsevier") provided by Copyright Clearance Center ("CCC"). The license consists of your order details, the terms and conditions provided by Elsevier, and the payment terms and conditions.

**All payments must be made in full to CCC. For payment instructions, please see information listed at the bottom of this form.**

| | |
|---|---|
| Supplier | Elsevier Limited<br>The Boulevard,Langford Lane<br>Kidlington,Oxford,OX5 1GB,UK |
| Registered Company Number | 1982084 |
| Customer name | Xu Xiang |
| Customer address | 1801B<br>HOUGHTON, MI 49931 |
| License number | 3661511403957 |
| License date | Jul 03, 2015 |
| Licensed content publisher | Elsevier |
| Licensed content publication | Advances in Colloid and Interface Science |
| Licensed content title | Smart core/shell nanocomposites: Intelligent polymers modified gold nanoparticles |
| Licensed content author | Dongxiang Li,Qiang He,Junbai Li |
| Licensed content date | 30 July 2009 |
| Licensed content volume number | 149 |
| Licensed content issue number | 1-2 |
| Number of pages | 11 |
| Start Page | 28 |
| End Page | 38 |
| Type of Use | reuse in a thesis/dissertation |
| Intended publisher of new work | other |
| Portion | figures/tables/illustrations |
| Number of figures/tables/illustrations | 1 |
| Format | both print and electronic |
| Are you the author of this Elsevier article? | No |
| Will you be translating? | No |
| Original figure numbers | Figure 2 |
| Title of your thesis/dissertation | Biological Materials: Part A. Temperature-responsive Polymers and Drug Delivery and Part B. Polymer Modification of Fish Scale and their Nano-mechanical Properties |
| Expected completion date | Jul 2015 |
| Estimated size (number of pages) | 175 |
| Elsevier VAT number | GB 494 6272 12 |
| Permissions price | 0.00 USD |
| VAT/Local Sales Tax | 0.00 USD / 0.00 GBP |
| Total | 0.00 USD |